UNIVERSITAT POLITÈCNICA DE CATALUNYA BARCELONATECH

Geologically constrained joint inversion of hydraulic, tracer and ERT data for process visualization

Andrea Viviana Palacios Pierluissi

UNIVERSITAT POLITÈCNICA DE CATALUNYA

Department of Civil and Environmental Engineering

Geologically constrained joint inversion of hydraulic, tracer and ERT data for process visualization

Thesis presented by

Andrea Viviana Palacios Pierluissi

To obtain the degree of Doctor in Civil Engineering

Work conducted at the Institute of Environmental Assessment and Water Research (IDAEA-CSIC) under the supervision of

Director
Dr. Jesús Carrera
IDAEA-CSIC

Codirector
Dr. Juan José Ledo
Universitat de Barcelona

Tutor
Dr. Xavier Sánchez-Vila
UPC

Barcelona, July 2021

This project was funded by the European Union's Horizon 2020 research and innovation programme under the Marie Sklodowska-Curie Grant Agreement No 722028 and by the projects CGL2016-77122-C2-1-R/2-R of the Spanish Government.

To Emilien, Paulina and Baby 2

Acknowledgements

Now that I'm days away from submitting my thesis project to the Doctoral school, I would like to thank all those that took part in these almost 4 years of work.

Thank you Prof. Jesús Carrera, my thesis director at IDAEA-CSIC, for seeing an exploitable potential in me and giving me the opportunity to participate in the European Commission ENIGMA Innovative Training Network as your student. Thank you for the interesting lessons in hydrogeology and in programming, for sharing your vision and thoughts with me during long debates about the state-of-the-art and your opinion on what is done and what should be done. Conversations with you very often finished with my brain enlightened (and spinning) with so much information and ideas. Thank you for taking me serious and for listening to and respecting my points of view, for treating me like a colleague and helping me in giving closure to this project, especially these last months.

Thank you Prof. Juanjo Ledo, from the University of Barcelona, for presenting me and trusting me with the beautiful geophysical dataset that gave so much life to my thesis. Being the only geophysicist in the research group at IDAEA-CSIC, you represented a great support during these years. Thank you for your efficiency, for your presence when needed and for your good advices. I hope you are satisfied with what I could make out of those CHERT panels.

Thank you Dr. Niklas Linde, from the University of Lausanne, for always being there when most needed. Without your support, brightness, time and patience, I wouldn't be about to submit this thesis. Thank you for having me in your group for a few months. Every visit to Lausanne was a breath of fresh air, and it refilled me with good energy and positivism about what I was doing. I am very glad we met in the ENIGMA ITN, and that you agreed to be part of my project.

Thank you Dr. Juan Hidalgo and Dr. Daniel García, from IDAEA-CSIC, for taking many hours to sit and talk with me. You two helped me in covering some of my weaknesses in the IT tools I needed to actually do what I had in mind. I will be forever grateful with you for helping me moving forward when I thought I was most stuck.

Thank you soon-to-be Dr. Tybaud Goyetche, for being my colleague and friend in this unique thesis experience since day 1. Thank you for teaching me so much at the field, for always answering the simplest hydrogeology and hydrogeochemistry questions with patience, and for the numerous conversations we had to help keep each other sane and strong throughout the years. It was a pleasure working by your side.

Thank you to the whole ENIGMA ITN, professors and PhD students, for the good work environment that was created among us. I truly enjoyed every workshop and field training, as well as the dinners and hangouts during the conferences and the meetings. I am very proud of being a part of this ITN. A special thank you to Dr. Peter Engesgaard, Dr. Majken Looms, and Dr. Joel Tirado, for welcoming me in Copenhagen during my secondments and for showing me such a nice way of working and living.

Thank you to the MEDISTRAES project members, for sharing the Argentona site with me, for celebrating my first publication with me, and for making me part of the seawater intrusion community. There is so much to be done, and I hope the work I made was helpful for everyone involved. I look forward to hearing about all the progresses made in the project.

To all those who shared the hall of the 4th floor, the coffee machine tiny room, the long tables in the yard while having lunch, and who celebrated with me the arrival of my first child: thank you for being there, for relaxing stressful days, for the company and empathy, for talking about anything non-thesis related when needed, and for also being there when thesis-related talks were necessary.

Thank you to all my friends, not only for the all the good moments that make us be friends, but for trying to understand and follow my work, for supporting me and for telling me I could finish this successfully.

Thank you to my parents and siblings, for forging my personality and making me the person and the professional I am today. Thank you for believing in my potential and for nurturing the confidence I have in me. Thank you also to my extended family for your unconditional support and for your presence although far away.

Thank you a million times to my husband, Emilien, my daughter Paulina, and baby girl number 2 in my womb. Emilien, thank you for living an adventurous life with me, for seeing opportunities and exciting things where others may see too much trouble, for accepting to move our family to Barcelona so that I can live this experience. Thank you for your support and your patience, for understanding how challenging and exhausting this experience was for me, and at the same time for understanding and supporting my will of doing things right and my motivation to keep on going. Thank you for wanting me to shine always brighter. Paulina, thank you for keeping my priorities straight, for being such a lovely and fun girl, and for bringing so much joy to my life in times of stress at work. You are the best! Baby number 2, thank you for keeping me company with all your kicks and movements while finishing this project and writing my thesis. You are already such a good girl!

Table of contents

ABSTRACT **1**

RESUMEN **3**

1 INTRODUCTION **5**

2 TIME-LAPSE CROSS-HOLE ELECTRICAL RESISTIVITY TOMOGRAPHY (CHERT) FOR MONITORING SEAWATER INTRUSION DYNAMICS IN A MEDITERRANEAN AQUIFER. **8**

2.1 Introduction **8**

2.2 The Argentona site **9**

2.3 CHERT experimental setup **11**

2.4 Processing and inversion methods **12**

2.5 Results **14**
2.5.1 Reference Model 14
2.5.2 Time-lapse results 16

2.6 Discussion **22**
2.6.1 Surface ERT vs. CHERT 22
2.6.2 Reference model: link between bulk EC and geological conceptual model 23
2.6.3 Time-lapse study: long-term effects 24
2.6.4 Time-lapse study: short-term effects 25
2.6.5 Model validation 26
2.6.6 The CHERT experiment 26

2.7 Conclusions **27**

3 HYDROGEOPHYSICAL INVERSION OF HEADS, SOLUTE TRACER AND GEOELECTRICAL DATA FOR SEAWATER INTRUSION CHARACTERIZATION: THE ARGENTONA CASE. **28**

3.1 Introduction **28**

3.2 Experimental site **30**

3.3 Methodology **31**
3.3.1 Conceptual Model 31

3.3.2 Density-dependent flow and transport Model 32
3.3.3 Petrophysics and Geoelectrical modelling 33
3.3.4 Handling head and concentration data 36
3.3.5 Hydrogeophysical Objective Function 37

3.4 Results 38
3.4.1 Testing the conceptual models: one aquitard or three aquitards. 38
3.4.2 Hydrological and hydrogeophysical inverse problems. 41

3.5 Discussion 45
3.5.1 The role of thin aquitard layers in the hydraulic behavior. 45
3.5.2 Data quality in coastal aquifers. 46
3.5.3 Combining datasets: worse fit but better prediction 47
3.5.4 Time-lapse monitoring simulation. 47
3.5.5 Numerical dispersion: will we ever simulate correctly the fully fresh or fully salty water? 48

3.6 Conclusions 48

4 CALIBRATION OF DENSITY-DEPENDENT FLOW MODELS USING GEOELECTRICAL DATA: DEALING WITH NUMERICAL DISPERSION 50

4.1 Introduction 50

4.2 Methodology 51
4.2.1 What we propose 51
4.2.2 Why using the cumulative distribution function (CDF)? 52
4.2.3 Modification of the HHCCR inverse problem. 53

4.3 Results 54

4.4 Discussion 59
4.4.1 The optimized CDF-type conversion and the width of the transition zone. 59
4.4.2 The change in the estimated parameters post numerical dispersion correction. 60
4.4.3 The best model: worst calibration fit but best prediction capabilities. 61
4.4.4 The Argentona site conceptual model improvements: the before and after calibration 61

4.5 Conclusions 62

5 GENERAL CONCLUSIONS 63

6 BIBLIOGRAPHY 65

7 ANNEX 71

List of figures

Figure 2.1 (a) Location map of the Argentona site, some 30 km northeast of Barcelona, Spain. (b) Field spread of the Argentona site, installed piezometers (black dots), piezometers equipped with electrodes (yellow dots), surface ERT and CHERT transects. (c) Vertical cross-section showing piezometers with screened depth, location of the 36 electrodes in each well and stratigraphic correlation (modified from Martínez-Pérez et al. (2019). Two sandy aquifers are loosely separated by a silt layer at 12 m depth. The semi-confined aquifer is underlaid by weathered granite. 10

Figure 2.2 (a) Stainless-steel meshes (electrodes) permanently fastened around PVC piezometers for time-lapse CHERT experiment during piezometer installation. (b) Electrode configurations used in the survey. A total of 5843 measurements are recorded per CHERT in less than 30 minutes. Data is acquired sequentially by considering one pair of neighbouring boreholes at the time. 4 CHERT are needed to build a complete CHERT, the whole 2D transect from boreholes N225 to PP20. 12

Figure 2.3 Bulk electrical conductivity models obtained by the inversion of the CHERT and surface-based ERT data (a), the result when only considering the complete CHERT (b) and only the surface ERT (c) with the corresponding calculated coverages for each model (d-f). The complete CHERT model shows conductive anomalies (in red), which are not shown by the surface ERT model. The inversion of both datasets combines the coverages and yields an image with higher resolution near the surface and in depth (d). 15

Figure 2.4 Result from the inversion of surface and cross-hole ERT (dataset from September 8th, 2015). Stratigraphic columns are shown to relate stratigraphic units with bulk conductivities. Grey dots represent the electrodes around the boreholes and on surface. Grey dashed line indicates the approximate groundwater table. Black dashed line indicates the silt layer. This cross-section is used as reference model in the time-lapse inversion. 16

Figure 2.5 Percentage of accepted data points in each CHERT, after quality control during data pre-processing. Note the decrease in the amount of accepted data with time, most likely due to corrosion of the electrodes, particularly in the PP20-PP15 panel, which is located the closest to the sea. 16

Figure 2.6 Results from the time-lapse inversion of 16 complete CHERT acquired during 2 years (July 2015 through September 2017). Images display the ratio of bulk electrical conductivity with respect to September 2015 (a brownish area implies higher EC and, therefore, salinity than in September, 2015). The silt layer is indicated with a dashed line. Note the increase in bulk EC in the upper-right side (<80 m of distance to the sea), and along a line just below the silt layer, indicating a rise in the saltwater interface. 18

Figure 2.7 Average conductivities extracted from the inverted models, at -8 m a.s.l (blue), -12.5 m a.s.l (green) and -16 m a.s.l (red). Precipitation (PPT) data from Cabrils station and simulated significant wave height time-series are displayed. The points indicate times of CHERT campaigns. Note that acquisitions were made before and after the 220 mm precipitation event of October 12, 2016. Significant seasonal fluctuations and an overall increase of EC can be seen in the upper part of the semiconfined aquifer (elevation of -12 m a.s.l), but are negligible in the lower portion of both the shallow unconfined aquifer (-8 m a.s.l) and the semi-confined aquifer (-16 m a.s.l). 19

Figure 2.8 (a) Ratio between the bulk electrical conductivity model of September 30 and October 21, 2016. The heavy rain occurred on October 12, 2016. The image shows a decrease in conductivity in the unconfined and semi-confined aquifer and a conductivity increase in the unsaturated zone on both sides of nest N1. The decrease in conductivity observed along borehole PP15 is attributed to freshwater

infiltration due to borehole construction. (b) Time-series of groundwater level in boreholes N115, average significant wave height (grey bars) and precipitation (black bars). Highlighted is the heavy rain event of 220mm that occurred on October 12, 2016. The event was accompanied with an increase in groundwater level and in significant wave height. 19

Figure 2.9 (a) Ratio of October 2016 to February 2017 CHERT ECs. (b) Extraction of CHERT bulk EC profiles along PP20. The winter period with higher significant wave heights is marked by a twofold increase in bulk electrical conductivity values from the coastline until 90 m from the coastline. The extractions in (b) show the bulk EC in the upper layers during winter (200 mS/m), and the recovery 6 months after winter (100 mS/m). The extractions also evidence the increase in conductivity in the lower aquifer. 20

Figure 2.10 Water electrical conductivity measurements taken on water samples from piezometers in nests N1, N2, N3, and N4. The piezometers are grouped according to the elevation of the screened intervals: “upper” (blue, -7 to -10 m a.s.l), “transition” (green, -11.5 to -13.5 m a.s.l) and “lower” (red, -15.5 to -18.5 m a.s.l), where EC is that of seawater. 21

Figure 2.11 Annual precipitation since 2000 from Cabrils weather station, 7 kilometers northeast from the site. Average precipitation is 584,1 mm (dashed line). Note that the monitoring period is below the average. The black bar in 2016 represents the 220 mm rain event of October 12, which probably produced relatively less recharge than typical rainfalls.....22

Figure 2.12 Comparison of bulk electrical conductivity models obtained from induction logs and CHERT along piezometers in nests N2 (a), N4 (b), N3 (c) and N1 (d). The CHERT logs were extracted from the CHERT bulk EC models along the boreholes.....22

Figure 3.1. a) Localization of the Argentona site, 40 km northeast of Barcelona, in Spain, and map view of the Argentona site with the monitoring line perpendicular to the coast (in yellow). c) The stratigraphic correlation shows the lithology identified in the piezometers, based on geophysical boreholes and core descriptions. The aquifers are composed of alluvial sediments, and the base of the aquifers is composed of weathered granite. Thin clay and silt layers separate the subsurface in three sequences. Along the monitoring line there are three nests (N2, N3 and N1) with three piezometers each, with screens at 15, 20 and 25 m depth, and three individual piezometers (PP15, PP18 and PP20). PP15 and PP20 are fully screened. The piezometers are equipped with annular electrodes. 31

Figure 3.2. Temporal and spatial discretization of the Argentona site hydrological model. The timeline shows 4 periods: first, a 200-years pseudo steady-state; then, a 4 and ½ warm-up period during which varying boundary conditions with time-series start; finally, the actual experiment is simulated at the site during two years with a daily time-step. The first year of the monitoring is used for model calibration, and the second year is used for model validation. The mesh covers a total of 600 m, with 200 m at the seaside, and 45 m in depth. The site topography reaches a maximum of 7.3 m on the left side. The cells of the mesh vary from 2x1 m to 1x1 m (from bottom to top). Boundary conditions for flow and solute transport are represented in the figure with colored lines. 32

Figure 3.3. Boundary conditions applied to the boundaries of the hydrological model. a) Precipitation in the study area during the monitoring period (black). Top freshwater (FW) recharge, as computed by the soil water balance (red). A few precipitation episodes represent the effective FW recharge. b) Lateral inflow from the inland boundary is the result of the simulation using the box model and the head variations measured in a borehole 400 m uphill. The red dashed line illustrates that the inflow of FW diminishes during the monitoring period, from 2015 until 2017. c) Sea level variations, as registered in the Barcelona port. d) Wave-height simulated data from SIMMAR. The red line indicates the threshold of >2 m chosen for the application of the storm surge boundary condition. 34

Figure 3.4. Model 1A (top) represents what was initially believed for the Argentona site layering: one continuous silt layer separates the aquifer into two. The dots represent the observation points for the readings of the simulated data during the calibration process. Model 3A (bottom) is the update of the conceptual model after the results from the CHERT experiment were interpreted along with other experimental data. Two very thin aquitard layers at -5 m a.s.l and -17 m a.s.l were found to be important for the hydraulic behavior of the aquifer and the water salinity distribution. The dots represent the observation points for the readings of the simulated data during the calibration process. 35

Figure 3.5. Scheme of the coupled hydrogeophysical modelling and inversion tools. The link between hydrological and geophysical simulators was done using a Python interface, which calls the density-dependent flow and transport simulator (SEAWAT) through Flopy and the cross-hole electrical resistivity tomography simulator (CHERT) through PyGIMLi. The conversions necessary to convert salinities to bulk electrical resistivity are done inside the Python interface, as well as the data conversion (from h to hh, and from c to cc). The inverse problem is solved using PEST, which collects the simulated and the observed data through its specific input files. 39

Figure 3.6. Result of the calibration of the heads observation group using the **HC** inverse problem on the one aquitard (1A) and the three aquitard (3A) models. The grey area denotes the data points that were calibrated and the white area shows the non-calibrated data points belonging to the validation period. The three columns group the piezometers in the freshwater zone, the transition zone and the seawater zone, following the classification made in Chapter 2. The two models reach a reasonable fit in the three areas, however, the 3A model is superior in the validation test for the freshwater zone piezometers. 40

Figure 3.7. Result of the calibration of the apparent bulk electrical resistivity (rho) observation group using the **HC** inverse problem on the one aquitard (1A) and the three aquitard (3A) models. Above, the first CHERT dataset from July 2015, belonging to the calibration period; below, the last CHERT dataset from September 2017, belonging to the validation period. Both models display a similar fit during the calibration phase, but the 3A model yields better results in the validation tests. 40

Figure 3.8. Result of the calibration of the heads observation group using the **HC, HHCC** and **HHCCR** inverse problems on the three aquitard (3A) model. The grey area denotes the data points that were calibrated and the white area shows the non-calibrated data points belonging to the validation period. Inverse problems HC and HHCCR show a very similar result in all piezometers. The HHCC problem does not fit the absolute value of the heads, but gives more weight to the variations keeping a homogeneous gap between simulated and observed time series. 43

Figure 3.9. Result of the calibration of the concentrations observation group using the **HC, HHCC** and **HHCCR** inverse problems on the three aquitard (3A) model. The grey area denotes the data points that were calibrated and the white area shows the non-calibrated data points belonging to the validation period. The HC and HHCCR inverse problems preserve the freshwater area, although the HHCCR should be fresher than 5 g/L; they are able to reproduce the salinization in the piezometers of the transition zone and to position salt water in the piezometers in the saltwater zone. The HHCC inverse problem yields a model with a very high water salinity, even in the freshwater zone. 44

Figure 3.10. Result of the calibration of the apparent bulk electrical resistivity (rho) using the **HC, HHCC** and **HHCCR** inverse problems on the three aquitard (3A) model. The HHCC inverse problem failed to calibrate and predict the rho time series. The HC and HHCCR problems yield a better result during the calibration phase (a), and the HHCCR makes in general a better prediction, mainly by achieving higher resistivities. In October 2016, a heavy rain event that took place a few days before the CHERT (b) caused higher resisitivity readings. This one-day phenomenon is not properly reproduced by our model, due to its time discretization, and also to the missing third dimension, important for the fresh surface and groundwater flow from the Argentona stream towards the aquifers. 44

Figure 3.11. Time-lapse view of the simulated spatial distribution of salinity computed with the HHCCR calibrated model. Black lines show the position of the silt layers at -5, -9 and -17 m a.s.l, known to limit the SWI. We can highlight that the model reproduces the entrance of the SWI into the lower aquifer, from 60 m to 120 m from the coast in the two years of monitoring; the vertical movement of the transition zone, and the storm surge effect on the beach area in January and February 2017. The weathered granite layer is simulated with a salinity lower than seawater salinity, from the site until more than a hundred meter after the coastline.....45

Figure 4.1. Link between hydrological and geoelectrical simulator (left panel). Water salinities from the hydrological model are first converted to water electrical conductivities (ECw) and then to bulk electrical conductivities (ECb) through a petrophysical law. The conversion law between water salinity and water EC are commonly linear, but we propose a cumulative distribution function (CDF) type conversion in order to correct the numerical dispersion of the hydrological simulator. The CDF-type conversion law would lower ECw in low salinity areas and increase it in high salinity areas.....52

Figure 4.2. Illustration of the procedure to fit a salinity curve to another salinity curve with a given dispersion value. Three snapshots of the analytical solution of the advection-dispersion equation at 10, 20 and 40 days are displayed for three models ran with dispersion values: D = 1.0E-3 (black), 4E-3 (green) and 1.6E-2 (red). By optimizing the parameters of the CDF, each concentration curve can be changed from a modelled output to another output under different dispersion conditions (green and red dots). The table shows the optimal parameters and it can be observed that they change for each dispersion value and vary with time. 53

Figure 4.3. Conversion curves used to relate water salinities and water electrical conductivities. The linear conversion is the one originally used in the HHCCR inverse problem presented in Chapter 3. In the first modification of the inverse problem (CDF), we use the CDF-type conversion curve with fixed parameters: μ = 19 g/L, σ = 10 g/L, and a=5.8 S/m. In the second modification of the inverse problem (CDF-STD), we use the CDF-type conversion and include the CDF standard deviation in the parametrization. Green arrows illustrate the impacts of changing the standard deviation of the a priori CDF.....54

Figure 4.4. A priori (black), CDF (red) and CDF-STD (green) estimated values for the lateral inflow boundary conditions of the hydrogeophysical model. The CDF problem finds that the highest fresh groundwater flow passes through aquifer 3, while CDF-STD problem estimates that the highest lateral inflow goes through aquifers 1 and 2.....57

Figure 4.5. A priori (red) and estimated (green) salinity vs. ECw relations. Inverse problem CDF-STD found a value of 16 for the CDF standard deviation, creating a smoother conversion line and, consequently, wider transition zone. According to the estimated curve, pure freshwater would have a minimum water EC of 0.24 S/m, and seawater with 38 g/L of salt would have a ECw of 5.5 S/m. Both extreme values are consistent with Argentona site data. 57

Figure 4.6. Result of the calibration of the apparent bulk electrical resistivity (rho) using the Linear, CDF and CDF-STD inverse problems. CHERT panels PP20-PP15 and PP15-N125 are on the beach area and are the most affected by the storm surges that occurred early 2017. The CDF inverse problem yields too low resistivities in both panels from February 2017 and September 2017, suggesting an overestimation of the saltwater infiltration. With the CDF-STD the simulated bulk apparent resistivities in the prediction period respect the change from more conductive to more resistive in each panel, although it still doesn't reproduce the dispersive behavior of the points in panels PP20-PP15 and PP15-N125 after the heavy rain episode in October 2016. 58

Figure 4.7. Result of the simulated salt concentrations using the Linear, CDF and CDF-STD inverse problems. The grey area denotes the data points that were calibrated and the white area shows the non-calibrated data points belonging to the validation period. The estimated salinity in the freshwater

zone lowers with both CDF and CDF-STD estimations. In the transition zone, CDF-STD estimation follows the salinization trend, better than the CDF estimation. In the saltwater zone, the estimated salinity is lower than with the Linear problem, and the decreasing trend in N325 is not reproduced. Overall, the estimated absolute values are not far from field measurements, except in the PP20a borehole, where the predictions for model CDF are too high. 58

Figure 4.8. Result of the calibration of the heads observation group using the Linear, CDF and CDF-STD inverse problems on the three aquitard (3A) model. The grey area denotes the data points that were calibrated and the white area shows the non-calibrated data points belonging to the validation period. The calibrated head values of models CDF and CDF-STD are better for all piezometers. In the validation period, however, the CDF model overestimated the head increase during the days of storm surge..... 59

Figure 4.9. Time-lapse view of the simulated spatial distribution of salinity computed with the Linear and the CDF-STD models. Black lines show the position of the silt layers at -5, -9 and -17 m a.s.l, known to limit the SWI. The main difference between both models is the salinity of the freshwater zone of the model. The salinity distribution is less dispersive in the upper part of the model, above the silt layers at -5 and -9 m a.s.l. In the beach area, the effect of storm surges completely disappeared in June 2016, and the washout is more visible in September 2017, for the CTD-STD model..... 60

List of tables

Table 3.1. Names and composition of the three inverse problems that were solved to calibrate the Argentona site hydrogeophysical model. HC: inverse problem using heads and salt concentration data with equal weight inside the objective function. HHCC: inverse problem using heads, salt concentrations, salt concentration differences and head differences with ranked weights according to the interpreter's confidence in the datasets. HHCCR: inverse problem using heads, salt concentrations, salt concentration differences, head differences and apparent bulk electrical resistivity datasets. Apparent bulk electrical resistivities correspond to the CHERT experiment and a high confidence was put on this dataset given its quality. 38

Table 3.2. Summary of the results of the inverse problems HC, HHCC and HHCCR, along with the a priori values of the calibrated parameters and the absolute values of the total and partial objective functions. The hydraulic conductivities found by the inverse problems HC and HHCCR are similar in magnitude, while HHCC found lower hydraulic conductivities in the aquifer layers. The HHCCR supports the idea of a large freshwater flow through the aquifer layers, especially through the weathered granite. A value of 15 was found for the formation factor of the alluvial sediments, much higher than expected. For the comparison of the objective functions, all data points were given the same weight of 1.0. It can be observed that including more datasets worsens the fit of the observation groups (e.g. H, HH and CC), except in the case of the salt concentrations where the HHCCR problem reaches a better fit for group C. The misfits in the validation period (prediction) indicate that the HHCCR inverse problem is the one that yields the best results. 42

Table 4.1. Summary of the results of the inverse problems CDF and CDF-STD. The results from the HC and the Linear problems solved in Chapter 2 and the a priori values of the calibrated parameters are shown for comparison. The hydraulic conductivities found by the inverse problems CDF and CDF-STD problems are similar to the HC and the Linear problem results in the aquifer layers, but one order of magnitude lower in aquitard 3 and the weathered granite. The arrangement of the fresh groundwater flow from the CDF and the CDF-STD problems changes drastically from the a priori values and previous results, putting most of the flow through the alluvial aquifer layers and not the weathered granite. Problem CDF found a higher value for the storm surge multipliers. The estimated values for the formation factor of the alluvial layers were also reduced to 5 and 11.83, in comparison with the 15.34 found in the Linear inverse problem. These values are closer to the expected value. The CDF standard deviation changed from 10 to 16 during the calibration process. For the comparison of the objective functions, all data points were given the same weight of 1.0. It can be observed that neither the CDF nor the CDF-STD problems reduced the misfits in the calibration period, but problem CDF-STD has the lowest misfits in the validation period. 56

Abstract

Seawater intrusion (SWI) consists in the movement of seawater (SW) into freshwater (FW) aquifers, contaminating drinking water resources. SWI, along with the parallel reduction of Submarine Groundwater Discharge may lead to ecological impacts beyond the reduction of FW resources. Water salinity is the critical physical property to identify SWI. The salinity contrast between FW ($\sim 1 g/L$) and SW (35g/L) is high enough for salinity and, therefore, water electrical conductivity (ECw), to be indirectly measured using geophysical techniques such as geophysical logs (e.g. induction) or electrical and electromagnetic methods (e.g. electrical resistivity tomography, ERT). Although the context of SWI sounds ideal for the use of geophysics, ERT displays poor resolution in depth.

We propose using cross-hole ERT (CHERT) to enhance resolution, placing the electrodes in depth along the boreholes. We tested it for the first time in a SWI context, at the Argentona experimental site, some 40 km NE of Barcelona. Results of the 2-years time-lapse CHERT monitoring showed that the use of CHERT and surface ERT increased the model resolution, and the bulk EC (ECb) values from CHERT were validated with induction logs from the site. We were able to image the seasonal fluctuations of groundwater flux that cause the SW-FW interface to move seawards during periods of high flux or landwards during periods of low flux; as well as the salinization of the aquifer due to an intense drought in the study area during the monitoring period. Two short-term events were also imaged: a decrease in ECb related to a heavy rain event, and an increase in ECb in the beach area related to storm surges.

We built a hydrogeophysical model to characterize the Argentona site using all available data types. The model couples a density-dependent flow and transport simulator with a geoelectrical solver through a petrophysical relation. This model was calibrated by minimizing the misfit between observed and simulated hydraulic heads, salt concentrations and apparent ECb. The calibration was done on four time stages: a pseudo steady-state period, a model warm-up period for the introduction of time-varying boundary conditions, a calibration period covering the first year of the Argentona site monitoring, and a validation period covering the second year. The latter was used to assess the prediction capability of the models. The procedure allowed us to update the original conceptual model and demonstrate the importance of even the finest silt-rich layers. Then, three inverse problems were performed on the updated conceptual model: a) using the traditional point measurements of heads and salinity; b) adding the time variations of heads and the spatial differences of salinity to address common issues of using heads and salinity measurements taken from boreholes in coastal aquifers; and c) adding the apparent ECb from the time-lapse CHERT. We discuss the value of using time variations of heads, instead of only head absolute values; as well as on the use of spatial differences of salt concentrations. The model calibrated using all types of data (heads, salinity and ECb) had the best prediction capability and the model was able to reproduce the main events observed during the two years of monitoring of the Argentona site.

Numerical dispersion prevents the model from simulating FW (0-1 g/L), which affects calibration. To tackle this issue, we propose to use an alternative conversion from water salinity to ECw that corrects for numerical dispersion when computing ECb. The methodology consists in applying and calibrating the error function to reduce salinity in the FW zone, and increase it in the SW zone. The

error function calibration can also change the width of the FW-SW interface. This conversion improved the model prediction capability and led to a set of parameters less affected by numerical dispersion (e.g. estimated petrophysical parameters are within the expected range).

Resumen

La intrusión salina (SW) es el flujo de agua de mar (SW) hacia acuíferos de agua dulce (FW), contaminando las reservas de agua potable. La SWI, más la disminución de la Descarga de Agua Submarina, tiene impactos ecológicos más allá de la reducción del agua potable. La salinidad del agua es clave para identificar la SWI. El contraste entre el FW ($\sim 1 g/L$) y el SW (35g/L) es tan alto que la salinidad, y la conductividad eléctrica del agua (ECw), puede ser medida usando técnicas geofísicas como los sondeos (e.g. inducción) o los métodos eléctricos y electromagnéticos (e.g. tomografía de resistividad eléctrica, ERT). Aunque el contexto de la SWI suene ideal para el uso de la geofísica, la ERT tiene baja resolución en profundidad.

Proponemos el uso de ERT entre pozos (CHERT) para mejorar la resolución, con los electrodos a lo largo de los piezómetros. Se ha testeado el CHERT por primera vez para la SWI en el sitio experimental de Argentona, a 40 km al noreste de Barcelona. Los resultados de los dos años de monitoreo muestran que el uso del CHERT y del ERT mejora la resolución del modelo, y los valores de la EC del medio (ECb) se validaron con los sondeos de inducción. Se logró visualizar las fluctuaciones temporales de los flujos de agua subterránea que causan que la interfaz FW-SW se mueva hacia el mar en periodos de alto flujo, o hacia el interior en periodos de bajo flujo; al igual que la salinización del acuífero debido a una sequía intensa en el área durante el periodo de monitoreo. Dos eventos de corta duración también se detectaron: una disminución en la ECb por un evento de lluvia intensa, y un aumento de la ECb en el área de la playa por las mareas de tormenta.

Se construyó un modelo hidrogeofísico para caracterizar el sitio de Argentona usando todos los datos disponibles. El modelo acopla dos simuladores a través de una relación petrofísica: el de flujo y transporte con densidad variable y el de geoeléctrica. El modelo se calibró minimizando la distancia entre las medidas y las simulaciones de los niveles, las salinidades y las ECb aparentes. La calibración se hizo en cuatro periodos: uno pseudo-estacionario, uno de calentamiento que introduce las series temporales, uno de calibración que cubre el primer año de monitoreo, y uno de validación que cubre el segundo año. Este último fue usado para evaluar la capacidad de predicción de los modelos. El procedimiento nos permitió actualizar el modelo conceptual y demostrar la importancia de las capas de limo más finas. Luego, se resolvieron tres problemas inversos usando el modelo conceptual actualizado: a) usando las medidas tradicionales de niveles y de salinidad; b) añadiendo las variaciones temporales de nivel y la variación espacial de salinidad para hacer frente a la dificultad de usar los datos de nivel y salinidad tomados de pozos en acuíferos costeros; y c) añadiendo la ECb aparente del CHERT. Discutimos sobre el valor añadido de usar las variaciones temporales de nivel, en vez de únicamente los valores absolutos; así como sobre el uso de las diferencias espaciales de salinidad. El modelo calibrado usando todos los datos (niveles, salinidad y ECb) tuvo la mejor capacidad de predicción y es capaz de reproducir los principales eventos observados durante los dos años de monitoreo en el sitio de Argentona.

La dispersión numérica evita que el modelo simule la zona de FW (0-1 g/L), afectando la calibración. Para esto, proponemos una conversión alternativa entre la salinidad y la ECw que corrige la dispersión

numérica al calcular la ECb. El método consiste en aplicar y calibrar la función de error para reducir la salinidad del agua en la zona de FW, e incrementarla en la zona de SW. Esta calibración también puede cambiar el ancho de la interface FW-SW. La conversión mejoró la capacidad de predicción del modelo y llevó a obtener un conjunto de parámetros menos afectado por la dispersión numérica (e.g. parámetros petrofísicos estimados dentro del rango de valores esperados).

1 Introduction

Coastal aquifers are an important source of freshwater for agriculture, urbanization and industrial activities for the population living in proximity to the seas and oceans (Cañedo-Argüelles et al., 2019; Michael et al., 2017; Post, 2005a; Werner et al., 2013). Aquifers containing freshwater are submitted to increasing stresses due to human daily activities because of the need of pumping freshwater from the ground. The contact between fresh and saltwater is the origin of a complex physical phenomenon driven by gravitational forces. Saltwater is denser than freshwater, so it flows below freshwater and pushes it upwards. If no other factors affecting the forces of the system were present, a natural equilibrium would be found between both waters and there would be no further movement. Reality is there are several external factors driving the movement of the freshwater-saltwater interface. Sea level rise, for example, increases the weight of the saltwater, pushing it further inland. Pumping freshwater from boreholes decreases the weight of freshwater and lets saltwater in. When saltwater moves inland salinizing the freshwater in the aquifers, we call it seawater intrusion. Understanding how this equilibrium works and ensuring that it is maintained is of great importance for the preservation of freshwater resources. The way to understand it is through the study of the processes that occur in the subsurface and through the characterization of each study area.

Monitoring salinity is critical in seawater intrusion studies, but interpreting and using the typical measurements like hydraulic heads and water salinity from the piezometers is not trivial in coastal aquifers (Carrera et al., 2010; Costall et al., 2020; Post et al., 2007; Shalev et al., 2009). Water salinity profiles made in boreholes are valid only when these are fully open. However, a common technique for isolating a given depth is to make a slotted interval. In screened piezometers, the measurements that are taken are assumed to correspond to the depth of the screen but this is not necessarily the case. Water recirculation inside the borehole accommodates the density dependent flow and, if trapped in deep layers, freshwater can go up through the borehole and mix with saltwater. Plus, if the screen interval is long enough to cover different formations, when we pump water from the borehole we take a water sample which is a mixture of waters from each formation. This is why water salinity profiles rarely measure the maximum seawater salinity. In turn, hydraulic heads are dependent on water salinity. Problems with the salinity inside the borehole compromise hydraulic heads, especially if these must be converted to equivalent freshwater heads previous to being used inside a model. So, there is a need for better techniques to monitor salinity without changing the environment and without affecting the salinity distribution.

Electrical and electromagnetic geophysical methods are widely used for monitoring coastal aquifers thanks to their high sensitivity to the changes in water salinity (Beaujean et al., 2014; Costall et al., 2020; de Franco et al., 2009; Goebel et al., 2017; Huizer et al., 2017; Nguyen et al., 2009; Sutter and Ingham, 2017; Tarallo et al., 2014). They measure water or formation electrical conductivity (EC), which can be used as a proxy for water salinity because of the high linear correlation between both properties. Geophysical techniques have the advantage of being non- or minimally invasive. Surface ERT, for example, consists in positioning electrodes on the surface and measuring the potential that is created after the injection of current. This method has very high sensitivity near the electrodes and

yields 2D or 3D images of the upper layers of the subsurface. In depth, however, the resolution is loss and water EC measurements cannot be translated to the correct salinities. As the sensitivity is near the electrodes, performing the ERT between boreholes is a solution to obtain high resolution in depth. Many field studies have proved that positioning the geophysical tools along the boreholes to perform cross-hole surveys is a good way to monitor tracer tests (Daily et al., 1992; Linde et al., 2006; Looms et al., 2008; Singha and Gorelick, 2005; Slater et al., 2000). The first specific objective of this work is to test the capability of cross-hole ERT to correctly image the seawater intrusion without resolution loss.

The quantitative characterization of the subsurface is usually done through the representation of reality using numerical models. For the creation of these models, the equations describing the physical phenomena are discretized in time and space. To model seawater intrusion, we use the density-dependent flow and transport equation, where hydraulic conductivity is the main parameter controlling the flow of groundwater. High uncertainty in the creation of models is related to knowing the values of the parameters in the study area. An approach to reduce this uncertainty is solving an inverse problem to fit the response of the model to the observed data by fitting the uncertain parameters set. In theory, the more data is given to the inverse problem, the better the result. The typical hydrological inverse problems are based on hydraulic heads and solute tracers' data. In the branch of hydrogeophysics, the aim is to combine hydrological and geophysical datasets to improve the monitoring and characterization of hydrological processes through the use of geophysics (Binley et al., 2015). In the seawater intrusion studies, some have tried to derive salinity from ERT inverted bulk resistivity models (Beaujean et al., 2014; González-Quirós and Comte, 2020; Nguyen et al., 2009). The problem is that these models are the result of an uncertain inverse problem and the errors from these images are propagated to their estimations. In addition to this, as mentioned before, the loss of resolution can cause issues when converting EC to salt mass fraction. The second specific objective of this thesis is to use bulk EC in the inverse problem, along with hydrological data, to calibrate a hydrogeophysical model and test if the inclusion of ERT data improves the results of the model and, more importantly, improves the estimation of water salinity.

Numerical dispersion is a common issue when solving numerically the solute transport equation, related to the time and space discretization. Typically, the modeler must compromise between having the most accurate results thanks to a fine discretization and computing time, so that he is always at least partly confronted to this problem. Numerical dispersion smooths the solute concentration curve preventing us to see the real peaks and lows of concentration (Woods et al., 2003).This means that transport models simulating the seawater intrusion will have problems simulating the maximum and the minimum of water salinity (Werner, 2017). Given that the simulated geophysical data in the hydrogeophysical model depends on the good simulation of water salinities, the error from numerical dispersion is propagated to the geophysical simulator, and thus, affects the calibration of the geophysical datasets. Our third specific objective is to propose and test a methodology to support the use of geoelectrical data when dealing with dispersive hydrological models.

The thesis was developed in the Argentona experimental site, built in the MEDISTRAES project for the study of the seawater intrusion and the submarine groundwater discharge (Folch et al., 2020; Martínez Pérez, 2020). The site is located 40 km northeast of Barcelona, in Spain. In order to fulfill the first objective of the thesis, a 2-years time-lapse CHERT monitoring experiment was carried out at the Argentona site (Palacios et al., 2020), where boreholes on a perpendicular line to the coast were equipped with stainless steel electrodes. For the second and third objective, a hydrogeophysical model was created using SEAWAT (Guo et al., 2008), a density-dependent flow and transport simulator, linked with PyGIMLi (Rücker et al., 2017), the geoelectrical simulator.

In summary, the objective of the thesis is to effectively integrate the geophysical data in the model calibration procedure to try to obtain a model able to simulate, but also predict, the behavior of the system. By doing this, we would propose a novel and efficient methodology for monitoring water

salinity in coastal aquifers and for creating informed numerical models that can help in the groundwater management.

2 Time-lapse cross-hole electrical resistivity tomography (CHERT) for monitoring seawater intrusion dynamics in a Mediterranean aquifer.[1]

2.1 Introduction

Seawater intrusion (SWI) increasingly affects the ever growing populations near coastlines. The inland movement of saline groundwater not only contaminates drinking water resources, but also drives other important changes in ecological and hydrological cycles, thereby creating a hostile environment for plants and animals that are incapable of adapting to salinization (Michael et al., 2017; Post and Werner, 2017). SWI has been studied for many years but, even today, remains an open research topic because of the complex physical, chemical, mechanical, and geological processes involved. The equations that govern interactions between fresh and seawater are well established, and models of simplified generic scenarios are commonly used to predict and assess the risks linked to SWI and to define appropriate management strategies (Abarca et al., 2007; Henry, 1964). However, real field conditions are much more complex and detailed case-studies are less common in the SWI literature.

Salinity is the critical physical property to describe SWI. Water salinity contrasts are so strong that salinity by itself indicates whether water is pure freshwater, pure seawater or a mixture of both (the transition or mixing zone). The electrical conductivity (EC) of water is strongly, positively and linearly correlated with water salinity (Sen and Goode, 1992), so that EC represents an excellent proxy to salinity, to the point that it is often used synonymously with salinity. Electrical and electromagnetic geophysical measurements provide information about the bulk or formation EC, representing the effective conductivity of the mixture of solid rock material and the fluids contained in the pores (Bussian, 1983; Waxman and Smits, 1968). Pore-water electrical conductivity contributes to bulk electrical conductivity, which implies that higher pore water EC results in higher bulk EC. Consequently, bulk EC can be used as an indirect proxy measurement of water EC, and thus, of water salinity (Lesmes and Friedman, 2005; Purvance and Andricevic, 2000). However, bulk EC depends also on factors such as porosity, tortuosity, and constrictivity, which affect electrical current through the liquid, and clay content, which may contribute to bulk EC through mineral surface currents. This implies that detailed site knowledge is needed to quantitatively relate bulk EC to salinity.

Water EC is widely used to visualize SWI (Costall et al., 2018; Falgàs et al., 2009, 2011; Post, 2005b; Zarroca et al., 2011). It is usually measured in piezometers to obtain either point measurements

[1] *This chapter of the thesis is based on the article Palacios et al., 2020. Hydrol. Earth Syst. Sci., 24, 2121–2139.*

(samples) or as water EC profiles in fully screened boreholes. The limited sampling associated with the former makes it inefficient to derive an image of the typically heterogeneous salinity distribution. The latter is not good practice because density-dependent flow inside the borehole makes water EC profiles unrepresentative of the water EC in the surrounding environment (Carrera et al., 2010; Shalev et al., 2009). For this reason, it is tempting to infer water EC from bulk EC using geophysical techniques such as electrical resistivity tomography (ERT).

Since ERT provides more coverage than a few individual point measurements and is noninvasive, it has become a very common approach in SWI studies. In an inversion process, the ERT measurements are transformed into upscaled 2D and 3D images of bulk EC. Many authors have used surface-based ERT in real and synthetic SWI studies (Beaujean et al., 2014; de Franco et al., 2009; Goebel et al., 2017; Huizer et al., 2017; Nguyen et al., 2009; Sutter and Ingham, 2017; Tarallo et al., 2014) with the results being negatively affected by the low resolution of the images at depth. As a manifestation of this problem, Huizer et al. (2017), Beaujean et al. (2014) and Nguyen et al. (2009) showed that using ERT-derived salt-mass fraction for solute transport model calibration lead to important errors due to poor resolution at depth. The computed bulk EC at depth is typically much lower than what we would expect from a seawater wedge with pores completely filled with seawater, which is the generally accepted paradigm of seawater intrusion, a seawater wedge beneath fresh water. Paradoxically, surface ERT results may be consistent with salinity profiles measured in fully screened wells, which often display salinities much lower than that of seawater (Abarca et al., 2007). It is clear that either measurement methods, or the current paradigm, or both, need to be revised.

Costall et al. (2018) review some of the above issues in their comprehensive study about electrical resistivity imaging of the saline water interface in coastal aquifers. Specifically, they mention the scarcity of publications of time-lapse ERT for monitoring SWI dynamics, the low resolution of surface ERT, and imaging limitations related to electrode arrays. They also recommended designing optimized experiments suitable for the monitoring of short and long-term salinity changes in aquifers, and in the swash zone (zone of wave action on the beach), rarely captured by land-based ERT surveys.

We conjecture that cross-hole ERT (CHERT) can enhance the imaging of natural saltwater-freshwater dynamics, given that its superior resolution compared with surface-based deployments have been amply demonstrated in other related application areas (Bellmunt et al., 2016; Bergmann et al., 2012; Kiessling et al., 2010; Leontarakis and Apostolopoulos, 2012; Schmidt-Hattenberger et al., 2013). Although CHERT has drawbacks (high contact resistance in the unsaturated zone, loss of the fully non-invasive nature of surface ERT, and sensitivity being mainly constrained to the region between the boreholes), the benefits of this type of tomography may be larger because the resolution of the inversion images obtained will be high at the depths where changes are expected to occur. Nevertheless, there is yet no field demonstration in the literature to test this conjecture as CHERT has never been used for monitoring SWI, most likely due to cost constraints, the high risk of electrode corrosion in saline environments, and because it typically covers a smaller investigation area than surface ERT or time-domain electromagnetics (the most common geophysical technique in saltwater intrusion studies).

The objective of this work is to overcome the above-mentioned limitations. Specifically, we test CHERT for imaging SWI and its dynamics through time-lapse acquisitions. To do so, a two-year monitoring experiment was conducted at the Argentona site, located in a permeable coastal alluvial aquifer in northeast Spain.

2.2 The Argentona site

The Argentona site (Figure 2.1) is located at the mouth of the “Riera de Argentona” (Argentona ephemeral stream), some 30 km northeast of Barcelona. The field site covers an area of some 1500 m^2

and the mean elevation is 3 m. The Argentona stream only flows during heavy rainfall episodes that occur mainly in autumn. The climate is sub-Mediterranean. According to data from the Cabrils weather station, located 7 km northeast from the site, the mean annual precipitation since 2000 is 584,1 mm. Compared to most Mediterranean areas, the precipitation is more evenly distributed throughout the year with the rainiest seasons being spring and autumn.

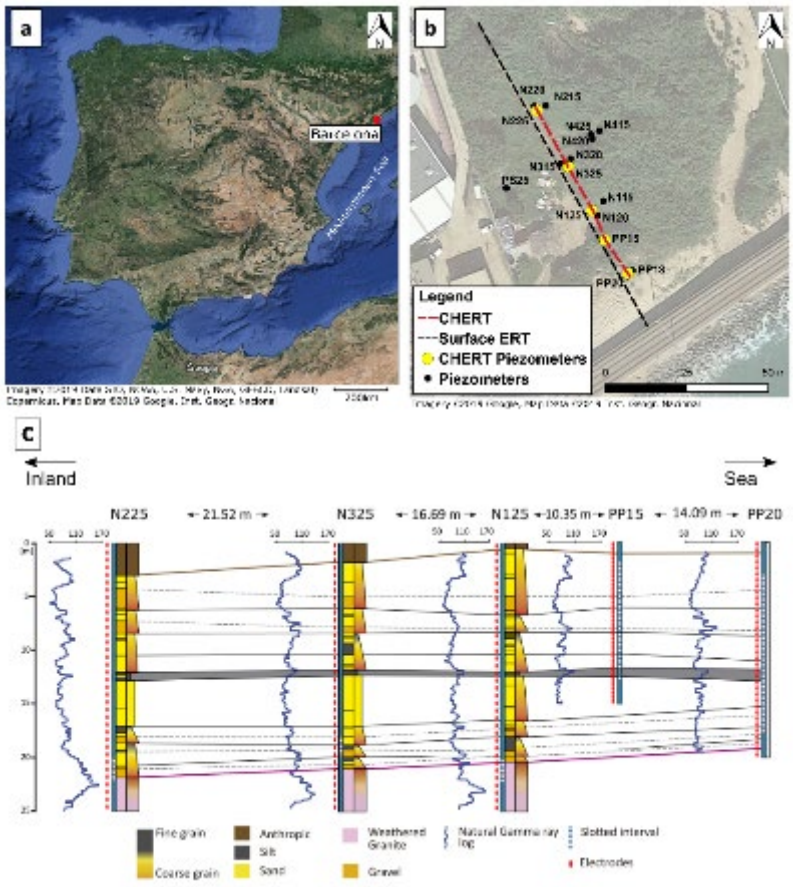

Figure 2.1 (a) Location map of the Argentona site, some 30 km northeast of Barcelona, Spain. (b) Field spread of the Argentona site, installed piezometers (black dots), piezometers equipped with electrodes (yellow dots), surface ERT and CHERT transects. (c) Vertical cross-section showing piezometers with screened depth, location of the 36 electrodes in each well and stratigraphic correlation (modified from Martínez-Pérez et al. (2019)*. Two sandy aquifers are loosely separated by a silt layer at 12 m depth. The semi-confined aquifer is underlaid by weathered granite.*

We have installed 16 piezometers in a cross-shaped distribution with the longest axis being oriented perpendicularly to the coastline (Figure 2.1a). These include four nests (N1-N4) of three piezometers with depths of 15, 20 and 25 m (N115, N120, N125, etc.), screened over 2 m at the bottom. The distance from the closest piezometer (PP20) to the coastline is almost 40 m.

The field site is located on a coastal alluvial aquifer that overlies a granitic basement (Figure 2.1b). Core analyses reveal that the sediments are mostly unconsolidated. Martínez-Pérez et al. (2019) identify two sequences, located above and below a silt layer at -9 m a.s.l. The upper and lower sequences display a fining-upward pattern. The granitic basement was found at -17 to -18 m a.s.l in piezometers N225, N325 and N125, with signs of intense weathering. A well-correlation profile was built from core descriptions supported by gamma-ray and induction logs. The silt layer at -9 m a.s.l

appears to be continuous along the main transect between piezometers N225 and PP20. Its continuity, especially towards and below the sea and its low permeability nature are yet to be defined. The present 2D conceptual model of the site is simple and several questions remain unanswered: Is the silt layer continuous and impervious or is a significant water flow passing through it? Is the weathered granite an aquitard or another permeable unit given its strongly weathered nature? (see, e.g. Dewandel et al. (2006)). One of the goals of our time-lapse CHERT investigations is to contribute to answering these open questions and improve the conceptual understanding of the site.

2.3 CHERT experimental setup

The objectives of the time-lapse CHERT experiments are to image SWI in order to improve the geological conceptual model, and to infer SWI dynamics. This requires installing metal electrodes in a corrosive saline environment, in which electrolysis due to current injection further accelerates the corrosion process and limits the lifetime of the installation. Therefore, addressing corrosion was a main concern when designing the system and planning the monitoring experiments. The impact of corrosion on the electrode-functioning was tested in the laboratory before field deployment. The parts that are most sensitive to corrosion are the connection points between the mesh electrodes and the copper cables that bring current. Our strategy to delay corrosion at the connection points was to tie together the mesh and the cable, and to cover the connection point by a double silicone layer to prevent contact with water. In the laboratory, the electrodes showed signs of corrosion after 500 hours of full contact with saline water (55 mS/cm), under a constant current injection of 1A at a frequency of 3 Hz. In our setup, stainless-steel mesh electrodes were permanently attached to the outside of the seven deepest PVC piezometers (Figure 2.2a). When conducting a CHERT, the injected current is less than 1 A and the time of injection is a fraction of a second. Based on these laboratory test results, it was suggested that the instrumentation would last for at least two years, which was the minimum desired duration of the experiment.

All piezometers have 36 electrodes and the distance between electrodes is 70 cm, 55 cm and 40 cm in the 25 m, 20 m and 15 m depth piezometers, respectively. Numerical simulations by al Hagrey (2011) suggest that satisfactory resolution can be achieved using aspect ratios (horizontal distance between the boreholes and their depths) up to 2 for different scenarios by fixing constraints about the resistivity structures during the inversion procedure. In the Argentona site, the aspect ratio for the different borehole pairs considered ranges from 0.6 to 0.8. Further details on the set-up and installation are described by Folch et al. (2019).

When performing ERT, we measure an “apparent” resistivity that depends on the geometry of the acquisition. The apparent resistivity is related to measured electrical resistances:

$$\rho_{app} = \frac{K}{VI} \tag{2.1}$$

where ρ_{app} is the apparent resistivity, K is a geometric factor that depends on the electrode array and site characteristics, V is the voltage between two electrodes measured during current injection and I is the magnitude of the current flowing between an other pair of electrodes. Any electrode configuration or array can, in principle, be used to perform ERT at the surface or between boreholes. For surface ERT, there are many well-established array types, such as Wenner, Schlumberger, dipole-dipole, or pole-pole. For CHERT, several studies have sought to determine the most informative and cost-effective arrays for monitoring dynamic processes (Bellmunt et al., 2012; Zhou and Greenhalgh, 2000). Bellmunt et al. (2016) suggest that it is better to use different configurations (dipole-dipole, pole-tripole and Wenner) with different sensitivity patterns in order to obtain the maximum information about the subsurface. Moreover, given the corrosive environment in which the steel electrodes were installed, we decided to maximize the number of data measurements to ensure enough

repeatability for the time-lapse inversion. The different configurations used were already described and assessed by Zhou and Greenhalgh (2000) and Bellmunt et al. (2016). Figure 2.2b shows the electrode configurations used at the Argentona site: dipole-dipole, pole-tripole and Wenner. Note that these data are acquired sequentially by considering one pair of neighboring boreholes at the time.

We use an optimized survey design that allows more than 5800 data points to be acquired in less than 30 minutes. After the installation of the electrodes around the casings (36 at each borehole), the data acquisition process was straightforward, with no need for large additional costs in maintenance or human working time. The equipment used was a Syscal-Pro multi-channel (10-channel) system from IRIS instruments with 72 electrodes. The current injection time was 250 ms, and stacking of up to 6 measurements was done to meet data quality requirements. It took 2 hours to complete the 4 CHERT acquisitions needed to cover the whole 2D transect from boreholes N225 to PP20. The combination of four such sections are referred to as a complete CHERT.

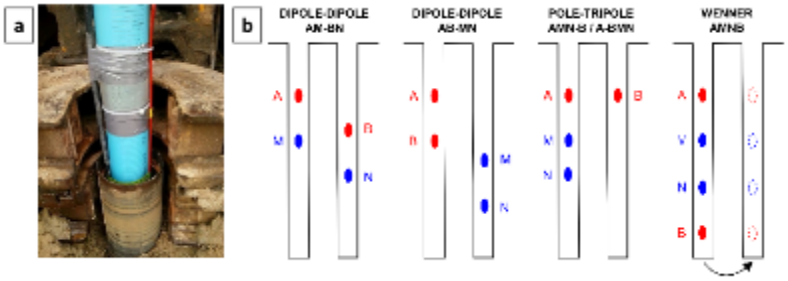

Figure 2.2 (a) Stainless-steel meshes (electrodes) permanently fastened around PVC piezometers for time-lapse CHERT experiment during piezometer installation. (b) Electrode configurations used in the survey. A total of 5843 measurements are recorded per CHERT in less than 30 minutes. Data is acquired sequentially by considering one pair of neighbouring boreholes at the time. 4 CHERT are needed to build a complete CHERT, the whole 2D transect from boreholes N225 to PP20.

2.4 Processing and inversion methods

Sixteen time-lapse datasets were collected during two years (five in 2015, eight in 2016, and three in 2017), corresponding roughly to a complete CHERT every 90 days. This relatively low sampling interval was partly motivated to decrease corrosion of the electrodes due to repeated current injections.

Data pre-processing was needed to remove anomalous and erroneous data points prior to imaging. Comparison of normal and reciprocal measured resistances is a common technique for appraising data errors (Flores-Orozco et al., 2012; Koestel et al., 2008; LaBrecque et al., 1996; Oberdörster et al., 2010; Slater et al., 2000). We follow the strategy proposed by Bellmunt and Marcuello (2011) for the quality control of the data based on the comparison between normal and reciprocal measurements. We chose a threshold of 10% difference between the normal and reciprocal data in order to keep the measurement. Furthermore, the electrical contact resistance between the electrodes and the subsoil was checked before each data acquisition. Although the specific values of each pair of electrodes were not recorded, they were low in general. The deepest electrodes, in contact with the SWI, had contact resistances values in the order of 1 kohm and the ones closer to the surface had values of a few tens of kohm.

Pseudo-sections of the apparent resistivities are easily created for surface ERT surveys, but there is no corresponding visualization technique for CHERT surveys. Instead, we plot geometric factors, apparent resistivities, and data errors versus data number, to identify electrode configurations with anomalous values. Clearly, for time-lapse studies it is important to ensure that changes observed are

due to subsurface processes, and not to changes in the survey setup. Consequently, the sixteen datasets were scanned and compared to keep only identical electrode configurations.

For inversion, we make the common assumption that the bulk EC distribution is constant in the direction perpendicular to the complete CHERT transect. The corresponding 2.5D electrical inverse problem is solved on an unstructured mesh with tetrahedral elements using BERT (Boundless Electrical Resistivity Tomography) (Günther et al., 2006; Rücker et al., 2006) and pyGIMLi (Generalized Inversion and Modeling Library) (Rücker et al., 2017). The inversion algorithm inverts the log-transformed apparent resistivities, into a 2D log-transformed electrical resistivity distribution. The objective function to minimize is:

$$\varphi = \varphi_d + \lambda\varphi_m = \left\|\boldsymbol{C_d^{-0.5}\Delta d}\right\|^{\boldsymbol{n}} + \lambda\left\|\boldsymbol{C_m^{-0.5}\Delta m}\right\|^{\boldsymbol{n}} \quad (2.2)$$

where $\varphi_d$is the data misfit term, $\boldsymbol{\Delta d} = \boldsymbol{d} - \boldsymbol{f}(\boldsymbol{m})$is the vector containing data residuals; with $\boldsymbol{d}$ a vector containing field data; $\boldsymbol{f}(\boldsymbol{m})$ the forward response of the geoelectrical problem using model $\boldsymbol{m}$, and n is the order of the norm. In order to make the inversion less sensitive to data outliers, we apply a L1-norm mimicking scheme to the data misfit term using iteratively reweighted least squares (ILRS) (Claerbout and Muir, 1973). We assume uncorrelated data errors, so $\boldsymbol{C_d^{-0.5}}$ is a diagonal matrix with entries containing the inverse of the relative resistance errors. A relative error model with a 3% mean deviation is further assumed. $\boldsymbol{\Delta m} = \boldsymbol{m} - \boldsymbol{m^{ref}}$ is the vector being penalized in the model regularization, with $\boldsymbol{m}$, the vector of estimated parameters; and, $\boldsymbol{m^{ref}}$, a vector of reference parameters. $\boldsymbol{C_m^{-0.5}}$ is the model regularization matrix. Smoothness operators are frequently used but are not suitable for capturing the sharp resistivity changes expected at the interface of the saltwater intrusion. We have chosen to define $\boldsymbol{C_m}$ as a geostatistical operator (Chasseriau and Chouteau, 2003; Hermans et al., 2012; Linde et al., 2006), containing site-specific information about how the resistive bodies are expected to correlate in space. Hermans et al. (2016) provide an example of how the inclusion of covariance information in ERT inversion improves the imaging of the target in terms of shape and amplitude, creating more realistic images. For this purpose, we use an exponential covariance model implemented in pyGIMLi by Jordi et al. (2018). The spatial support of the geostatistical operator helps to reduce the tendency of anomalies being clustered around the electrode region where sensitivities are high. The parameters used in the covariance model were chosen in agreement with the expected groundwater processes. Pore water is expected to flow through the horizontal layers shown in the stratigraphic correlation, so the variations that we expect to observe will be more correlated in the horizontal direction than in the vertical direction. The integral scales in the horizontal and vertical direction are 10 m and 2 m respectively, the anisotropy angle is 90º and the variance of the logarithm of the resistivities was set to 0.25. The detailed description of this type of covariance model is found in, for example, Kitanidis (1997).

The minimization of φ is performed iteratively using the Gauss-Newton scheme. We start the inversion with a homogeneous model corresponding to the average apparent resistivity. In Equation 2, λ is the regularization parameter. We apply an Occam type inversion, in which we seek the smallest φ_m while fitting the data (Constable et al., 1987). We set λ to a high value at the first iteration and decrease it by 0.8 in each subsequent iteration. The iterative process is stopped when the data are fitted to the noise level.

To study variations in time, the simplest approach consists of inverting independently each dataset to analyze the evolution of changes. This approach may work when changes are large, but it is not considered state-of-the-art because inversion artifacts tend to be time independent (though not always, see discussion by Dietrich et al. (2018) and may mask actual changes. Singha et al. (2014) review time-lapse inversion as a way to impose a transient solution constraint through the analysis of differences or ratios in the data (Daily et al., 1992; LaBrecque and Yang, 2001), through the differentiation of multiple individual inversions (Loke, 2008; Miller et al., 2008), or through temporal

regularization (Karaoulis et al., 2011). Daily et al. (1992) introduced the ratio inversion, in which data are normalized with respect to a reference model represented by a homogeneous half space. The method allowed qualitative interpretation of resistivity changes, but made quantitative interpretation difficult. This motivated "cascaded inversion" (Miller et al., 2008), which consists of selecting as reference model the result of an initial inversion or baseline dataset. This approach removes the effects of errors and yields more reliable sensitivity patterns (Doetsch et al., 2012). The difference inversion by LaBrecque and Yang (2001) assumes that the changes from one acquisition to another are small, but this is not the case throughout the two years of monitoring at the Argentona site. In the newest approaches, a 4D active time constrained inversion is applied simultaneously to all datasets (Karaoulis et al., 2011) penalizing differences between models. Although this is the most novel procedure for time-lapse inversion, it is computationally demanding. We have decided to apply the "ratio inversion", solving for the updates of a reference model, thereby, allowing us to account for the leading non-linear effects.

For data at time-lapse t, φ_d is:

$$\varphi_d = \left\| \boldsymbol{C_d^{-0.5}} (\boldsymbol{d^t} - \boldsymbol{f}(\boldsymbol{m^{ref}}) \frac{\boldsymbol{d^t}}{\boldsymbol{d^{ref}}}) \right\|^{\boldsymbol{n}} \qquad (2.3)$$

where $\boldsymbol{d^t}$ is the data vector at time $\boldsymbol{t}$, $\boldsymbol{f}(\boldsymbol{m^{ref}})$ is the calculated forward response of the geoelectrical problem using a reference model $\boldsymbol{m^{ref}}$, and $\boldsymbol{d^{ref}}$ is the data vector of reference time $\boldsymbol{t^{ref}}$.

The reference model for time-lapse inversion was built by inverting data from a complete CHERT and surface ERT from September 8, 2015. The surface ERT dataset consists of 1600 data points acquired along the transect shown in Figure 2.1a. We used the Wenner-Schlumberger configuration with 72 electrodes and a 1.5 m electrode spacing. Inversion results are displayed in the next section in terms of bulk electrical conductivities, σ_b (the reciprocal of resistivities ρ_b).

2.5 Results

2.5.1 Reference Model

Inversion results of data used to establish the reference model are shown in Figure 2.3. We display the bulk EC model obtained by the inversion of the CHERT and surface-based ERT data (Figure 2.3a), the result obtained when only considering the complete CHERT (Figure 2.3b) and only the surface ERT (Figure 2.3c) next to the calculated coverages for each model (Figure 2.3d-f). The bulk EC model obtained from the surface ERT campaign shows resistive layers in the first 5 to 10 m below the land surface, while the model obtained from the complete CHERT data alone is unable to resolve them. The complete CHERT, however, shows high conductive anomalies at depth. Also, the magnitude of the bulk EC below -10 m a.s.l is higher in the complete CHERT model. These results confirm the expectations derived from the literature described in the introduction. Surface ERT is unable to accurately image the magnitude of saline regions at depth. Figure 2.3e and Figure 2.3f display the coverage of the CHERT and surface ERT acquisitions computed using the cumulated sensitivity. The maximum coverage is attained near the electrodes. By combining the two datasets, the inverted bulk EC model has high sensitivity near the surface and in depth. The complementarity of the two surveys is well illustrated in Figure 2.3d. For the reference model of the time-lapse inversion, we chose the inversion result from the complete CHERT dataset and the surface dataset (Figure 2.3a).

Figure 2.4 shows the reference model with the site stratigraphic correlation. The estimated bulk electrical conductivity ranges from 1 to 1000 mS/m. A resistive layer of less than 5 mS/m is visible in the top 3 m, starting 60 m from the sea. This layer with low bulk EC is caused by the unsaturated zone; it coincides with the depth to groundwater (gray dotted line in Figure 2.4) that usually vary between 0

to 0.5 m a.s.l. The thickness of the unsaturated zone is resolved thanks to the surface ERT data. The bulk EC grows to a mean value of 50 mS/m below the water table in the shallow aquifer from 0 to -10 m a.s.l. Conductivity grows further, exceeding 500 mS/m, below -10 m.

Bulk electrical conductivity values above 200 mS/m can here be conclusively attributed to the presence of seawater in the pore space. We see an upper conductive anomaly of some 100 mS/m in the unconfined aquifer above -5 m a.s.l towards the sea (from 35 m to 50 m to the coast). We attribute this anomaly to beach sediments saturated with a mixture of fresh and saline water. The upper anomaly vanishes inland before piezometer PP15. The second conductive anomaly, below -10 m a.s.l, extends from 35 m to 90 m to the coast, and it vanishes before reaching piezometer N225. Poor imaging resolution is not expected at this depth, so we must consider the possibility that lithological heterogeneity or lower water salinity causes the change in bulk EC in the lower aquifer. In the bottom part of Figure 2.4, bulk EC decreases where the top of the granite is found in piezometer N125.

The reference model and stratigraphic units provided insights pertaining to the interpretation of subsurface processes. Time-lapse changes will help confirming whether conductivity anomalies in the reference model are related to fluid dynamics or to geologic structures.

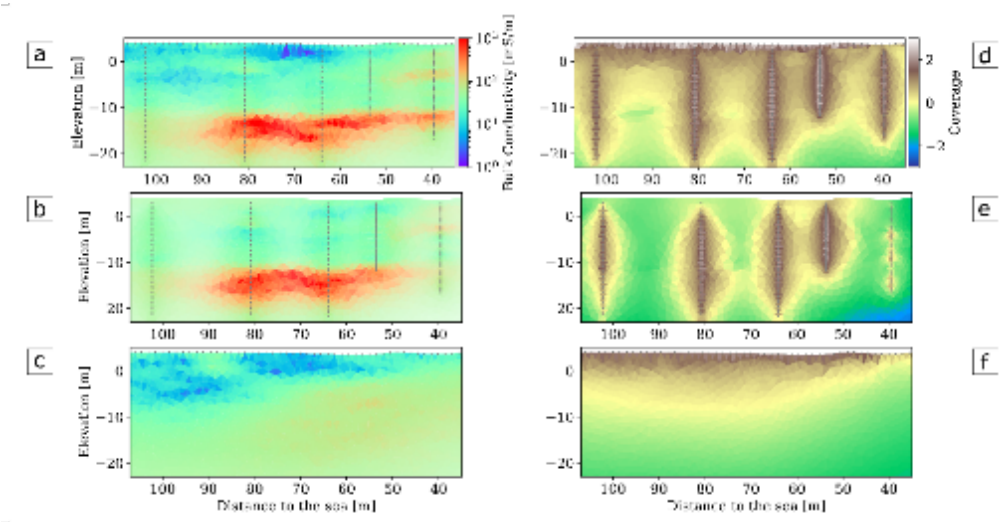

Figure 2.3 Bulk electrical conductivity models obtained by the inversion of the CHERT and surface-based ERT data (a), the result when only considering the complete CHERT (b) and only the surface ERT (c) with the corresponding calculated coverages for each model (d-f). The complete CHERT model shows conductive anomalies (in red), which are not shown by the surface ERT model. The inversion of both datasets combines the coverages and yields an image with higher resolution near the surface and in depth (d).

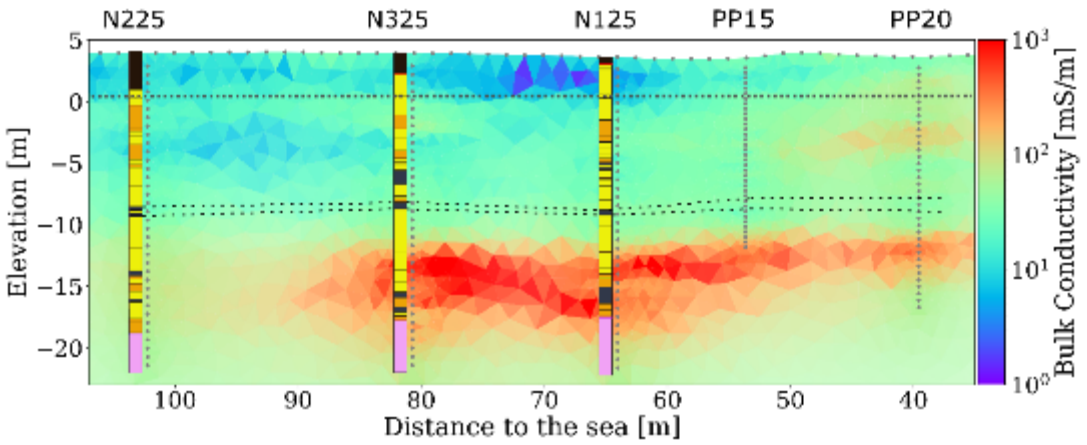

Figure 2.4 Result from the inversion of surface and cross-hole ERT (dataset from September 8th, 2015). Stratigraphic columns are shown to relate stratigraphic units with bulk conductivities. Grey dots represent the electrodes around the boreholes and on surface. Grey dashed line indicates the approximate groundwater table. Black dashed line indicates the silt layer. This cross-section is used as reference model in the time-lapse inversion.

2.5.2 Time-lapse results

Figure 2.5 shows the time evolution of the data percentage that satisfies the constraints on data quality (less than 10% percent of difference between normal and reciprocal measurements). The panel between boreholes PP20 and PP15 is the one that suffers the most from discarded data, likely due to its proximity to the coast and it is the zone where lower resistivities cover a thicker vertical zone. The decrease in data quality with time is probably related to corrosion processes of the electrodes in contact with marine water. The quality control after each acquisition, plus the identical geometry constraint for the time-lapse inversion, reduced the data set to 2677 identical measurements that were extracted from each complete CHERT.

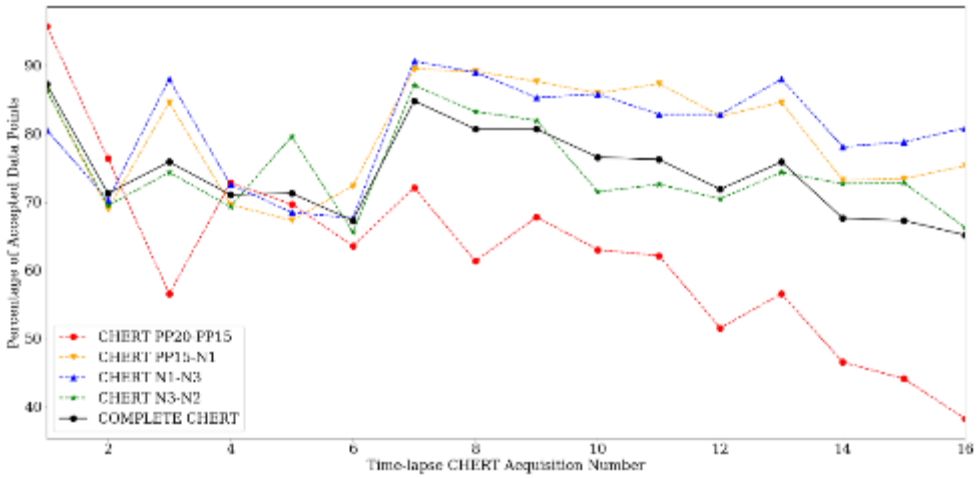

Figure 2.5 Percentage of accepted data points in each CHERT, after quality control during data pre-processing. Note the decrease in the amount of accepted data with time, most likely due to corrosion of the electrodes, particularly in the PP20-PP15 panel, which is located the closest to the sea.

Time-lapse results are displayed in Figure 2.6 as the ratio between each bulk EC model and the bulk EC of the reference model (September 2015). The color scale in the figure varies from a twofold

increase (dark red) to a decrease by half (dark blue) in bulk EC with time. The color scale does not show the minimum and maximum magnitude of the variations; it was chosen to highlight major changes in the two years of monitoring. In the imaging process, the use of a geostatistical operator in model regularization helped in removing the boreholes' footprint in the bulk EC models, but these remain in the ratio images due to the high sensitivity of the method near the electrodes. Figure 2.6a (ratio of September to July 2015 ECs) shows an increase in bulk EC during summer 2015. That is, EC is smaller in July than in September, which suggests advancement of salinity. From October 2015 to March 2016 (Figure 2.6c-g) an increase is successively observed near PP20, reaching 70 m from the sea. In March, April and May 2016 (Figure 2.6g-i), a decrease in bulk EC is observed in both aquifers. Complete CHERT from June 2016 to September 2017 (Figure 2.6j-l) show successive increase in the conductivity of the semi-confined aquifer, below -10 m a.s.l. In 2017 (Figure 2.6m-l), a highly conductive anomaly reappears in the upper right part of the time-lapse ratio images between nest N3 and borehole PP20. This is the largest anomaly captured by the experiment in size and magnitude. In the last ratio image between September 2017 and September 2015 (Figure 2.6l), the increase in bulk EC in the study area is clearly observed.

We analyze below the origins of long-term and short-term changes described in the previous paragraph by correlating them with precipitation and wave activity data. The precipitation and the wave activity data are here used as a proxy to indicate the likely timing when a significant freshwater recharge occurred and when water from large waves might have formed seawater ponds at the surface.

Figure 2.7 displays the average conductivity of the inverted model at -8 m a.s.l, -12.5 m a.s.l and -16 m a.s.l. In this figure we also display daily precipitation data from the Cabrils Station, located 7 km northeast of the site. Precipitation data (inverted y-axis) shows two relevant features: (1) important precipitation events can occur in one day (e.g., 220 mm in October 2016); (2) the rainiest periods during the 2 years of monitoring consistently occurred in the fall and spring. The winter and summer of 2016 were the driest periods. Wave-related data (normal y-axis) is obtained from a numerical model called SIMAR 44 (Pilar et al., 2008). The numerical model is calibrated using data from wave buoys distributed along the Catalan coast. Wave numerical models have limitations, and tend to underestimate wave height near the coast, but they give general insights about the wave activity (WAMDI Group, 1988). In Figure 2.7, we show the significant wave height from the numerical model. Significant wave height (Hs) is defined as the average height of the highest one-third waves in a wave spectrum (Ainsworth, 2006), and it is the most commonly used parameter because it correlates well with the wave height that an observer would perceive. The wave data show increased wave heights in Autumn 2015, January 2016 and Winter 2017. These periods correspond to the appearance of a superficial conductive anomaly in the upper part of the time-lapse images.

The plots of average bulk EC in Figure 2.7 capture the evolution of the conductivity in the unconfined and the underlying semi-confined aquifer over time. The mean bulk EC of the upper portion of the lower aquifer (at -12.5 m a.s.l) displays a more than twofold increase (from 200 mS/m to more than 500 mS/m) in the two years of monitoring. We can also observe cyclic variations throughout the year. In contrast, both fluctuations and overall variation are very small in both the shallow (bulk EC around 20 mS/m) and greater (some 300 mS/m) depths.

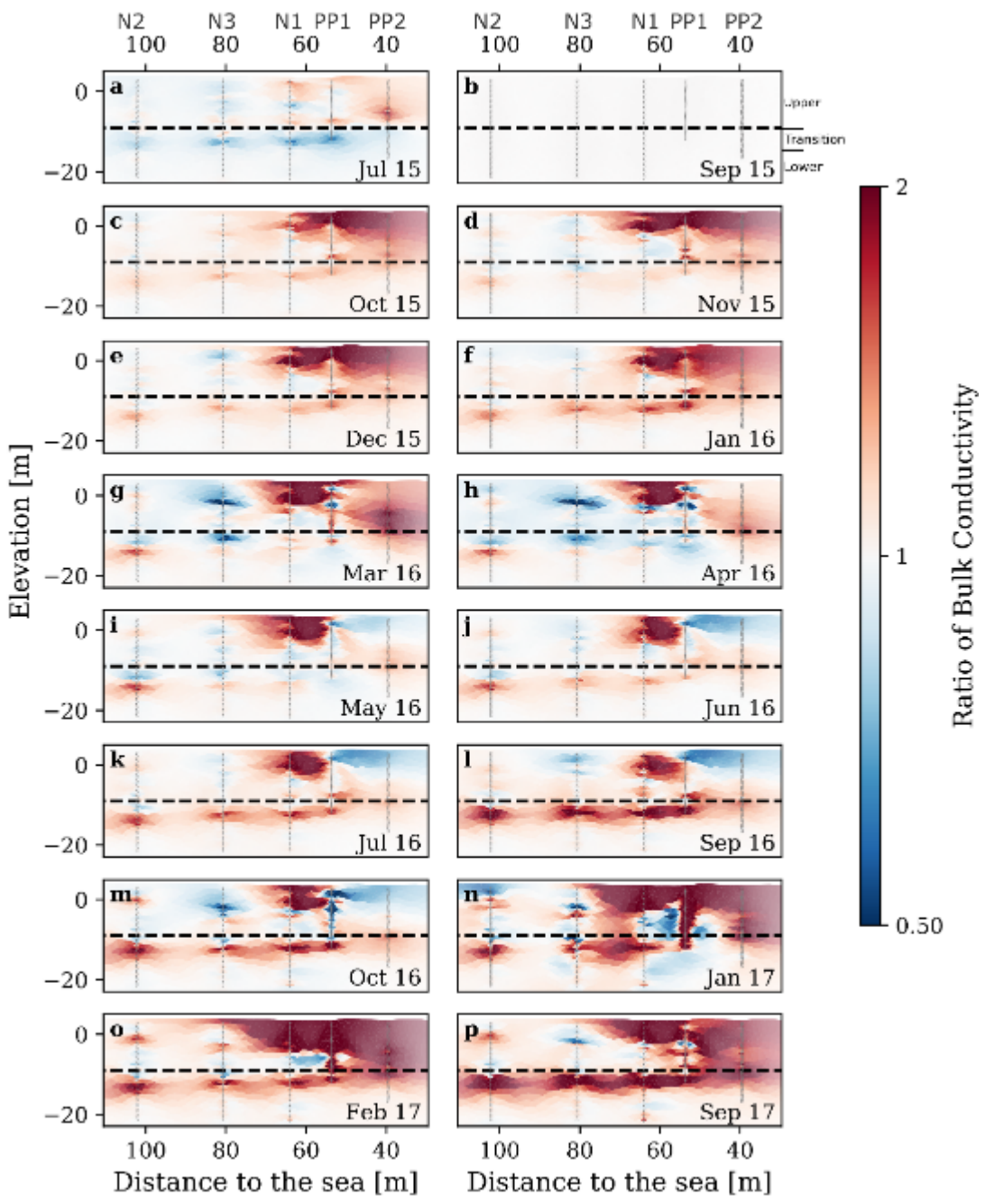

Figure 2.6 Results from the time-lapse inversion of 16 complete CHERT acquired during 2 years (July 2015 through September 2017). Images display the ratio of bulk electrical conductivity with respect to September 2015 (a brownish area implies higher EC and, therefore, salinity than in September, 2015). The silt layer is indicated with a dashed line. Note the increase in bulk EC in the upper-right side (<80 m of distance to the sea), and along a line just below the silt layer, indicating a rise in the saltwater interface.

In order to assess the impact of a heavy rain event at the site, we have computed the ratio of the CHERT bulk EC models from September 30, 2016 and October 21, 2016, 11 days before and 9 days after the heavy 220 mm precipitation. The color scale chosen for the Figure 2.8a differs from previous figures to improve visualization of the bulk conductivity variations. Figure 2.8a displays the conductivity ratio image, which reveals a decrease in the conductivity throughout the saturated zone, both above and below the -10 m a.s.l. silt layer, and an increase in the unsaturated zone, above the 0 m a.s.l, between nest N3 and PP20. No difference is observed below -15 m a.s.l. The decrease in

conductivity observed along borehole PP15 is most likely related to water flowing along the borehole (the site was flooded). Heads measured in piezometers N115 (black) and N120 (blue) are shown in Figure 2.8b, showing that hydraulic heads increased 60 cm in nest N1 during the rain. Rain was accompanied by an increase in the significant wave height. After 10 days, when the complete CHERT was acquired, groundwater level had already dropped by 30 cm.

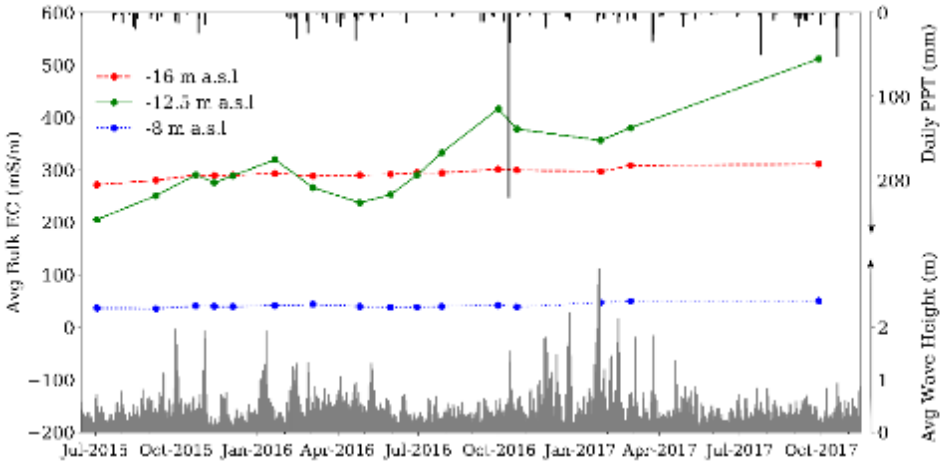

Figure 2.7 Average conductivities extracted from the inverted models, at -8 m a.s.l (blue), -12.5 m a.s.l (green) and -16 m a.s.l (red). Precipitation (PPT) data from Cabrils station and simulated significant wave height time-series are displayed. The points indicate times of CHERT campaigns. Note that acquisitions were made before and after the 220 mm precipitation event of October 12, 2016. Significant seasonal fluctuations and an overall increase of EC can be seen in the upper part of the semiconfined aquifer (elevation of -12 m a.s.l), but are negligible in the lower portion of both the shallow unconfined aquifer (-8 m a.s.l) and the semi-confined aquifer (-16 m a.s.l).

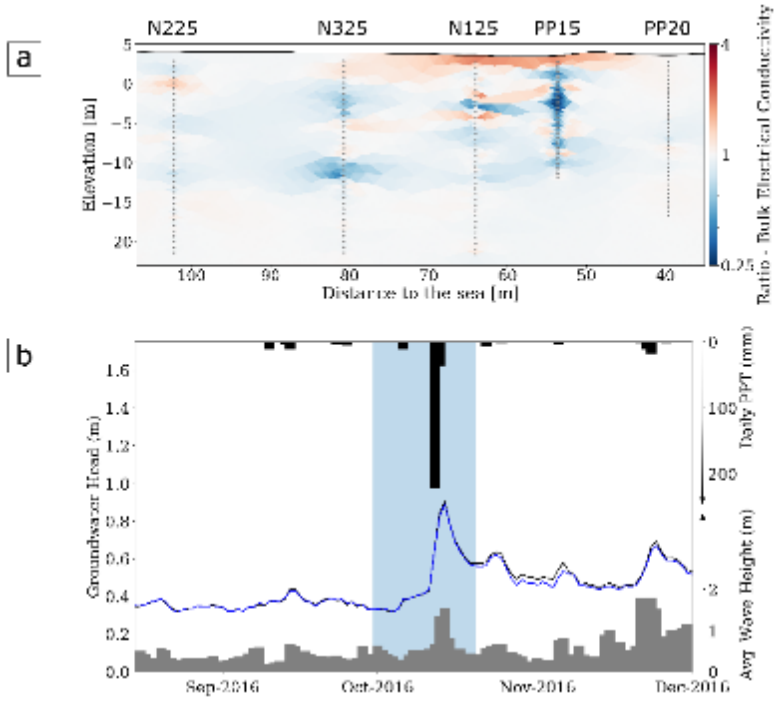

Figure 2.8 (a) Ratio between the bulk electrical conductivity model of September 30 and October 21, 2016. The heavy rain occurred on October 12, 2016. The image shows a decrease in conductivity in the unconfined and semi-confined aquifer and a conductivity increase in the unsaturated zone on both sides of nest N1. The decrease in conductivity observed along borehole PP15 is attributed to freshwater infiltration due to borehole construction. (b)

Time-series of groundwater level in boreholes N115, average significant wave height (grey bars) and precipitation (black bars). Highlighted is the heavy rain event of 220mm that occurred on October 12, 2016. The event was accompanied with an increase in groundwater level and in significant wave height.

A clear change observed in time-lapse images of Figure 2.6n-p is the increase in bulk EC in the shallow layers during the winter of 2017. This increase in bulk EC occurs at a time of higher wave activity, as shown by Figure 2.7. To quantify the amount of the increase in conductivity, we compute the ratio of the bulk EC of CHERT from October 2016 (the last tomography before winter) and February 2017 (a tomography during winter and the high waves period). The result from the ratio is displayed in Figure 2.9a. Again, the color scale of the figure is adapted to better visualize the variations. EC increased by 200-500% from 80 m to 35 m from the coastline, between nest N3 and borehole PP20. The increase in conductivity observed along borehole PP15 is, again, most likely related to water flowing along the borehole. Figure 2.9c shows the recovery of the bulk EC in the shallow layers around PP20 in September 2017.

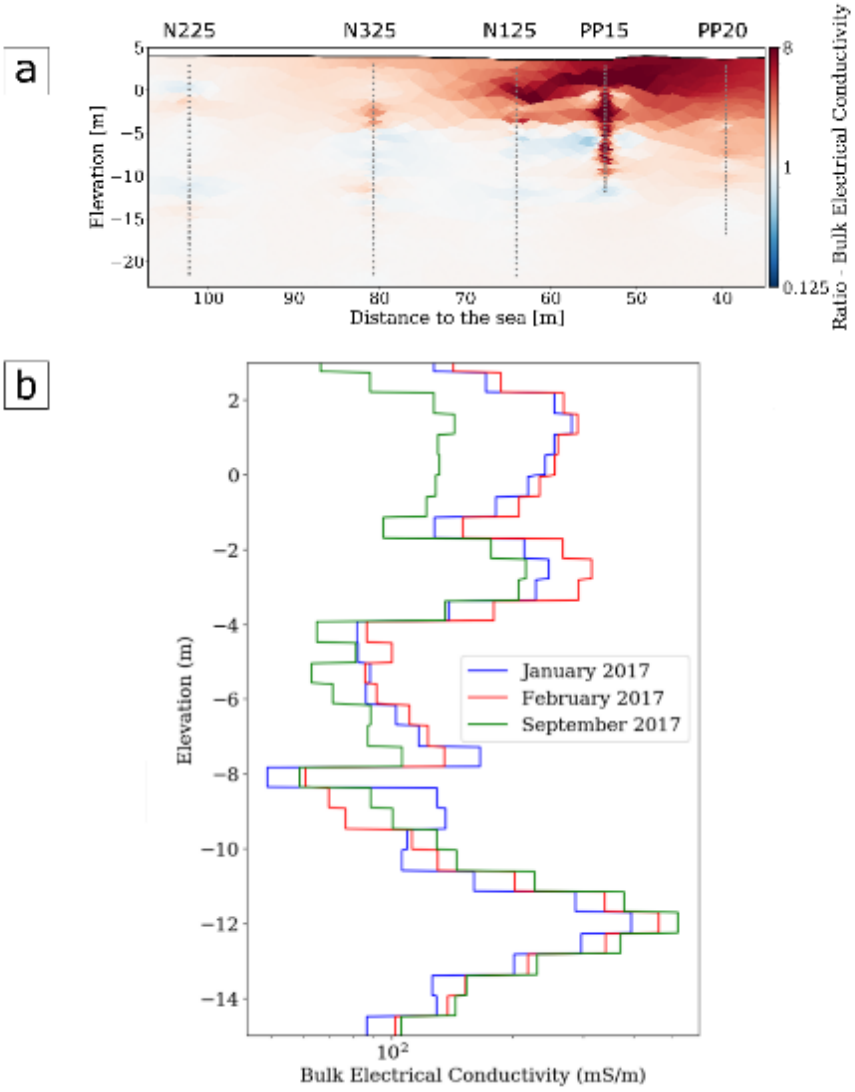

Figure 2.9 (a) Ratio of October 2016 to February 2017 CHERT ECs. (b) Extraction of CHERT bulk EC profiles along PP20. The winter period with higher significant wave heights is marked by a twofold increase in bulk electrical conductivity values from the coastline until 90 m from the coastline. The extractions in (b) show the bulk EC in the upper layers during winter (200 mS/m), and the recovery 6 months after winter (100 mS/m). The extractions also evidence the increase in conductivity in the lower aquifer.

Measurements of water EC from water samples are displayed in Figure 2.10. Piezometers from nests are screened at different depths, and we have grouped them in three categories: N115, N215, N315 and N415 are in the "upper" group (colored in blue), because the screening depth is above -10 m a.s.l; N220, N320 and N420 are in the "transition" group (colored in green), with the screen around -12.5 m a.s.l, thus, just above the saltwater intrusion; and, N120, N125, N225, N325 and N425 in the "lower" group (colored in red), with the screen below the transition zone, where saltwater is considered to be concentrated. Similar to the plots of average bulk EC from complete CHERT in Figure 2.7, the major changes occur in the "transition" group, with an increase of water EC by 300%, from 1000 mS/m to 3000 mS/m in the two years of monitoring. Apart from the increase in water EC observed in N115 (screened interval at -9.9 m a.s.l), no clear variations are observed in the "upper" and "lower" groups. Note that N120 has higher conductivity values than N125, which suggests that a freshwater source is present or a desalination process is occurring below -18 m a.s.l.

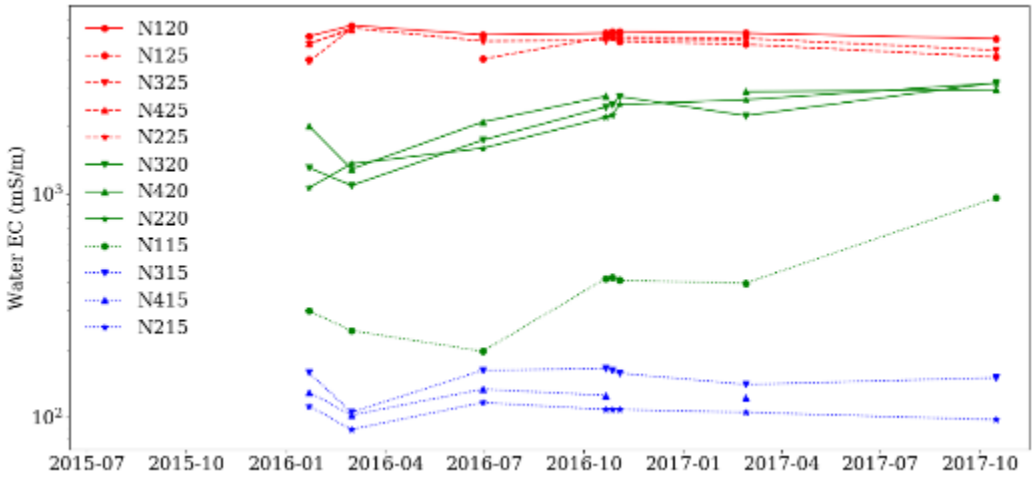

Figure 2.10 Water electrical conductivity measurements taken on water samples from piezometers in nests N1, N2, N3, and N4. The piezometers are grouped according to the elevation of the screened intervals: "upper" (blue, -7 to -10 m a.s.l), "transition" (green, -11.5 to -13.5 m a.s.l) and "lower" (red, -15.5 to -18.5 m a.s.l), where EC is that of seawater.

Figure 2.11 displays the precipitation history recorded at the Cabrils station, 7 km northeast from the site. The annual precipitation from 2000 to 2017 is plotted in gray. The black bar of year 2016 refers to the heavy singular 220 mm rain event, which causes that year to look wet but produces floods rather than proportional recharge. Average yearly precipitation since 2000 is 584,1 mm. 2015 was the driest year of the sequence with only 355 mm of precipitation (38% lower than average). Actually, rainfall was below the long-term average during the last three years of monitoring. The 2015 to 2017 drought is the likely cause for the overall increase in the aquifer bulk electrical conductivity, due to the decrease in freshwater recharge.

The reliability of bulk electrical conductivity models obtained with the CHERT experiment can be evaluated using other independent datasets. Induction logs (IL) acquired at the Argentona site also provide bulk EC models. Induction logs were done using the GEOVISTA EM-51 electromagnetic induction sound. Figure 2.12 displays a comparison of the bulk EC from IL along piezometers N2, N4, N3 and N1 (from left to right) and extractions from the complete CHERT conductivity models along the same piezometers. N4 is not on the complete CHERT transect, but as we neglect heterogeneity perpendicular to the transect, we assume nest N4 is comparable to nest N3. IL were not performed in the 25 m deep piezometers because the stainless-steel electrodes installed outside the casing severely corrupted the recorded signal. Instead, they were performed in neighboring 20 m deep piezometers that do not contain any electrodes. IL from May 2015 (light blue), before the beginning of the CHERT

experiment are available for all piezometers. They are compared with the CHERT conductivity model from July 2015 (dark blue). In Figure 2.12c, an IL from July 2016 in nest N3 is compared with CHERT conductivity model from the same month. In Figure 2.12b, an IL from October 2017 in nest N4, conducted two weeks after the end of the CHERT experiment, is displayed with the CHERT conductivity model from September 2017 of nest N3. CHERT conductivity model can be well correlated with the IL from all piezometers. There are differences in the magnitudes of the bulk EC, but both methods agree on the location of the transition zone, from -10 to -12 m a.s.l.

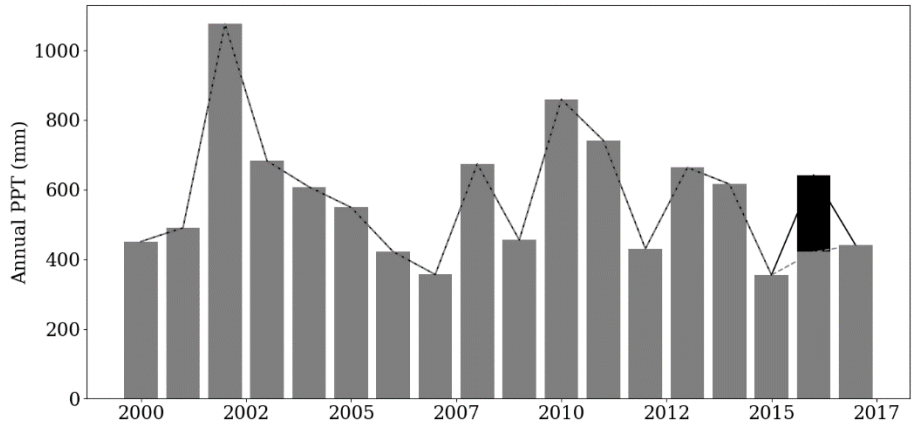

Figure 2.11 Annual precipitation since 2000 from Cabrils weather station, 7 kilometers northeast from the site. Average precipitation is 584,1 mm (dashed line). Note that the monitoring period is below the average. The black bar in 2016 represents the 220 mm rain event of October 12, which probably produced relatively less recharge than typical rainfalls.

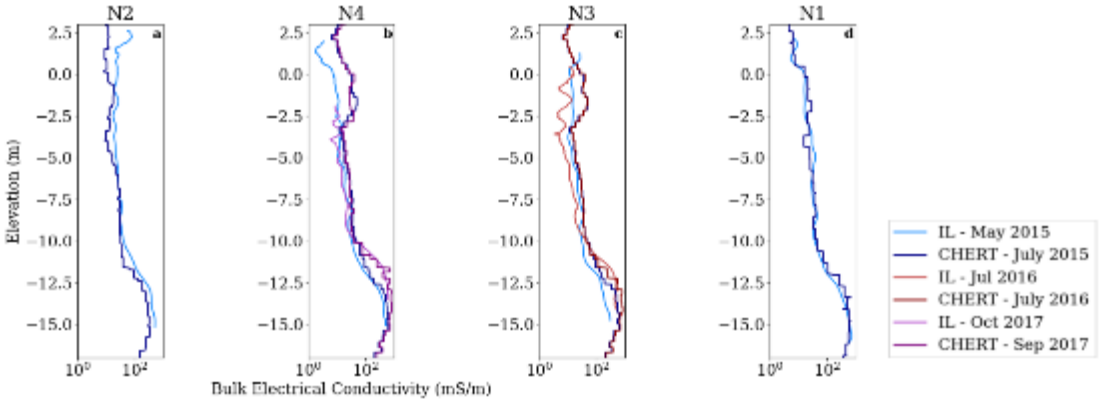

Figure 2.12 Comparison of bulk electrical conductivity models obtained from induction logs and CHERT along piezometers in nests N2 (a), N4 (b), N3 (c) and N1 (d). The CHERT logs were extracted from the CHERT bulk EC models along the boreholes.

2.6 Discussion

2.6.1 Surface ERT vs. CHERT

Surface ERT reflects quite accurately the thickness of the unsaturated zone and the location at which the water becomes more saline, but it is impossible to image the difference between the transition zone and the actual saltwater intrusion. Using only the surface ERT bulk conductivity model,

one could argue that SWI in the Argentona site displays the paradigmatic saline wedge shape of Abarca et al. (2007) or Henry (1964). Instead, the CHERT data model suggests two conductive anomalies, one in the unconfined aquifer towards the sea, and one in the semi-confined aquifer below the –10 m a.s.l. silt layer.

An important magnitude difference is observed between surface ERT and complete CHERT bulk EC models. The surface ERT model shows much lower bulk EC in the saltwater zone than the complete CHERT model. Studies trying to link hydrological and geophysical models in coastal aquifers (Beaujean et al., 2014; Huizer et al., 2017; Nguyen et al., 2009) have encountered difficulties using surface ERT-based models due to insufficient resolution at the depth of interest. This lack of resolution causes the underestimation of water EC, and thus, of water salinity. The differences in the models shown in Figure 2.4a suggest that surface ERT is not able to correctly capture the conductivity contrasts in the subsurface. This finding is confirmed by the validation of the CHERT bulk EC models with induction logs (Figure 2.12).

2.6.2 Reference model: link between bulk EC and geological conceptual model

The complete CHERT produces a quite clear picture of the link between the bulk EC model and the stratigraphic units. We can explain the presence of two saline bodies with the presence of a continuous semi-confining layer, and the existence of up to three different aquifer layers. This is relevant by itself because it was unexpected. The only geologic feature is a relatively minor but apparently continuous silt layer, which we originally discarded as relevant. Bulk EC imaging suggests that this layer may play an important role. The transition zone is not located at the depth of the silt layer. This silt layer is the one separating the unconfined from the semi-confined aquifer. It is not, however, separating the freshwater from the saltwater. The saltwater intrusion zone begins 2 to 3 m below the silt layer, thus suggesting that a significant flux of fresh water occurs below this layer. This result is consistent with sandbox experiments of Castro-Alcalá (2019) who found that relatively minor heterogeneities may cause the saltwater wedge to split.

In addition, CHERT allowed us to improve the visualization of the SWI in comparison to traditional hydrology monitoring methods. Indeed, using traditional methods the silt layer would have been completely discarded as relevant, but the CHERT made possible the visualization of a non-monotonic salinity profile that confirms the importance of the heterogeneity. Specifically, salinity profiles in fully screened boreholes (such as PP20) are always monotonic (EC increases with depth) and rarely reach seawater salinity. Our imaging points out that actual salinity is non-monotonic and leads to the suggestion that it is the flow of buoyant freshwater within the borehole what explains both the observed step-wise increase in traditional salinity profiles and the fact that salinity is below that of seawater. The process is described by Folch et al. (2019) and by Martínez-Pérez et al. (2019), but visualization is only possible by ERT (and specifically CHERT) or electromagnetic methods (e.g., induction logs).

Weathered granite was found in the cores at the bottom of N1, below -17 m a.s.l. At this depth, the magnitude of the CHERT bulk EC model decreases. We can, thus, infer that the decrease in bulk EC at the base of piezometers N325 and N225 is related to the continuity of the crystalline formation. Loss of resolution below PP20 and PP15 does not allow us to infer anything about the presence of weathered granite towards the sea. From the available data, we conclude that the decrease in bulk EC observed in the images has two causes: first, an important change in lithology from gravel to weathered granite; and, second, a decrease in water EC observed in the water samples from N125, with respect to the water sample from N120 (Figure 2.10). The water EC values from N125 samples suggest that pore water is a mixture of fresh and saltwater. The granite is, most likely, not an impervious boundary for mixing processes, but merely another source of heterogeneity in the system. The existence of a freshwater from bottom layers of the model is yet to be explored, but it is consistent with the findings

of Dewandel et al. (2006), who described frequent highly transmissive zones at the base of the weathered granite in numerous sites around the globe.

The conductive anomalies fade while moving away from the sea. Above -10 m a.s.l, the small conductive anomaly stops before PP15, and is no longer present around N325. Below -10 m a.s.l, the conductive anomaly is present until N325, but is weaker around N225. Due to the distance between piezometers N225 and N325, sensititivity of the CHERT in this panel is lower than for the rest of the borehole pairs and the decrease in the bulk EC conductivity may be related to it. Nevertheless, this diminishing trend in the bulk EC reference model coincides with water EC values from piezometer N320 being slightly higher than water EC from piezometer N220. We identify a vertical mixing zone, but also, a lateral mixing zone between nests N3 and N2.

In summary, by comparing CHERT bulk EC model, water EC measurements and the site stratigraphic columns, we are able to highlight several features. (1) The resistive anomaly observed at the top is certainly related to partial water saturation. (2) The seemingly continuous silt layer found at -9 m a.s.l in boreholes N225, N325 and N125 does not represent a freshwater-seawater boundary. The freshwater-seawater boundary appears 2 to 3 m below, which implies that the silt layer is a semi-confining layer and freshwater discharges below. (3) There are not one but two saline bodies, one in each aquifer. The lower one is a traditional one, but the upper one is more complex and will be discussed in Section 6.4. (4) The conductivity value of the most conductive anomaly below -10 m a.s.l, interpreted as seawater-bearing formations, decreases at the top of the weathered granite. This decrease in bulk EC is explained by the reduction of water EC, and by a reduction in bulk EC due to the larger electrical formation factor of the granite. (5) CHERT bulk EC models show the location of a vertical transition zone, and also the extent of a lateral transition zone.

2.6.3 Time-lapse study: long-term effects

2.6.3.1 Seasonality: the natural dynamics

The time evolution of the average bulk EC displayed in Figure 2.7 shows that there are months with a decrease in bulk EC conductivity and months with an increase in bulk EC conductivity. These months are correlated with rainy and dry periods, and also with the occurrence of storm surges. During summer and beginning of autumn, the conductivity increases slowly until the rain period starts; in autumn, during heavy rains, conductivity decreases; during winter months, conductivity increases due to sea storms; in spring, conductivity decreases, and it reaches its lowest point before the dry summer period begins again. In the deeper areas where seawater is already in place, average bulk EC does not show important variations.

2.6.3.2 The drought: long-term salinization

The time-lapse ratio image from September 2017 (Figure 2.6l), the average bulk EC at -12.5 m a.s.l (Figure 2.7) and the water EC measurements in the transition zone (Figure 2.10) indicate a clear increase of bulk EC in the lower aquifer since the beginning of the experiment.

We conjecture that this increase in water salinity is linked to the drought that started in 2015, and had not yet ended by November 2017. In recent years, drought occurs every 8 to 10 years, and last a few years. This is visible in Figure 2.11 in years 2006/2007 and 2015/2016/2017. The effect of the decrease of freshwater recharge by rainfall is observed in the experimental results, in the form of salinization of the aquifers at a distance of 100 meters from the coastline. This result is corroborated by water EC from water samples taken at the piezometers. Overall increase in bulk EC is attributed to overall increase in water EC. While this is not surprising, what may come as a surprise is the relatively slow response of salinization of SWI to weather fluctuations. No steady regime has been reached after three years and salinization continues.

2.6.4 Time-lapse study: short-term effects

2.6.4.1 The heavy rain: a freshwater event

A 220 mm - a third of the region's average annual precipitation – rainfall event lasting less than a day occurred on October 12, 2016. It was a catastrophic event that created human and material losses due to flooding. The Argentona stream is an ephemeral stream that carries water a few days each year during monsoon-like rains, typically between September and December. A rainfall of this magnitude floods the Argentona stream, and the entire experimental site.

Do the CHERT images capture the effect of the heavy rain in the coastal aquifer? Figure 2.8a displays the difference in conductivity obtained by the tomography from 11 days before the rain and 9 days after the rain. The bulk EC ratio image reveals a decrease in the bulk EC in both upper and lower aquifers. In October 2016, according to Figure 2.7, the increase in bulk EC that was taking place was interrupted after this heavy rainfall.

To understand the change in bulk EC, we must think in terms of water masses. When an important precipitation event occurs, freshwater flows through rivers and streams towards the sea. Inland, some freshwater infiltrates into the subsurface, pushing in-situ water masses down and to the sides. The displacement of "old water" creates space for the newly infiltrating fresh rainwater, and this movement enhances mixing processes. Offshore, surface and submarine groundwater discharge is occurring at the same time. The observed change in bulk EC is most likely the result of the mixture of old saltwater with rainwater in the aquifer, which creates a new water, that is still saline but less than before the rain event. However, despite the rainfall magnitude, EC changes were neither dramatic nor long lasting.

The effect of the heavy rain that lasted only a few hours supports what was said in the drought section about this rain not being representative of the region's precipitation. One sudden episode, even of this magnitude, is not enough to make a significant difference in the seawater intrusion pattern and in the aquifer's long-term salinization.

2.6.4.2 The storm: a saltwater event

From July 2015 to October 2016, CHERT experiments had conveyed that the most conductive anomaly was concentrated below the silt layer, but another strong conductive body appeared between nest N3 and borehole PP20 early in 2017.

The traditional SWI paradigm (Abarca et al., 2007; Henry, 1964) suggests that it is the freshwater head what drives the seawater-freshwater interface movement. When heads rise, the interface moves down and seawards because freshwater pushes saltwater seaward. When the groundwater table falls, the opposite occurs, and the seawater interface moves up and inland. The work by Michael et al. (2005) explains how other mechanisms, besides seasonal exchanges, can promote seawater circulation enhancing the seawater intrusion and mixing. According to Michael et al. (2005), some of these mechanisms are: tides, wave run-up on the beach, and dispersion of saline water into freshwater discharge. In the Mediterranean Sea, tidal forcing is not a cause of important change in heads because the tidal amplitude is small (< 20 cm). Wave action and wind could drive changes in the sea level and thus in groundwater heads, but these effects are not long lasting.

A recent study by Huizer et al. (2017) about monitoring salinity changes in response to tides and storms in coastal aquifers showed, through surface ERT experiments, as well as flow and transport simulations, that storm surges can have a strong impact on groundwater salinity. In time-lapse images of the Argentona site, storms seem to be enhancing the conditions for seawater to move inland, through the most superficial layers (Figure 2.9a); and further infiltrate the soil from the surface through piezometer PP15, which is fully screened, and between nests N1 and N3. However, salinity increases from the top, rather than from an interface. Therefore, we conclude that these changes in salinity are

the result of storm surges, rather than from interface dynamics. In fact, six months later (Figure 2.9c), the unconfined aquifer has recovered, which implies a more dynamic system in the superficial layers.

The CHERT experiment seems to constitute a good tool for the monitoring of such phenomenon near the coast related to tides, wave run-up, and submarine groundwater discharge.

2.6.5 Model validation

Differences between bulk EC models obtained from induction logs and CHERT are attributed to the differences in location and in time of acquisition, considering they were performed neither at the same time nor at the exact same location.

The comparison of the bulk EC model with other independent data sources was very important to prove the reliability of the CHERT experiment. The use of other types of data such as induction logs and water EC from water samples have helped in increasing the confidence in the capabilities of the CHERT experiment for monitoring coastal aquifer dynamics. Water samples are taken only from screened piezometers or with the use of sophisticated isolating equipment. With water samples we can observe the increase in water EC in time and in space, but we can't know the depth of the interface or the lateral variations between wells. Induction logs reproduce similar data than the CHERT experiment, but only along piezometers. Interpolation techniques must be applied to IL data to obtain a 2D image. The CHERT experiment involves real interaction between boreholes. Furthermore, although sensitivity is concentrated around the electrodes (Figure 2.4), we would like to stress that ERT (surface- or borehole-based) have sensitivity to the electrical conductivity outside of the array (so-called outer-space sensitivities) as studied by Maurer and Friedel (2006).

2.6.6 The CHERT experiment

The CHERT experiment, contrary to surface ERT, is an invasive procedure because it needs the installation of boreholes, which may affect local dynamics. For example, the vertical anomalies along piezometer PP15, better observed in Figure 2.8a and Figure 2.9a, are attributed to fluid flow through the annular space between the borehole and the formation. Borehole measurements are, nonetheless, necessary for subsurface exploration. We suggest an additional consideration when planning the position of the boreholes to use CHERT.

A key point to consider when defining a CHERT experiment is the aspect ratio between the horizontal distance of the boreholes and the maximum vertical distance between the electrodes located in each borehole (e.g., LaBrecque et al. (1996)). Ideally, we would look for small values of the aspect ratio, but the location of the boreholes was conditioned by several factors including logistics and requirements for other monitoring methods as well as experiments planned at the experimental site. Furthermore, there is a trade-off with the overall investigation area implying that larger borehole spacings are sometimes motivated. Beyond this, both the geology (Figure 2.1c and Figure 2.4) and the SWI display significant lateral continuity so that vertical resolution is more critical than the horizontal one. This is achieved by imposing stronger regularization constraints in the horizontal than in the vertical direction.

The use of an optimized protocol to acquire a complete dataset in the least amount of time is recommended to capture dynamic processes with changes happening in a smaller time-step. This was not the objective of the CHERT monitoring experiment in Argentona from 2015 to 2017, but it is feasible (taking into consideration that metal corrosion will be accelerated by the injection of electric current, implying that the life of the instrument will be certainly shorter). Although surface ERT does not have enough resolution for the depth of interest, the combination of CHERT with surface ERT is suggested to understand the most superficial layers of the subsurface.

Future work will include hydrological modeling of density-dependent flow and transport at the Argentona site in order to reproduce the observed bulk electrical conductivity changes observed with the CHERT experiment. It is anticipated that this model can be used to predict future changes in the system.

2.7 Conclusions

The monitoring experiment using CHERT at the Argentona site, from July 2015 to September 2017, was successful in several aspects, regarding both geophysical imaging and SWI understanding:

- The joint use of CHERT and surface ERT increased the initial model resolution compared with only surface ERT. Comparison of CHERT inversion to salinity profiles from induction logs is excellent and validates the methodology.
- The increase in resolution allowed us to image unexpected salinity changes both in the upper layers, and the lower layers with only limited loss of resolution with depth despite the high salinity of water.
- Imaging of spatially fluctuating salinity has led to explaining the paradoxical salinity profiles often recorded in fully screened wells (step-wise increase but without reaching seawater salinity) as due to deep freshwater flowing up inside the well and mixing.
- Time-lapse CHERT captured long-term and short-term conductivity changes. Long-term changes included (a) seasonal fluctuations of groundwater flux that cause the seawater-freshwater interface to move seawards during periods of high flux or landwards during periods of low flux; and (b) the long-term salinization of the lower aquifer due to an intense drought in the study area during the monitoring period. Short-term changes included (a) a decrease in conductivity related to a heavy individual rain event of 220 mm of precipitation (a third of the annual average rainfall) in only one day; and (b) an increase in conductivity in the beach area, coinciding with storms that caused enhanced wave activity.

In short, employing CHERT at the Argentona site proved to be a cost-effective and efficient tool to shed light on seawater intrusion dynamics through the analysis of bulk formation conductivity.

3 Hydrogeophysical inversion of heads, solute tracer and geoelectrical data for seawater intrusion characterization: The Argentona case.

3.1 Introduction

Coastal aquifers are under stress due to population growth and the consequent economic needs which increase the demand for groundwater. They also suffer the effects of climate change such as heavier rains and storms, longer periods of droughts and sea level rise. This situation has been recognized as critical for freshwater resources in all coastal areas where subsurface aquifers constitute the main drinking water source. Seawater intrusion (SWI) is one of the threats chasing coastal aquifers. Coastal aquifers differ from other aquifers in that their depletion causes the advance of seawater within the aquifers, greatly affecting water salinity (Michael et al., 2017). For this reason, monitoring salinity in these regions is of extreme importance.

Traditional point measurements have the disadvantage of very low spatial coverage, making it hard to map the total extent of SWI, but also have high uncertainties due to the variable density system. Using heads and concentration data in these regions is not straight-forward. Head measurements requite measuring salinity along the whole profile. Costall et al. (2020) describe the difference in measured heads depending on the position of the screen: the freshwater zone, the seawater zone or the transition zone. Also, they state that in screened wells, the point-water head assumes that the measured head exists throughout the whole column, but water redistribution inside the well can occur, especially if the screen crosses layers with different hydraulic conductivities. Post et al. (2007) reminds the “golden rules” for taking and using hydraulic head measurements in variable-density systems, stating that not following these rules in the field may lead to very high uncertainties in the computation of hydraulic gradients, and to an uncertain determination of hydraulic conductivities for the groundwater models. Salinity measurements are affected by mixing in the wells. Carrera et al. (2010) state that water salinity measurements in fully open wells may reflect a flux-averaged concentration instead of the resident aquifer concentration. Shalev et al. (2009) alerts about the “short-circuit” that can be created in piezometers with long screens, allowing a vertical flow between higher and lower hydraulic conductivity zones and compromising the measurements of hydraulic head and water salinities.

The use of geophysical methods is attractive because they are non- or minimally intrusive and provide a large spatial coverage, unlike traditional hydrological methods. Using geophysical data to constrain hydrological models is the core of the scientific branch called hydrogeophysics (Binley et al., 2015) and it has increased in popularity since the 1990S, with many successful field examples (Daily et al., 1992; Irving and Singha, 2010; Jardani et al., 2012; Kowalsky et al., 2005; Looms et al., 2008; Scholer et al., 2011; Singha and Gorelick, 2005). Nevertheless, hydrological variables and geophysical

variables are not always highly correlated (Binley et al., 2005; Blainey et al., 2007; Gehman et al., 2009). The SWI context sounds ideal for hydrogeophysical applications because the bulk electrical conductivity (ECb) measured with electrical and electromagnetic methods is directly proportional to water salinity. The spatial coverage of electric and electromagnetic methods has made possible the study of SWI at a large scale (Goebel et al., 2019).

Calibrating SWI models is hard due to conceptual and computational difficulties (Carrera et al., 2010). Carrera et al. (2010) list some of these difficulties as reasons why there are so few examples of automatic calibration of SWI models (Beaujean et al., 2014; Comte and Banton, 2007; Coulon et al., 2021; Herckenrath et al., 2013a; Iribar et al., 1997; Sanz and Voss, 2006; Shoemaker, 2004). They mention the three-dimensional character of the SWI problem and its sensitivity to subsurface heterogeneities; the sensitivity to bathymetry and topography (Abarca et al., 2007; Yu et al., 2016); the uncertainty related to heads and water salinity measurements in variable-density systems; and, the computational effort required for solving two coupled non-linear equations, in 3D and inside an inverse problem. In the field of hydrogeophysics, Beaujean et al. (2014), Nguyen et al. (2009) and Huizer et al., (2017) have tried to combine hydrological and geophysical datasets using the sequential hydrogeophysical inversion (SHI), where a geophysical inversion is performed using only geophysical data, and bulk electrical conductivities are transformed to water salinities to constrain or validate hydrological models. This approach has several drawbacks, the biggest one being that errors from the geophysical inversion process are propagated into the hydrological model (Ferré et al., 2009; Hinnell et al., 2010).

Coupled hydrogeophysical inversion (CHI) is another approach consisting in linking hydrological and geophysical models to make the hydrological processes drive the interpretation of geophysical data. Few have tried this in the SWI context (González-Quirós and Comte, 2020; Herckenrath et al., 2013b, 2013a; Lebbe, 1999; Steklova and Haber, 2017a). Recently, Coulon et al. (2021) have done the CHI using hydraulic heads, electromagnetic and ERT data, and they concluded that the use of geophysical datasets greatly improved the results of the inversion. They used the sharp interface SWI model but, while tempting due its very fast computation times, the simplicity of these models may not be adequate in many cases (e.g. aquifers with a broad transition zone and salinity inversions (freshwater below saltwater)). A density-dependent flow and transport model is needed to describe complex SWI features and mixing zones.

The Argentona site is a Mediterranean alluvial aquifer 40 km northeast of Barcelona, Spain. A series of experiments have been carried out in the site from 2015 to 2017, to study the dynamics of SWI and submarine groundwater discharge (SGD). The experiments include monitoring with distributed temperature sensing, geoelectrical surveys and geophysical borehole logging, heads and solute concentrations measurements, among others (Folch et al., 2020; Goyetche, 2021; Martínez-Pérez et al., 2019; Palacios et al., 2020; del Val et al., 2021). Specifically, a 2-years time-lapse monitoring experiment using cross-hole electrical resistivity tomography (CHERT), discussed in Chapter 2 yielded high resolution formation electrical resistivity images and it was useful for improving the site's conceptual model and for understanding transient processes (Palacios et al., 2020). The usefulness and quality of the data make us conjecture that this dataset can substantially help in the model calibration process through a coupled inversion of hydrological and geophysical state variables, namely heads, salt concentrations and bulk electrical resistivities.

The objective in this chapter is to assess the gains of performing a coupled hydrogeophysical inversion on a seawater intrusion problem using high resolution time-lapse CHERT, while accounting for heads and salinity measurement issues.

3.2 Experimental site

The Argentona experimental site is located on the Mediterranean coast of Spain, 40 km NE Barcelona, at the end of the Argentona ephemeral stream watershed (Figure 3.1a). A typical Mediterranean stream, it is generally dry but carries a large flow rate when it rains. In fact, summers are especially dry and there could be months without any significant precipitation. Heavy rain events occur in the fall. They represent a large portion of the annual precipitation (around 600 mm). Except during these events, the stream is dry.

In order to study groundwater discharge to the sea and follow SWI, 16 boreholes have been installed in a cross-shaped distribution at the mouth of the Argentona ephemeral stream (Figure 3.1b). In this study we will focus on the central line, a transect perpendicular to the coastline, due to the low coverage along the direction parallel to the coast. The considered transect includes 3 borehole nests (N2, N3 and N1), two fully-screened boreholes (PP15 and PP20) and one single borehole (PP18). Nests are a group of 3 boreholes with a 2 m screened interval at roughly 15 m, 20 m and 25 m depth.

The geology of the aquifer represents a typical fluvial sediments alternation of sand, gravel and silt sequences overlying weathered granite (see details of the geological characterization in Martínez-Pérez et al., (2019)) (Figure 3.1c) .

The Argentona site is a highly instrumented site where a series of experiments have been carried out since its construction. Surface and cross-hole electrical resistivity tomography (Palacios et al., 2020), distributed temperature sensing (del Val et al., 2021), geological characterization through core descriptions and borehole logs (Martínez-Pérez et al., 2019), geophysical logs such as induction logs, magnetic logs and nuclear magnetic resonance, pumping tests, heads, which have allowed us to perform a thorough analysis of tides (Goyetche, 2021), and solutes concentration monitoring through water sampling. A description of the site instrumentation can be found in Folch et al. (2020).

In this study, we focus on using head data, solute concentration data and cross-hole electrical resistivity tomography to move from the qualitative interpretation of the Argentona site hydrological processes made in Palacios et al. (2020) to a quantitative interpretation.

Head time-series have been recorded in all piezometers since 2015 using Conductivity-Temperature-Depth (CTD) sensors. The CTDs are located at the depth of the screened interval of each piezometer, and at an elevation of -5.8, -7.2 and -12 m a.s.l. for piezometers PP15 and PP20 upper and lower sections. In Argentona we have two methods for measuring water salinity. The first one are the CTDs which record water electrical conductivity (ECw) at aquifer temperature, internally corrected to ECw at 25ºC. The second one is the water sampling campaigns during which water is pumped from all the boreholes, and water salinity is measured at a reference temperature of 25ºC using a parametric probe. The water samples are scarce in time, so salinity time series were constructed using both datasets when good correspondence between the two was found.

Cross-hole electrical resistivity tomography experiment consisted in 16 acquisitions from July 2015 to September 2017. Each acquisition was composed of five panels to create the complete CHERT of the transect perpendicular to the coastline: PP20-PP15, PP15-N325, N325-N125 and N125-N225. Each panel is composed of a series of apparent resistivity measurements between the two boreholes using all electrodes. More details on the experimental setup can be found in Palacios et al. (2020).

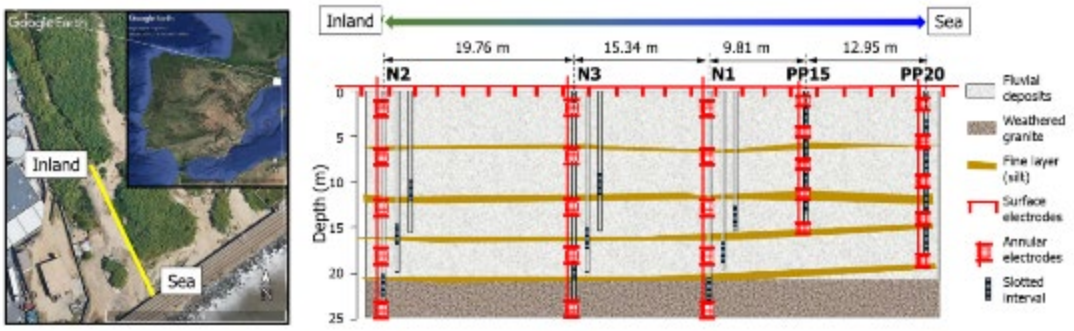

Figure 3.1. a) Localization of the Argentona site, 40 km northeast of Barcelona, in Spain, and map view of the Argentona site with the monitoring line perpendicular to the coast (in yellow). c) The stratigraphic correlation shows the lithology identified in the piezometers, based on geophysical boreholes and core descriptions. The aquifers are composed of alluvial sediments, and the base of the aquifers is composed of weathered granite. Thin clay and silt layers separate the subsurface in three sequences. Along the monitoring line there are three nests (N2, N3 and N1) with three piezometers each, with screens at 15, 20 and 25 m depth, and three individual piezometers (PP15, PP18 and PP20). PP15 and PP20 are fully screened. The piezometers are equipped with annular electrodes.

3.3 Methodology

3.3.1 Conceptual Model

The initial geological exploration of the Argentona site led to a conceptual model consisting of two aquifers separated by a silt layer at some -9 m a.s.l. However, once we did the time-lapse CHERT experiment we observed several SWI wedges: an upper seawater wedge above -5 m a.s.l and a lower one below the silt layer at –9 m a.s.l with its base at -17 m a.s.l, elevation at which we measured a further inversion in the formation EC, from conductive to resistive. This change in the EC was linked to a decrease in water salinity observed in piezometer N125, and to a decrease in bulk EC which can be associated with a change from alluvial sediments to weathered granite. For fresher water to be flow below these seawater wedges, some low permeability barriers had to be present at elevations of -5 and -17 m a.s.l.

This information was contrasted with the centimeter-scale core description made at the Argentona site and it was found that clay and silt layers as thin as a few centimeters were present at these depths in several piezometers which was confirmed by natural gamma logs. The role of very thin silt layers in controlling the flow and the salt distribution in a 100-meter scale site was discussed in a work by Pauw et al. (2017) and Martínez Pérez (2020). This re-analysis suggests a conceptual model with eight units: an unconfined sandy layer, three aquifers, three aquitards and a weathered granite layer whose low permeability nature is inferred but still unknown.

Dynamics of the site are controlled by the following processes:

- Rainfall fluctuations at several time-scales. Heavy daily rainfalls cause the Argentona ephemeral stream to discharge in a flash-flood manner, and lead to recharge events which are highly concentrated in time. Seasonal fluctuations cause the advance and retreat of the seawater wedge and are reflected in head responses, water salinity measurements and time-lapse CHERT. Interannual droughts also affect the study site. The one from 2015 to 2017 caused an overall salinization of the study area in the two years of monitoring.

- Storm surges affect the beach area, from the coastline until approximately piezometer PP15. Surges were observed at the site (storms with waves bringing SW to the site) and detected with the time-lapse CHERT experiment in response to severe storms. The bulk EC images showed the saltwater infiltration from the top of the soil until the first low permeability layer.

- The water table at the site is found at roughly 3-meters depth.
- Agricultural, commercial and industrial use of the surroundings control groundwater flow from the nearest mountains towards the sea. This water flow was monitored through a piezometer located 400 m away from the site, where we measured the diminishing trend of the water table in the two years of monitoring, which further supports salinization of the site.
- Small-scale head fluctuations are related to sea level fluctuations.
- Fresh groundwater flows through the deepest layer of the study area and below the seawater wedge, as has been evidenced by water samples from piezometer N125 and from bulk EC measurements.

3.3.2 Density-dependent flow and transport Model

The Argentona alluvial aquifer is simulated by a two-dimensional model. Spatial discretization is shown in Figure 3.2. Delayed yield is simulated by assigning a high storage coefficient in the first layer of the model covering all the area above 0 m a.s.l. The top boundary from the coastline (x=0 m) to the right boundary, and the vertical right boundary, represent the seawater level boundary with a salinity (T2S) of 38 g/L. Freshwater flow from the inland regional system towards the sea enters the model through the left boundary, from 0 m a.s.l until -45 m a.s.l, with a salt concentration of 0.22 g/L. Precipitation is represented in the model as a prescribed flow boundary condition directly at z = 0 m a.s.l to avoid the delay of the first layer. The effect of storm surges is modelled as a surface recharge over the area from the top of the model until -5 m a.s.l and from the coastline until piezometer PP15 with a salt concentration of 30 g/L. The base of the model is considered as a no-flow boundary.

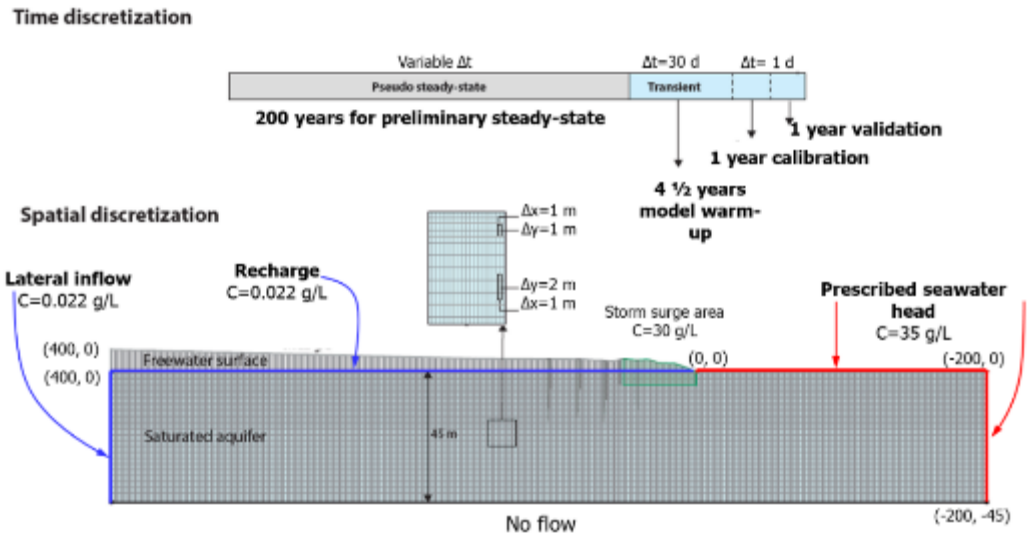

Figure 3.2. Temporal and spatial discretization of the Argentona site hydrological model. The timeline shows 4 periods: first, a 200-years pseudo steady-state; then, a 4 and ½ warm-up period during which varying boundary conditions with time-series start; finally, the actual experiment is simulated at the site during two years with a daily time-step. The first year of the monitoring is used for model calibration, and the second year is used for model validation. The mesh covers a total of 600 m, with 200 m at the seaside, and 45 m in depth. The site topography reaches a maximum of 7.3 m on the left side. The cells of the mesh vary from 2x1 m to 1x1 m (from bottom to top). Boundary conditions for flow and solute transport are represented in the figure with colored lines.

The time discretization includes four periods: first, a 200-years pseudo steady-state period during which the model is filled with seawater entering through the seawater boundaries; then, a 4 and ½ warm-up period during which time-varying boundary conditions are applied with a monthly time-step; finally, the actual experiment from mid-May 2015 until September 2017 is simulated with a daily time-step. This last simulation period was divided into two: a first one-year period, from mid-May 2015 until July 2016 is used for the calibration of the model, and a second one-year period, from July 2016 until September 2017, is used for the validation of the model.

Time-varying boundary conditions are shown in Figure 3.3. Time-series were applied from 2011 averaged over a time-step of 30 days, and then from 2015 with a time-step of 1 day. The freshwater top recharge (Figure 3.3a) was computed using a soil-water balance program which uses precipitation and temperature data to estimate potential evapotranspiration and real evapotranspiration. The program computes the effective precipitation and, by subtracting the surface runoff, can yield the amount of water that actually infiltrates the subsurface. Recharge occurs when water content exceeds the field capacity. We can observe that precipitation is low in the years of the monitoring, due to a drought period. Figure 3.3b shows the lateral inflow from the inland side, which was estimated by fitting a water balance in a box model to the hydraulic heads from a piezometer located 400 m inland. The estimated freshwater top recharge from the soil-water balance is what enters the box, and the outflow from the box is what enters the Argentona site model. The head data from the uphill piezometers shows a descending trend from 2011 to 2017, and this is translated into the boundary condition. For the sea-side boundary, the daily time-series from "Puertos del Estado" website was used, specifically the data from Barcelona Port located 4 km from the Argentona site (Figure 3.3c). For simulating the storm surges, we chose the days with a minimum of 2 m of simulated wave height data (Figure 3.3d).

Two conceptual models were calibrated (Figure 3.4) using the displayed a priori values for the parameters of the flow and transport simulator. The 1A model represents the first conceptual model of the Argentona site, with a confining layer dividing the aquifer into two. The 3A model is the updated model of the site, where two additional layers of silt and clay were added. In the figure we have also added the hydrological model observation points. Depending on the depth of the screened interval and of the surrounding predominant lithology, the observation point is considered for the heads or for the salt concentration simulated data.

3.3.3 Petrophysics and Geoelectrical modelling

The density-dependent flow and transport simulation yields a salinity distribution. This is translated to ECw using a linear relation (Sen and Goode, 1992). Then, we convert water EC into formation or bulk EC. For this purpose, we use a petrophysical law. The geological description of the cores recovered from the Argentona site piezometers show a variable clay and silt content. Even in a saline environment, the presence of clay minerals can have an important contribution to the overall bulk EC in the freshwater zone and in the transition zone. After reviewing the data from the Argentona site and the existing petrophysical models, we decided to use a generalized petrophysical law by Linde et al. (2006):

$$\sigma_{eff} = \frac{1}{F}[S_w^n \sigma_w + (F-1)\sigma_s] \tag{3.1}$$

Where σ_{eff}, σ_w, and σ_s are the bulk, water and clay surface conductivities, respectively, F is the formation factor defined as $F = \theta^{-m}$, with θ the porosity and m the cementation factor. We consider a mean porosity of 0.2 for the Argentona site (Martínez Pérez, 2020; del Val et al., 2021), and m vary ranging between 1.3 and 1.8, that gives formation factors of 8 for the alluvial sediments and 18 for the weathered granite. The sediments of the first layer are unconsolidated and very porous, so we consider a formation factor of 2.5 (θ =0.5 and m =1.5).

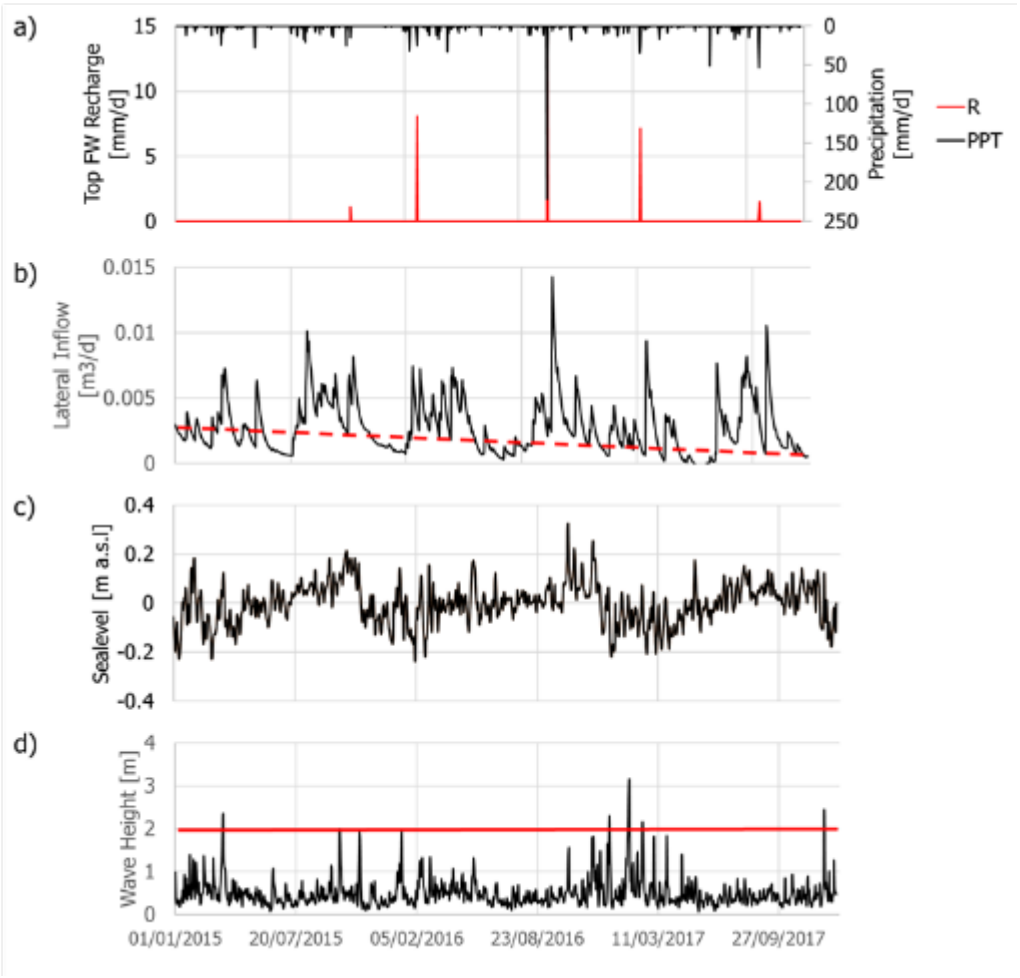

Figure 3.3. Boundary conditions applied to the boundaries of the hydrological model. a) Precipitation in the study area during the monitoring period (black). Top freshwater (FW) recharge, as computed by the soil water balance (red). A few precipitation episodes represent the effective FW recharge. b) Lateral inflow from the inland boundary is the result of the simulation using the box model and the head variations measured in a borehole 400 m uphill. The red dashed line illustrates that the inflow of FW diminishes during the monitoring period, from 2015 until 2017. c) Sea level variations, as registered in the Barcelona port. d) Wave-height simulated data from SIMMAR. The red line indicates the threshold of >2 m chosen for the application of the storm surge boundary condition.

For σ_s, we use a value of 5E-4 S/m for aquifers 1 and 2 where sand and gravel are interbedded with silt, and 0 S/m for Aquifer 3, composed of clean coarse sands. For aquitard layers and the weathered granite, which have mainly silt and clays, we set σ_s equal to 5E-2 S/m.

The CHERT electrodes are placed 50 cm to 70 cm below the ground surface, depending on the well, and the water table is around 2 m below the first electrode. Water saturation is so determinant on soil EC that we solve the petrophysical law with a water saturation of 0.3 for the layer above 0 m a.s.l to obtain the bulk electrical resistivity contrast between saturated and unsaturated soil measured in reality with the electrodes placed near the surface.

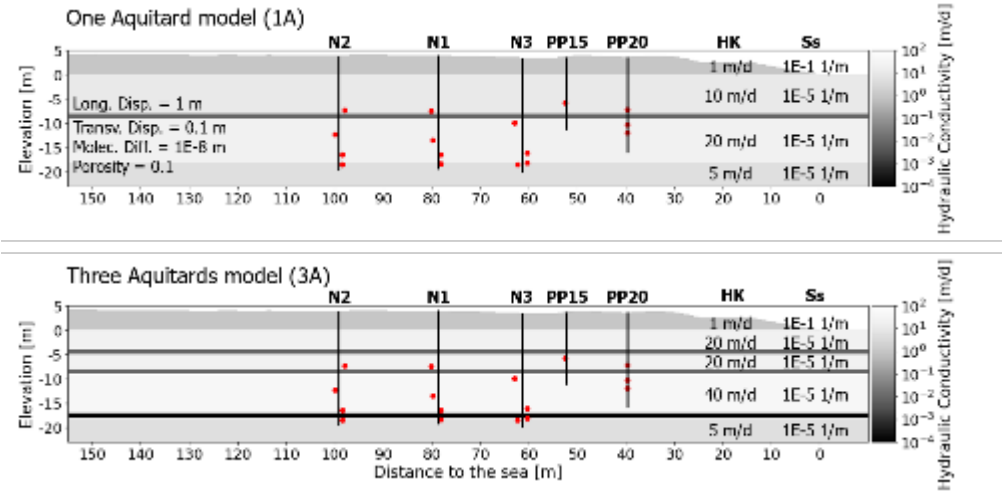

Figure 3.4. Model 1A (top) represents what was initially believed for the Argentona site layering: one continuous silt layer separates the aquifer into two. The dots represent the observation points for the readings of the simulated data during the calibration process. Model 3A (bottom) is the update of the conceptual model after the results from the CHERT experiment were interpreted along with other experimental data. Two very thin aquitard layers at -5 m a.s.l and -17 m a.s.l were found to be important for the hydraulic behavior of the aquifer and the water salinity distribution. The dots represent the observation points for the readings of the simulated data during the calibration process.

For ERT modelling the mesh must be fine near the electrodes and the mesh boundaries should be far from the electrodes to avoid numerical errors. At the same time, we have to maintain a reasonable number of elements in the mesh to limit the computation time. The mesh used to simulate the CHERT experiment is the same mesh used in Chapter 2. For coupling both simulators we used interpolation functions between meshes. For the background bulk conductivity of the mesh (everything outside the Argentona site area), we've used the mean ECb measured in the surveys, approximately 0.05 S/m.

In the geoelectrical simulation, there is current injection through a pair of electrodes and a reading of potential in another pair of electrodes. Using Ohm's law,

$$R = \frac{V}{I} \tag{3.2}$$

Where R is the electrical resistance, V is the potential and I is the current, we can relate the difference of potentials with the subsurface resistance R. Then, taking into account the geometry of the acquisition through the geometric factor K, we obtain the apparent electrical resistivity:

$$\rho_{app} = \frac{K}{VI} \tag{3.3}$$

The apparent electrical resistivity would be the real electrical resistivity if the subsurface was completely homogeneous. As it is not, we call the experimental data "apparent" until it is inverted and an image of the subsurface is obtained. As we're not using the results from the inverted geophysical images as in the SHI due to the error propagation issues mentioned by Ferré et al. (2009), we will use ρ_{app} to make the fit of the CHERT dataset.

3.3.4 Handling head and concentration data

Inversion involves minimizing an objective function that penalizes model departures from measurements by means of terms like

$$J_x = \boldsymbol{\varepsilon}_x^t \, \mathbf{V}_x^{-1} \boldsymbol{\varepsilon}_x \tag{3.4}$$

Where x stands for the type of data (i.e., heads, concentrations, or aparent resistivities, in our case), $\boldsymbol{\varepsilon}_x = \mathbf{x}(\mathbf{p}) - \mathbf{x}^*$ is the array of errors, $\mathbf{x}^*$ is the array of measurements, $\mathbf{x}(\mathbf{p})$ is the array of model responses with parameters $\mathbf{p}$, and $\mathbf{V}_\mathrm{x}$ is ideally the covariance matrix of errors $\boldsymbol{\varepsilon}_x$. In practice, $\mathbf{V}_\mathrm{x}$ is unknown, and is usually taken as diagonal because of computational simplicity and because it is natural to assume that measurement errors are independent. In reality, they need not. As mentioned in the introduction, measuring (equivalent freshwater) heads in coastal aquifers is tricky. Furthermore, errors $\boldsymbol{\varepsilon}_x$ include not only measurement errors, but also model errors. The latter result from model simplifications on heterogeneity, model dimension, or boundary conditions, to name a few.

Addressing autocorrelation can introduce an additional degree of complexity. An intermediate option is to adopt a first order autoregressive model (AR(1)) for time autocorrelation of heads, which was used successfully by Carrera and Neuman (1986) in a vertical cross section model hydraulically analogous to ours. In essence, the AR (1) involves adopting for each data time series a covariance of the form

$$\mathrm{corr}\left(\varepsilon_i, \varepsilon_j\right) = \sigma_x^2 \rho^{|i-j|} \tag{3.5}$$

where i ($1 \leq i \leq n$, number of data) and j stand for time order, σ_x^2 is the variance of ε, and ρ is the autocorrelation coefficient. The corresponding weights matrix is

$$(\mathbf{V}_x^{-1})_{ij} = \frac{\sigma_x^2}{1-\rho^2} \begin{cases} 0 & \text{if} \quad |i-j| > 1 \\ -\rho & \text{if} \quad |i-j| = 1 \\ 1+\rho^2 \ \text{ if } \ i = j \neq 1, n \quad \text{or} \quad 1 \ \text{ if } \ i = j = 1, n \end{cases} \tag{3.6}$$

Substituting this equation into (3.4) and doing some tedious but straight forwards algebra yields

$$J_x = \sigma_x^2 \left[\frac{\rho}{1-\rho^2} \sum_{i=1}^{n-1} (\varepsilon_{i+1} - \varepsilon_i)^2 + \frac{1-\rho}{1+\rho} \sum_{i=1}^{n} {\varepsilon_i}^2 + \frac{\rho({\varepsilon_1}^2 + {\varepsilon_n}^2)}{1+\rho} \right] \tag{3.7}$$

The last terms can be neglected for large n, which allows us to view J_x as the sum of squared errors of the values of x and of their time increments. Therefore, by appropriately weighting both, one can reproduce any autocorrelation. This option is similar to minimizing the sum of squared errors in the variable and its derivatives, which is used in the oil industry for pumping test interpretation (Gómez et al., 2014). To this end, the heads time-series were converted into a heads difference time-series, so $\boldsymbol{hh} = \boldsymbol{h_{t+1}} - \boldsymbol{h_t}$. Using the head differences, we constrain the model to follow the magnitudes of the head variations in time while we subtract the measurement and datum errors.

The same concept may be used for concentration data. However, here, data are much more scarce. Therefore, rather than time correlation, what we want to account for is spatial correlation, which may be induced by numerical dispersion or structural errors (e.g., on the location and or choice of silt layers). A similar concept has been explored successfully by Minutti et al. (2020) for head data. Here, we extend this concept to concentration data. Therefore, in addition to the sum of square errors in the absolute values of salinity, we also consider the sum of square errors on the spatial differences. Specifically, we sought salinity differences at different depths in the same nest. We calibrate $\boldsymbol{cc} = \boldsymbol{c_{Ni25}} - \boldsymbol{c_{Ni20}}; \boldsymbol{c_{Ni20}} - \boldsymbol{c_{Ni15}}$, with $\boldsymbol{i} = \mathbf{1}, \mathbf{2}, \mathbf{3}$, in order to force the model to keep a structural difference in the water salinity.

3.3.5 Hydrogeophysical Objective Function

A total of 16 parameters were calibrated. These included 8 log-transformed hydraulic conductivities, 4 multipliers applied to the lateral freshwater flow through the three aquifer layers and the weathered granite, a multiplier for the top freshwater recharge, a multiplier for the SW from storm surges, and the formation factors for the alluvial sediments and the weathered granite. Parameter estimation was done using the Gauss-Levenberg-Marquardt algorithm, as implemented in PEST (Doherty, 2015), to minimize the squared-weighted differences between simulated and observed values.

The objective function to minimize includes hydrological and geophysical datasets, as well as model parameters:

$$J = J_h + J_{hh} + J_c + J_{cc} + J_{rho} + J_p \tag{3.8}$$

$$= \boldsymbol{\varepsilon}_h^t \, \mathbf{V}_h^{-1} \boldsymbol{\varepsilon}_h + \boldsymbol{\varepsilon}_{hh}^t \, \mathbf{V}_{hh}^{-1} \boldsymbol{\varepsilon}_{hh} + \boldsymbol{\varepsilon}_c^t \, \mathbf{V}_c^{-1} \boldsymbol{\varepsilon}_c + \boldsymbol{\varepsilon}_{cc}^t \, \mathbf{V}_{cc}^{-1} \boldsymbol{\varepsilon}_{cc} + \boldsymbol{\varepsilon}_{rho}^t \, \mathbf{V}_{rho}^{-1} \boldsymbol{\varepsilon}_{rho} + \boldsymbol{\varepsilon}_p^t \, \mathbf{V}_p^{-1} \boldsymbol{\varepsilon}_p \tag{3.9}$$

Where J stands for objective function and the subscripts h, hh, c, cc, rho and p correspond to heads absolute values, heads time differences, concentrations absolute values, concentrations spatial differences, apparent resistivities and model parameters. We assume homogeneous and uncorrelated data errors, so that all $\boldsymbol{V}^{-1}$ matrices are diagonal matrices, with each element being the weight given to each data points. The terms in equation (3.9) are the same as in (3.4) for each data type. The term J_p is a model regularization term, corresponding to a first-order Tikhonov regularisation using preferred or a priori values for the 16 parameters. The a priori values are displayed in Figure 3.4.

As the problem is ill-posed and the parameters that we estimate present are highly correlated (lateral groundwater flow and hydraulic conductivities, for example), we use model regularisation through singular value decomposition. Singular value decomposition decomposes the set of parameters into two subspaces: a solution subspace and a null space, and solves the problem by changing the parameters from the solution subspace, while leaving those in the null space with their initial values because they cannot be properly estimated.

Three inverse problems are proposed for the calibration; they are presented in Table 3.1. Inverse problem HC uses the terms with h and c, with equal weights in the objective function. This inverse problem represents the traditional hydrological inverse problem. Inverse problem HHCC includes h, hh, c and cc, to circumvent data quality issues in coastal aquifers. The relative inter group weights reflect the data quality issues. We've ranked the datasets from highest to lowest quality in this order: hh, c, cc and h. Inverse problem HHCCR includes h, hh, c, cc and rho. In the joint hydrogeophysical inversion, we include the apparent resistivities rho. The CHERT dataset (rho) is given the highest rank in quality. This inverse problem will allow us to test our hypothesis about the improvement of the prediction capability of our model when adding geophysical data.

The prediction capability of each inverted model is tested using the validation period with the remaining dataset from July 2016 to September 2017.

Figure 3.5 displays a scheme of the numerical tool developed to perform the coupled hydrogeophysical inversion. The density-dependent flow and transport simulator (SEAWAT (Guo et al., 2008)) is linked to the CHERT simulator in PyGIMLi (Rücker et al., 2017) by means of a Python interface. Inside the Python interface, the computations are made to convert one datatype into another through the water salinity to ECw relation and through petrophysical relations; and to prepare the simulated datasets to be the input for PEST.

Inverse Problem Name	Observation Groups	Weight within ϕ
HC	Heads (h)	50%
	Salt Concentrations (c)	50%
HHCC	Heads (h)	10%
	Salt Concentrations (c)	20%
	Salt Concentration Differences (cc)	30%
	Head Differences (hh)	40%
HHCCR	Heads (h)	8%
	Salt Concentrations (c)	15%
	Salt Concentration Differences (cc)	21%
	Head Differences (hh)	28%
	Apparent bulk electrical resistivities (rho)	28%

Table 3.1. Names and composition of the three inverse problems that were solved to calibrate the Argentona site hydrogeophysical model. HC: inverse problem using heads and salt concentration data with equal weight inside the objective function. HHCC: inverse problem using heads, salt concentrations, salt concentration differences and head differences with ranked weights according to the interpreter's confidence in the datasets. HHCCR: inverse problem using heads, salt concentrations, salt concentration differences, head differences and apparent bulk electrical resistivity datasets. Apparent bulk electrical resistivities correspond to the CHERT experiment and a high confidence was put on this dataset given its quality.

3.4 Results

3.4.1 Testing the conceptual models: one aquitard or three aquitards.

Figure 3.6 displays the head fit results from the calibration of the 1A (red) and the 3A (blue) models solving inverse problem HC. The observed data are plotted in black. In the grey areas we plot the calibration data points, while in the white areas we plot the modelled heads in the validation period. That is, the points in the white area were not included in the inverse problem. The piezometers are divided in three groups following the classification made in Chapter 2: piezometers in the freshwater, transition and saltwater zones.

By looking just at the grey areas, we can notice that both models achieve a good fit of the head absolute values for all piezometers. The piezometers of the freshwater zone (N215, N315 and PP15) show that calibrated head time series from 1A have imperceptible daily variations. The modelled head in the validation period is more than 1 m too high in times of large recharge at the top of the model due to precipitation or storm surges. In the transition zone piezometers (N220, N320 and N115), there is a 25 cm difference between both models. Daily variations are well reproduced in the calibration and the validation period. In the saltwater zone (N120, N125, N225 and N325) the difference in absolute values between both models is of less than 25 cm. Daily variations are reproduced by the two models.

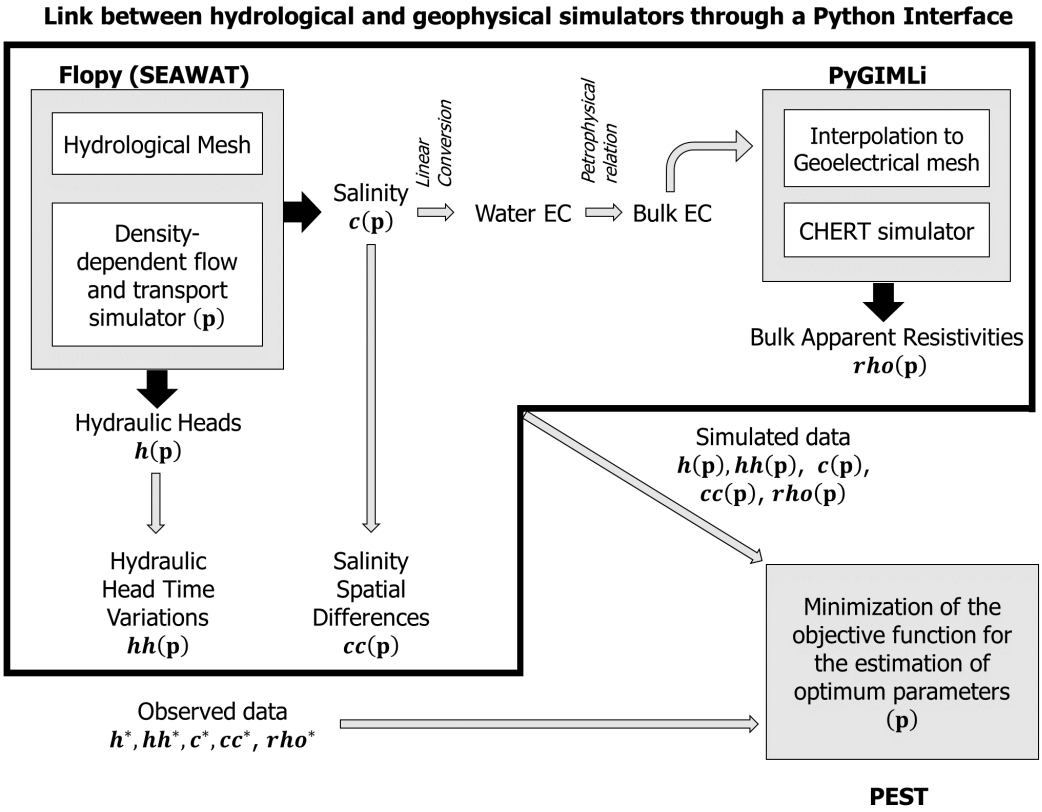

Figure 3.5. Scheme of the coupled hydrogeophysical modelling and inversion tools. The link between hydrological and geophysical simulators was done using a Python interface, which calls the density-dependent flow and transport simulator (SEAWAT) through Flopy and the cross-hole electrical resistivity tomography simulator (CHERT) through PyGIMLi. The conversions necessary to convert salinities to bulk electrical resistivity are done inside the Python interface, as well as the data conversion (from h to hh, and from c to cc). The inverse problem is solved using PEST, which collects the simulated and the observed data through its specific input files.

Figure 3.7 shows apparent resistivity records of all electrode pairs for July 2015 (top) and September 2017 (bottom). In the July 2015 CHERT (i.e., within the HC calibration period), the 1A and the 3A models display a similar fit, with the 1A model reaching higher resistivities in the N3-N2 panel. For the September 2017 CHERT, the models show a different behavior with the 3A model fitting the data better in all the panels. The 1A model is in overall more conductive, with apparent resistivities of maximum 10 Ohm.m.

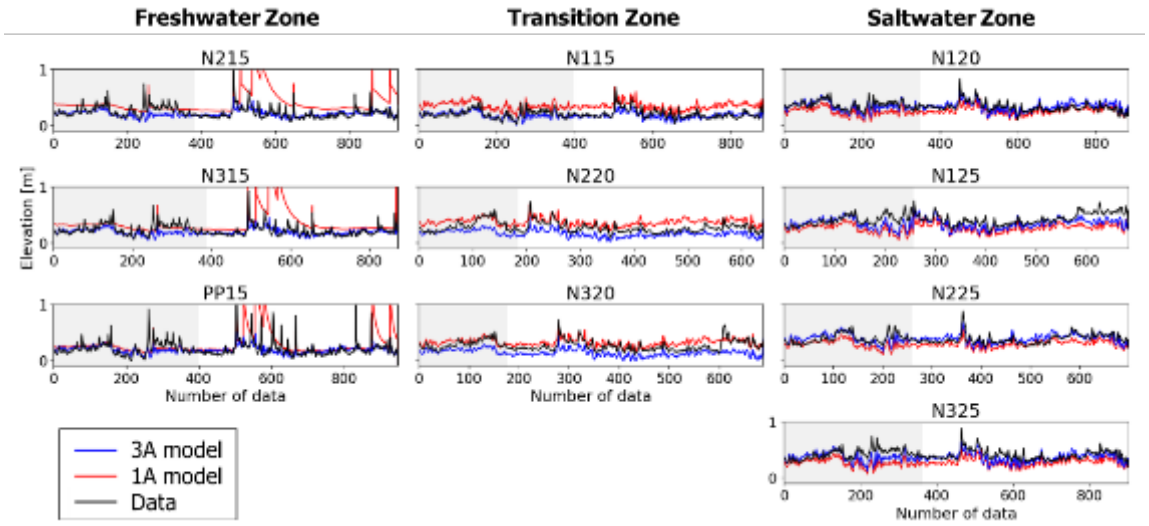

*Figure 3.6. Result of the calibration of the heads observation group using the **HC** inverse problem on the one aquitard (1A) and the three aquitard (3A) models. The grey area denotes the data points that were calibrated and the white area shows the non-calibrated data points belonging to the validation period. The three columns group the piezometers in the freshwater zone, the transition zone and the seawater zone, following the classification made in Chapter 2. The two models reach a reasonable fit in the three areas, however, the 3A model is superior in the validation test for the freshwater zone piezometers.*

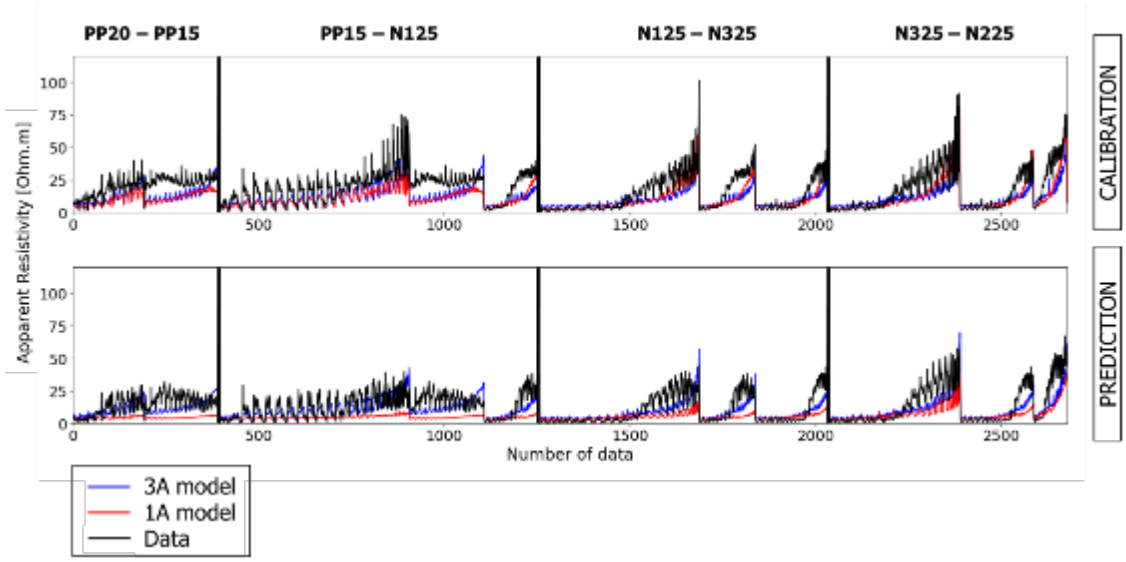

*Figure 3.7. Result of the calibration of the apparent bulk electrical resistivity (rho) observation group using the **HC** inverse problem on the one aquitard (1A) and the three aquitard (3A) models. Above, the first CHERT dataset from July 2015, belonging to the calibration period; below, the last CHERT dataset from September 2017, belonging to the validation period. Both models display a similar fit during the calibration phase, but the 3A model yields better results in the validation tests.*

3.4.2 Hydrological and hydrogeophysical inverse problems.

Table 2 presents the results of the HC, HHCC and HHCCR inverse problems solved using the 3A model. The table also shows the a priori values given to the inverse problems. The hydraulic conductivities of the water table layer vary from 3E-3 to 2.4E-1 m/d. Hydraulic conductivity of aquifer 1 varies from 3.7 to 10.5 m/d. Aquitard 1 hydraulic conductivity remains around 1E-2 m/d with estimated values from 1E-2 to 2E-2 m/d. The hydraulic conductivity of aquifer 2 has estimated values from 5.7 to 15.8 m/d. Aquitard 2 also remains around the 1E-2 m/d magnitude, with hydraulic conductivity varying from 2E-2 to 5E-2 m/d. Aquifer 3 has the largest range of hydraulic conductivity, from 7.9 to 81 m/d. Aquitard 3 moved away from the 1E-2 m/d a priori value to a hydraulic conductivity varying from 1.25E-4 to 2.33E-4 m/d. The deepest layer representing the weathered granite has an estimated hydraulic conductivity of 0.5 to 5.5 m/d.

The multipliers for lateral inflow were estimated for the three aquifers and for the deep weathered granite. The a priori values denote an increase of flow with depth. The inverse problems HC and HHCC left the multipliers almost unchanged with estimated values around 1, from 0.9 to 1.3 for the deep layer in HHCC. The HHCCR problem did use these multipliers for fitting the model, increasing from two to seven times the flow in the layers. The weathered granite layer would carry the largest amount of freshwater toward the sea according to the HHCCR inverse problem. The storm surge multiplier was diminished to a fifth in the HC problem and to a third in the HHCCR problem. It remained equal to 1 in the HHCC problem. The top recharge multiplier was increased to 1.1 and 1.2 in the HC and HHCCR problems respectively, and diminished to 0.25 in problem HHCC. Formation factors (F) were calibrated only in inverse problem HHCCR. A formation factor of 15.34 was found for the alluvial layers, much higher than the a priori value of 6. For the weathered granite, the estimated F value was 17.7, similar to the a priori value of 18.

The objective functions presented in were computed by taking the squared sum of the residuals between observed and modelled values with the parameters of the best iteration. Each data point has a weight equal to 1 in all inverse problems to compare the fit between different problems. Recall that each inverse problem has different relative weights for each observation group (Table 1).

In the calibration period, the best fit for the heads group is found in problem HC; for the heads time variations in problem HHCC; for salt concentrations in the HHCCR problem; and for spatial differences in salt concentrations in the HHCC problem.

Figure 3.8 shows the results of the modelled head time series using inverse problems HC, HHCC and HHCCR and the observed data in black. The grey and white area show the calibrated and validated data points respectively. HC and HHCCR models reach similar results in the calibration period, with a mean head absolute value similar to that of the observed data. The HHCC problem displays a mean 25 cm misfit in the modelled head data, not respecting the absolute value but respecting the head time fluctuations. In the validation period, the predominant feature are the five peaks of pressure felt by the piezometers in the freshwater and transition zones in the inverted model using HHCC. These peaks are related to the storm surge episodes (Figure 3.3). In the freshwater zone, PP15 data shows peaks that are not reproduced by any model.

Figure 3.9 displays the water salinity values. Water in model HHCC (red) is too saline in all piezometers, with a minimum of 28 g/L. Model HC has a clearer distinction of the zones, with approximately 5 g/L in the freshwater zone piezometers, 9 to 20 g/L in the transition zone piezometers and 19 to 28 g/L in the saltwater zone piezometers. Model HHCCR shows a similar result than model HC, except in the freshwater zone where salinity is around 8 g/L. Models HC and HHCCR reproduce the salinization of the transition zone. In the validation period, the models tend to keep the trend they had during the calibration period. No model was able to reproduce the detail of the salinity daily fluctuations registered with the CTDs in piezometers N125 or N225.

		HC	HHCC	HHCCR	A priori
	Parameters				
Hydraulic Conductivities	Freewater Table	3.0E-3	1.7E-2	2.4E-1	1.0E-1
	Aquifer 1	3.68	10.45	5.67	10.00
	Aquitard 1	1.0E-2	1.1E-2	2.0E-2	1.0E-2
	Aquifer 2	13.50	5.68	15.79	31.60
	Aquitard 2	2.5E-2	2.0E-2	5.0E-2	1.0E-2
	Aquifer 3	81.61	7.97	65.00	31.60
	Aquitard 3	1.3E-4	2.3E-4	1.7E-4	1.0E-2
	Weathered Granite	5.51	0.56	2.11	10.00
Fresh Groundwater Flow	Aquifer 1	0.91	1.19	2.00	1.00
	Aquifer 2	1.13	1.08	5.56	2.00
	Aquifer 3	0.91	1.13	4.44	2.00
	Weathered Granite	1.06	1.30	6.98	10.00
Multipliers	Storm Surge Flux	0.19	1.03	0.34	1.00
	Top Recharge Flux	1.39	0.25	1.28	4.00
Formation Factor	Alluvial Sediments			15.34	6.00
	Weathered Granite			17.68	18.00
	Partial Objective Functions ϕ				
Calibration Period	*h*	27.02	61.18	40.55	
	hh		3.06	3.36	
	c	3032.75	4193.50	2535.87	
	cc		1704.58	2888.37	
	rho			3.4E+6	
Validation Period (Prediction)	*h*	64.26	308.28	68.73	
	hh	10.72	248.80	9.50	
	c	18890.41	69501.49	30596.80	
	cc	4831.18	20180.34	4524.93	
	rho	2.6E+6	4.8E+6	1.5E+6	

Table 3.2. Summary of the results of the inverse problems HC, HHCC and HHCCR, along with the a priori values of the calibrated parameters and the absolute values of the total and partial objective functions. The hydraulic conductivities found by the inverse problems HC and HHCCR are similar in magnitude, while HHCC found lower hydraulic conductivities in the aquifer layers. The HHCCR supports the idea of a large freshwater flow through the aquifer layers, especially through the weathered granite. A value of 15 was found for the formation factor of the alluvial sediments, much higher than expected. For the comparison of the objective functions, all data points were given the same weight of 1.0. It can be observed that including more datasets worsens the fit of the observation groups (e.g. H, HH and CC), except in the case of the salt concentrations where the HHCCR problem reaches a better fit for group C. The misfits in the validation period (prediction) indicate that the HHCCR inverse problem is the one that yields the best results.

Figure 3.10 displays the modelled apparent resistivity of the CHERT experiment. Figure 3.9a corresponds to the calibration period, July 2015, and Figures 3.9b, c and d are from the validation period, October 2016, February 2017 and September 2017 respectively. In the calibration period, HHCC is too saline (low apparent resistivity) as was shown in Figure 3.8. HC and HHCCR show a more appropriate fit, with HC seeming slightly better in the data points with high apparent resistivity. Figure 3.9b corresponds to the CHERT 10 days after a large precipitation event. The CHERT measured overall highest resistivity this day, especially between PP20 and N1 (dispersive points in black). None of the models was able to capture this overall increase in resistivity. In Figure 3.9c and Figure 3.9d the prediction of the model HHCCR is slightly better than model HC, especially between nests N1 and N2.

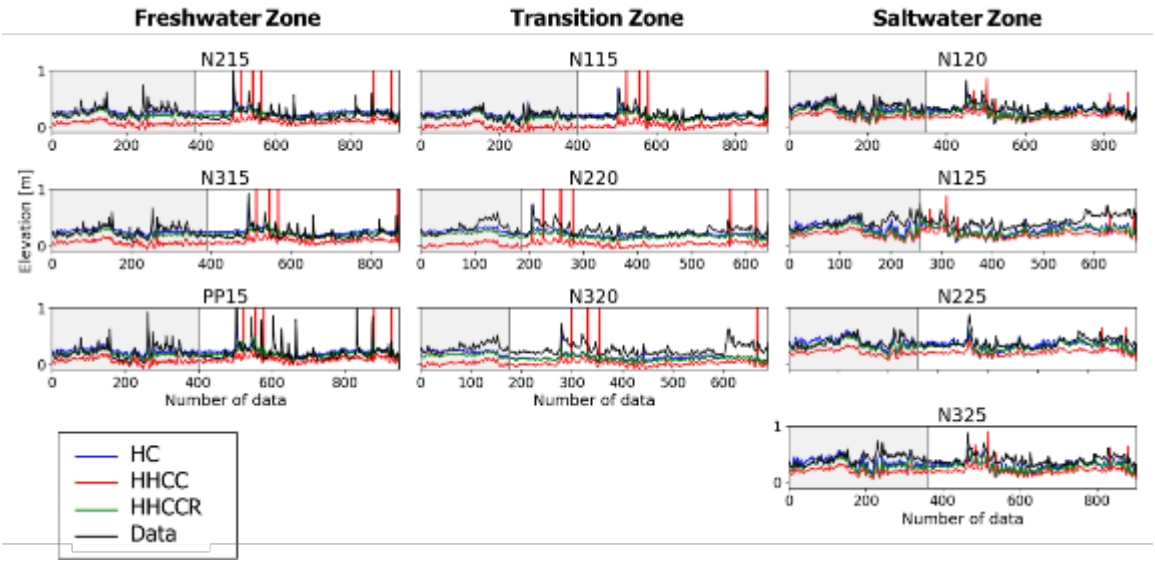

*Figure 3.8. Result of the calibration of the heads observation group using the **HC, HHCC** and **HHCCR** inverse problems on the three aquitard (3A) model. The grey area denotes the data points that were calibrated and the white area shows the non-calibrated data points belonging to the validation period. Inverse problems HC and HHCCR show a very similar result in all piezometers. The HHCC problem does not fit the absolute value of the heads, but gives more weight to the variations keeping a homogeneous gap between simulated and observed time series.*

Figure 3.11 shows four snapshots of water salinity. The color scale varies from 0 g/L in purple to 38 g/L in red. The figures show the hydrological models from the coastline to 150 m away from the coast. The four snapshots correspond to the date of the CHERT experiment in July 2015, June 2016, January 2017 and September 2017, and cover the two years of the time-lapse monitoring. The black arrows mark the height and length of the SWI in July 2015. We can see the SWI moving inland as well as getting thicker in the two years of monitoring. In July 2015, the SWI (C > 25 g/L) stopped 60 m from the sea and in September 2017 it reached 100 to 120 meters from the sea. In the vertical direction we can also distinguish a 3 m variation in the thickness of the SWI. In January 2017, storm surges salinized the upper right portion on the model until 50 m from the sea and -5 m a.s.l. The storm surge effect is largely washed out from the upper aquifer by September 2017, but the top unsaturated layer remains filled with salt water.

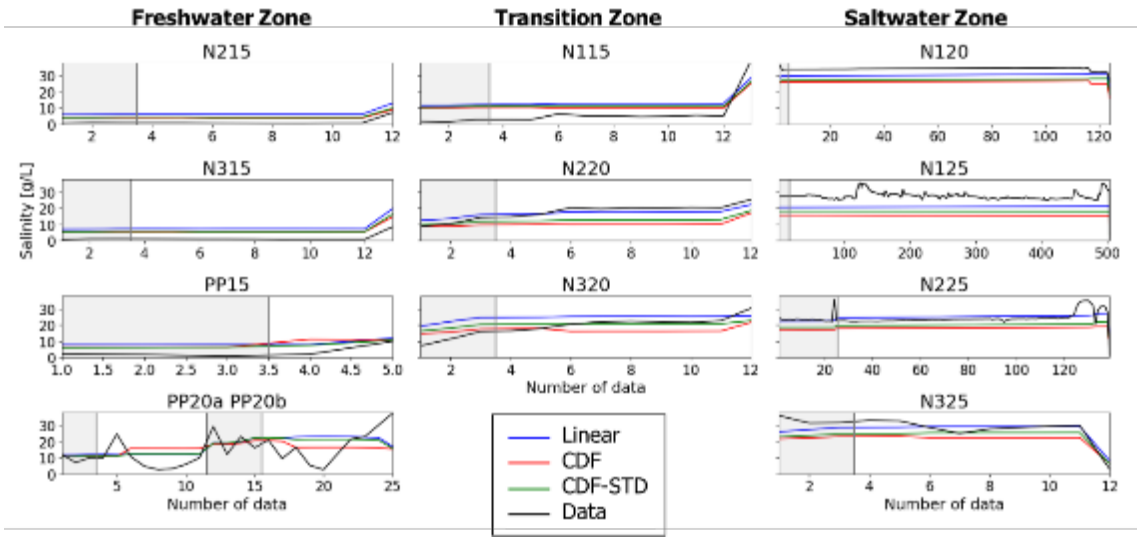

*Figure 3.9. Result of the calibration of the concentrations observation group using the **HC, HHCC** and **HHCCR** inverse problems on the three aquitard (3A) model. The grey area denotes the data points that were calibrated and the white area shows the non-calibrated data points belonging to the validation period. The HC and HHCCR inverse problems preserve the freshwater area, although the HHCCR should be fresher than 5 g/L; they are able to reproduce the salinization in the piezometers of the transition zone and to position salt water in the piezometers in the saltwater zone. The HHCC inverse problem yields a model with a very high water salinity, even in the freshwater zone.*

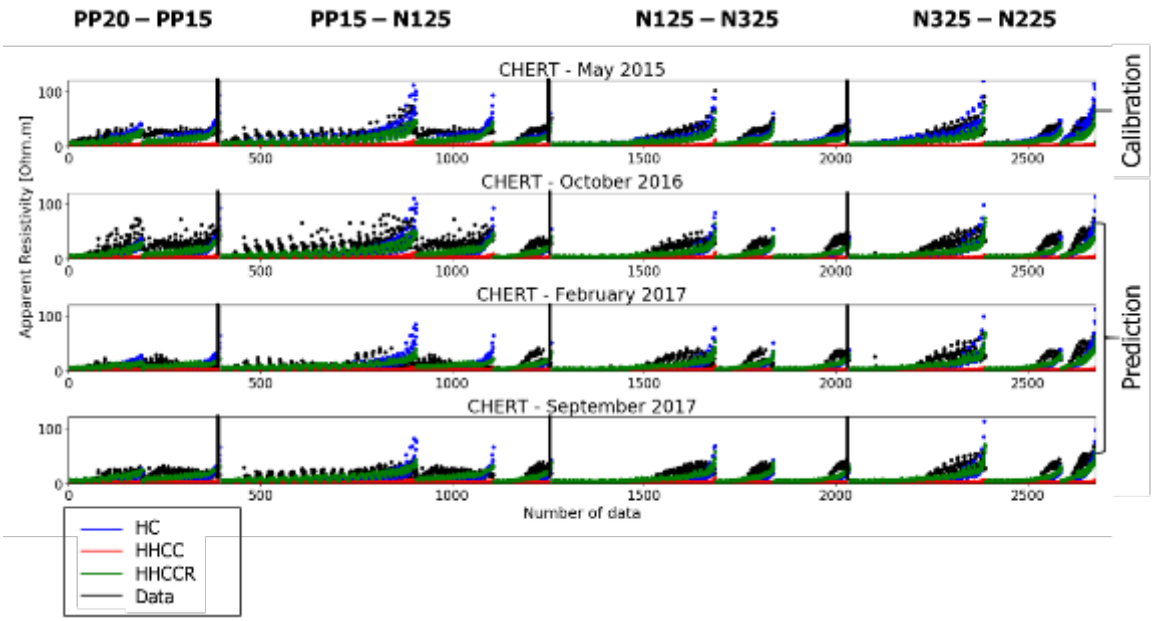

*Figure 3.10. Result of the calibration of the apparent bulk electrical resistivity (rho) using the **HC, HHCC** and **HHCCR** inverse problems on the three aquitard (3A) model. The HHCC inverse problem failed to calibrate and predict the rho time series. The HC and HHCCR problems yield a better result during the calibration phase (a), and the HHCCR makes in general a better prediction, mainly by achieving higher resistivities. In October 2016, a heavy rain event that took place a few days before the CHERT (b) caused higher resisitivity readings. This one-day phenomenon is not properly reproduced by our model, due to its time discretization, and also to the missing third dimension, important for the fresh surface and groundwater flow from the Argentona stream towards the aquifers.*

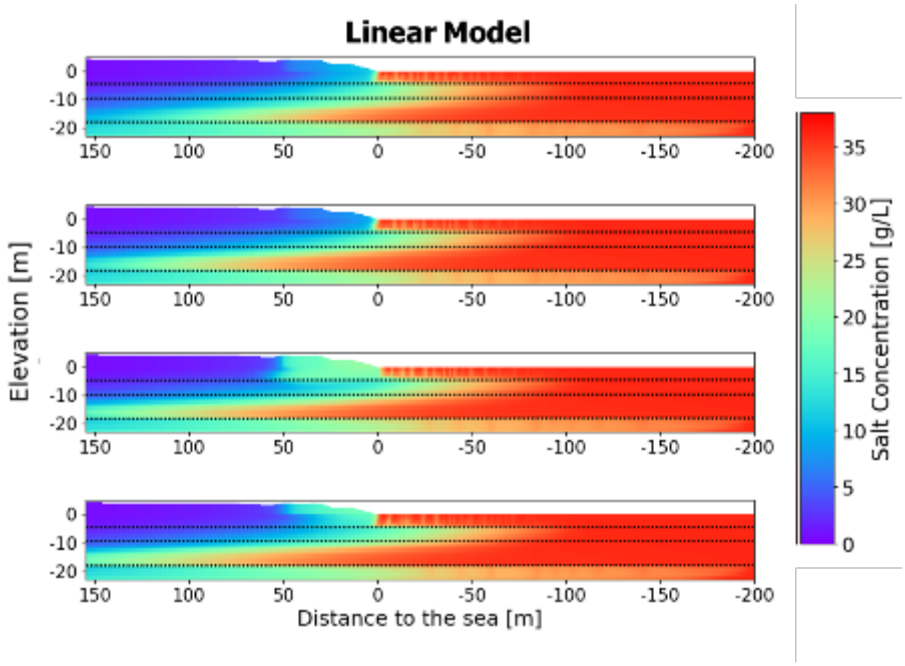

Figure 3.11. Time-lapse view of the simulated spatial distribution of salinity computed with the HHCCR calibrated model. Black lines show the position of the silt layers at -5, -9 and -17 m a.s.l, known to limit the SWI. We can highlight that the model reproduces the entrance of the SWI into the lower aquifer, from 60 m to 120 m from the coast in the two years of monitoring; the vertical movement of the transition zone, and the storm surge effect on the beach area in January and February 2017. The weathered granite layer is simulated with a salinity lower than seawater salinity, from the site until more than a hundred meter after the coastline.

3.5 Discussion

3.5.1 The role of thin aquitard layers in the hydraulic behavior.

Numerous studies have pointed out the importance of having a good conceptual model, guided by a thorough geological understanding of the study area. Costall et al. (2020), Kreyns et al. (2020), Michael et al. (2016), among many others, have proven that heterogeneities in the hydraulic conductivities can affect the hydraulic behavior of the aquifers, as well as the length to the toe of the SWI wedge and its shape. It has also been discussed that it is important to have a correct conceptual model, without structural errors, to get good results from hydrogeophysical inversion (Ferré et al., 2009; Hinnell et al., 2010). Structural errors can come from a conceptual model that is not adapted to reality. This is why we didn't want to test only one conceptual model, but to test the two conceptual models that we had at the Argentona site.

Results suggest that the 3A model as a better conceptual model for two reasons:

First, daily head fluctuations are not reproduced with the 1A model in the freshwater zone (remember that all FW piezometers are located in Aquifer 2). This might suggest a low connectivity of the aquifer with the sea, which is responsible for the small daily fluctuations. But dampening of fluctuations may also reflect that Aquifer 2 is effectively unconfined in model 1A. If Aquifer 2 were confined, hydromechanical response would cause the small sea level variations to be seen in the observation points. This is corroborated by the results of the 3A model, where an aquitard layer situated above Aquifer 2 confines the freshwater zone. This aquitard layer was also found to be important for the hydraulic behavior of the Argentona site aquifers when studying the aquifers' connectivity to the sea through the tides' signal (Goyetche, 2021).

Second, bulk apparent resistivity time series show that the 1A model is too conductive in September 2017. The CHERT time-lapse experiment showed that in 2017 the shallow depths of the Argentona aquifer were highly conductive due to storm surges and due to a drought period. However, the simulated apparent resistivity is largely below the observed value. The effect of the storm surges in Aquifer 2 is also observed in the five high peaks in the simulated head time series. This reflects that the freshwater zone piezometers are effectively open to the top layer of the model, where the saltwater from storm surges infiltrates and descends to deeper parts of the model. If a barrier is not present at -5 m a.s.l. like in the 3A model, the saltwater from storm surges is not limited to Aquifer 1.

Perhaps the most disturbing conclusion is the important role played by the thin layers at -5 and -17 m a.s.l. There two layers went unnoticed in the first geological descriptions. Yet, they control the seawater penetration into Aquifer 3 and both cause the aquifers beneath to discharge to the sea.

Note also that these two layers lead to unstable configuration with dense saltwater over light freshwater. It is well known that such confirmations lead to fingering (Abarca et al., 2007; Ben-Zur et al., 2021) But our model is not sufficiently refined to properly reproduce fingering. Some freshwater fingers can be seen carrying freshwater upwards to the sea against the infiltrating seawater. We conjecture that the mid-salinity beneath the silt layers is a “blurred” version of saline fingers dropping into the freshwater aquifer.

The 1A model with one aquitard layer guided many of our interpretations and experimental designs at the beginning of the field work in Argentona. The calibration exercise checked if a simple model such as the 1A model was enough to explain the datasets, but the results show that more refinement is needed in the model. Given the stratigraphy of the alluvial aquifers, with many intercalations of gravel, sand, clay and silt, it might be worth trying to solve the inverse problem using other parametrization approaches than the zonation approach. For example, instead of fixing the position and composition of a number of layers, we could try to solve the problem using geostatistical methods to simulate the small scale heterogeneity.

3.5.2 Data quality in coastal aquifers.

In coastal aquifers, it is difficult to use head values and salinity measurements taken from the boreholes because, very often, we don’t know for sure where or what we’re sampling, and this is inherent to the physical processes occurring in the subsurface. We can add to this difficulty, the issues related with the way the monitoring is carried out. After two years of monitoring, we had collected a great amount of data from the CTDs and, unfortunately, the data had to go through a long processing phase to recover sometimes only bits of time series. Once this processing was done and the model was built, the different sources of information for the boundary conditions (e.g. seawater level from a port away from the site, hydraulic data from piezometer uphill) and the need to georeference the model (e.g. piezometers elevation), made the head absolute values even more uncertain due to datum issues and the uncertain salinity of the water columns inside the piezometers. This is why using derived datasets that correct for this type of absolute value errors is interesting and why, a misfit in the mean absolute value of the heads is much less important for us, as interpreters, than a high misfit in the time variations. Model 1A, for example, had to be dismissed because the freshwater piezometers didn’t show enough temporal variations and this is not interesting when the transient processes occurring at the site are the ones that we wish to accurately reproduce. Although the HHCC model didn’t pass the prediction test, we can still highlight that the model fits the temporal variations better, and more importantly, that the gap between the observed and simulated head time series is more homogeneous than in the other models. When the temporal variations are not explicitly calibrated, the inverse problem fits only some of the times.

Regarding the water salinity dataset, we can start by highlighting the sparsity of the dataset that was used to calibrate the Argentona model. This was due to the difficulty of using CTDs salinity time-

series. The movement of the CTD in and out of the piezometers when other experiments take place, when they need reprogramming, or when the data is downloaded, can be another source of error. Unless extreme care is taken in measuring manually high quality salinity profiles along the borehole, the interpreter will not be able to match the time series with a given depth or salinity, even less make a conversion to freshwater heads, so needed in coastal aquifer management to interpret piezometric heads. Water samples taken from piezometers can also be tricky to use due to averaging in the salt concentration value, which may result from a mixture of waters flowing from different layers. Still, the references from hydrogeophysical calibrations for SWI studies (Beaujean et al., 2014; Nguyen et al., 2009) suggest that the use of water salinity control points are necessary in the calibration procedure.

3.5.3 Combining datasets: worse fit but better prediction

It can be noted in Table 3.2 that when we include more datasets in the inverse problem, the fit of the individual observation groups worsens. For example, the fit heads group in the HC problem is better than in the HHCC and HHCCR problems, mainly because the latter models contain more data to fit and covergence becomes more complex. The only group where the fit improves when a new dataset is added is the water salinity group in the HHCCR model, indicating that the apparent resistivity can help in fitting model salinity.

When calibrating a model, we check the reduction of an objective function because it is a way to measure the goodness of fit. However, there is a tendency in the hydrological community on looking for models that can predict rather than fit a certain dataset (Krysanova et al., 2018). A model that can predict an event is highly valuable for decision makers and for a good groundwater management. So, the "best" model is the one capable to predict the system response to future changes. Two short term transient events occurred at the Argentona site, during the validation period between July 2016 and September 2017: the heavy rain event on October 12th, 2016 (220 mm, a third of the annual precipitation) and the storm surges in January and February 2017.

Figure 3.10b shows the CHERT acquisition in October 21st, 2016, 9 days after the heavy rain event. In Chapter 2, we discussed how the CHERT data captured the decrease in bulk EC after the rain event, and this is not observed in the calibrated models. It is not necessarily linked to the inverse problem, but more to the 2D model limitations and to the temporal discretization. During such a heavy rain event, the Argentona stream carries a large amount of water and the whole Argentona site is flooded. The model used in this study does not include these features, and so it lacks fresh surface and groundwater inputs. This precipitation event represents one spike in the top freshwater boundary condition. We can also discuss how the inverse problem fits a time series through its mean absolute value and trend, because it is "cheaper" in the optimization process than fitting a one-day event. Nevertheless, through the fit of the mean and the trend models HC and HHCCR respect other characteristic processes like the two-years salinization of the transition zone and the salinity inversion in N1.

The storm surges recorded in January and February are modelled as saltwater flow on the beach area and in depth until -5 m a.s.l. The effect of these repeated surges is observed in the model because they caused a twofold increase in the bulk EC. Model HHCCR reached the best fit during the validation period, and it is the one that best simulates all types of data. Figure 3.11 shows the time evolution of the hydrogeophysical model, where we can observe that storm surges are well simulated.

3.5.4 Time-lapse monitoring simulation.

With the hydrogeophysical model calibrated using HHCCR we are able to fit the data and predict water salinity and bulk electrical resistivity variations in time and space with enough accuracy. The model reproduces the main hydrological processes that occurred at the Argentona site during the two years of monitoring: 1) the salinization linked to the drought, 2) the storm surges at the beach area,

and 3) the salinity inversion registered in nest N1 (Figure 3.11). The model also reproduces the three main salinity zones distinguished in the CHERT images: the freshwater zone (C < 10 g/L), the transition zone (ranging from 10 to38 g/L), and the deep saltwater zone (C > 25 g/L). Inside the transition zone the interface moves up and down, as well as it advances in the inland direction while salinity increases.

By comparing the time-lapse model results (Figure 3.11) with the time-lapse view of the CHERT results presented in Chapter 2 (Figure 2.6), we can observe that the true bulk EC images have more heterogeneities, and are affected by the high sensitivity around the electrodes and by the water circulation along PP15, a fully-screened piezometer. These characteristics of the true datasets are not reproduced in the model which is not contaminated by the ambient noise and not subject to the actual field conditions (e.g., flooding of the PP15 well). The CHERT experiment is a 3D experiment that averages the bulk resistivity of the medium. In the 2D model, we miss the heterogeneities of the third direction, where the Argentona stream passes surely affecting the flow in the aquifer.

3.5.5 Numerical dispersion: will we ever simulate correctly the fully fresh or fully salty water?

The freshwater zone, although identifiable in the images, does have a too large water salinity (3-10 g/L) compared to the expected water salinity (0-3 g/L). This difficulty in getting the freshwater zone salinity right was found in all tested models. During the steady state simulation, as the model fills with seawater, a convection cell forms in the bottom of the inland boundary when seawater reaches it. Werner (2017) discuss this numerical dispersion issue, stating that it is impossible to obtain salinities lower than 5 g/L in SEAWAT models. He recommends the use of a top freshwater recharge to clean the area. This was helpful but not enough to fully correct the problem.

The inability of the solute transport model to yield very low salinity affects the parameter estimation process. In our tests, we learned that PEST was trying to confine the aquifers in order to prevent saltwater to enter any aquifer layer, but this was also holding up the SWI and removed all mobility of water and transient processes with it.

When wanting to fit the apparent resistivity, the problem is translated to the petrophysical relations. Salinity is linearly correlated to water EC, so that a too high salinity reflects a too high water EC. Then, water EC is related to bulk EC through a petrophysical relation in which the formation factor F has the highest weight in the conversion when we consider no changes in lithology with time. If the water EC is too high in the model, the way to obtain a low bulk EC is increasing the formation factor F. This can be the reason why the inverse problem finds F = 15.38 in the alluvial layers, a higher value than expected. It makes us wonder if in the case of no numerical dispersion the estimation of petrophysical parameters would be significantly different.

3.6 Conclusions

The gains of performing a coupled hydrogeophysical inversion on SWI problems using high resolution time-lapse CHERT were assessed by means of prediction capability tests. Several specific conclusions can be drawn from the results:

- Regarding the conceptual model of the Argentona site, the three aquitards (3A) model proved to be better than the 1 aquitard (1A) model, confirming that thin heterogeneities in lithology have an important impact in hydraulic and transport behavior. The inclusion of more heterogeneity should be studied.
- The fit of heads time differences helps in recovering head fluctuations, which is important always, but especially when the mean absolute value of heads cannot be trusted, due to datum or salinity errors. The fit of the temporal variations makes the misfit in absolute

values more homogeneous in time. Fitting only the absolute values with no time correlation results in a good fit in some portions of the time series and a poor fit in others.

- Numerical dispersion can affect the parameter estimation problem and may be the cause of salinity in the freshwater zone, yielding an overall too conductive model when simulating CHERT.
- The HHCCR inverse problem reached the best salinity fit and passed the prediction capability tests with all types of data.

The calibrated hydrogeophysical model reproduces the main hydrological processes: long-term salinization, storm surges and the movement of the freshwater-saltwater interface in the transition zone. One-day rain events are not simulated by the model, most likely due to model dimension limitations and to the daily time discretization.

4 Calibration of density-dependent flow models using geoelectrical data: dealing with numerical dispersion

4.1 Introduction

The salinization of freshwater resources is a reality suffered by most regions of the world, due to natural reasons such as rainfall, rock weathering, seawater intrusion and aerosol deposits, but mostly because human activities accelerate it (Cañedo-Argüelles et al., 2019). Some of the factors increasing this global problem are the sustained increase in freshwater pumping, the excessive use of land for agricultural and commercial purposes, and natural (but also anthropic driven) processes like climate change and sea level variations (Werner et al., 2013). The fact is that these factors are present and we are not near reducing them, so the least we can do is to try to understand, monitor and manage them and their consequences in the best possible way.

Werner et al. (2013) pointed out that SWI studies were limited to steady-state conditions and that there were not enough field examples with model calibrations and model predictions. It is true that, for many years, scientists relied on analytical solutions, in hydrological point measurements (often inexact and only partially informative about the spatial extent of SWI and about the temporal processes). But improvements were made in the past 10 years in the study and characterization of SWI and submarine groundwater discharge (SGD) processes using geophysical data and examples of field studies and transient modelling can now be cited. SGD was studied in Belgium using electrical resistivity tomography (ERT) and frequency-domain electromagnetic methods (EM) (Paepen et al., 2020). Transient processes such as tides and storm surges in coastal aquifers based on surface ERT have been modeled (Huizer et al., 2017). Airborne EM has been used for monitoring SWI at a large scale (Goebel et al., 2019). Automatic calibration of SWI problems using hydrogeophysics has also been attempted (Beaujean et al., 2014; Coulon et al., 2021; Steklova and Haber, 2017b).

With the development of powerful open source software, we can now simulate in some detail many of the processes observed in the field, even if they are physically complex, numerically unstable, and, in practice, difficult to monitor. We have developed better experimental configurations to monitor SWI and SGD and we have numerical models to simulate these processes with great complexity. At the Argentona experimental site, we have conducted a long-term time-lapse cross-hole electrical resistivity tomography (CHERT) experiment which showed results of high quality and whose values were validated using other borehole geophysical logs (e.g. induction logs) (Palacios et al., 2020, Chapter 2). In the first attempts of calibrating the Argentona site SWI model, we performed the hydrological and the coupled hydrogeophysical inversion, and concluded that using hydrological data was not enough to represent all the processes observed in the Argentona site, namely storm surges, long-term salinization or heavy rain events, mainly because point measurements are not fitted to capture these events. The inclusion of geophysical data helped in the identification of the conceptual model and in the prediction of system behavior, but the use of this data was hindered by numerical dispersion and physical instability in the model.

Werner (2017) discusses the effects of mechanical and numerical dispersion present in density-dependent flow and transport models (like SEAWAT) when classifying SWI. When building the models, there is always a tradeoff between model size, model grid discretization and run times that must be considered for model predictions and, especially, calibration. Numerical dispersion has several effects on model results, and can prevent the correct simulation of the width of the mixing zone in density-dependent flow and transport models. Natural dispersion is responsible for the mixing zone, but in numerical simulations it is very hard to obtain undiluted freshwater or undiluted seawater in the model domain extremes. This means that a major part of the model is diluted, mixing zones are large and low salinity zones are reduced. This effect is increased if recharge is not taken into account and is larger near the inland border where SWI and freshwater encounter.

Water electrical conductivity (ECw) data is linearly correlated with salinity (Sen and Goode, 1992). In turn, ECw controls bulk or formation electrical conductivity (ECb) through petrophysical relations (Archie, 1942; Linde et al., 2006; Waxman and Smits, 1968). So, the errors of the salinity distribution are carried to the ECb data in a linear manner. This means that where salinity is low (between 0 and 3 g/L), but our model is unable to find salinities lower than 6 g/L, we have a minimum of 100% error in the salinity value which translates into 100% error in the modelled ECb value. This error is related solely to artificial numerical dispersion. Its propagation from the hydrological solver to the geophysical solver will obstruct the efficient use of geophysical data. Ferré et al. (2009) and Hinnell et al. (2010) discuss structural errors in the hydrological conceptual model and how they can damage the hydrogeophysical inversion results. Numerical dispersion is comparable to conceptual model errors, because the effect is essentially the same, an incorrect simulation of the hydrological process. So, what can we do when we cannot make the decision of using a sharp interface model or zero dispersion because we do have a transition zone, just not as large as the model shows?

This work aims at supporting the efforts of the hydrogeophysical community in integrating geophysical data with hydrological models, in exploiting its potential in a quantitative manner (Binley et al., 2015; Ferré et al., 2009; González-Quirós and Comte, 2020; Hinnell et al., 2010; Linde and Doetsch, 2016; Singha et al., 2014a) and in moving forward with the field applications of hydrogeophysical methodologies. The objective is to propose a hydrological model correction through the salinity-ECw relationship based on the cumulative distribution function (CDF). We conjecture that this correction would allow us to better exploit the time-lapse CHERT dataset.

4.2 Methodology

4.2.1 What we propose

The method that we propose is based on the modification of the salinity to ECw conversion. The link between hydrological and geoelectrical simulators is done through the conversion of the salinity distribution from the density-dependent flow and transport simulator into a ECw distribution. Then, the conversion from ECw to ECb is done through a petrophysical relation (Figure 4.1).

The conversion between salinity and ECw is usually done through a linear conversion (black line in Figure 4.1):

$$\sigma_w = b\omega \tag{4.1}$$

Where σ_w is ECw in S/m, b is a conversion factor equal to 0.1538 SL/mg in this study, and ω is water salinity in g/L. This conversion was applied in the hydrogeophysical model of Chapter 3.

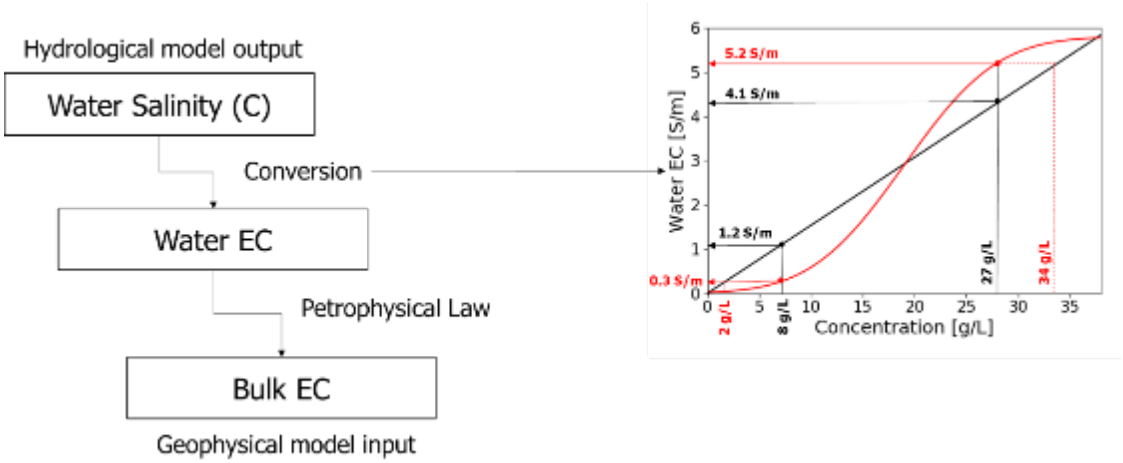

Figure 4.1. Link between hydrological and geoelectrical simulator (left panel). Water salinities from the hydrological model are first converted to water electrical conductivities (ECw) and then to bulk electrical conductivities (ECb) through a petrophysical law. The conversion law between water salinity and water EC are commonly linear, but we propose a cumulative distribution function (CDF) type conversion in order to correct the numerical dispersion of the hydrological simulator. The CDF-type conversion law would lower ECw in low salinity areas and increase it in high salinity areas.

Numerical dispersion appears in the model as a smoothing of the solution. Woods et al. (2003) shows that the maximum concentration diminishes with dispersion, causing the spatial distribution of concentration distribution to be broader, while narrowing the distribution of concentration values. Indeed, the salinity values from the SEAWAT models evidence that the high and low extremes are not well represented and that dispersion affects both the freshwater and the seawater zones. Ideally, we would like to have fresher water in the freshwater zone and saltier water in the seawater zone. To achieve this we propose to use a conversion with the shape of a CDF (see why in Section 4.2.2, below), the general case of the error function (red line in Figure 4.1 plot). In the figure, we can observe that with this type of conversion we would get what we look for. A salinity of 8 g/L represents 1.2 S/m after the linear conversion, but only 0.3 S/m with the CDF-type conversion. That is, 8 g/L of salt in the model would be simulated as only 2 g/L of salt in the geoelectrical solver. In the seawater side, a concentration of 27 g/L would change from 4.1 S/m with the linear conversion to 5.2 S/m with the CDF-type conversion, which would be ECw corresponding to salinity of 34 g/L. That is, the transformation corrects the artificial narrowing of the salinity values distribution or, equivalently, narrows down the width of the mixing zone.

4.2.2 Why using the cumulative distribution function (CDF)?

The shape of the CDF is the shape of the vertical salinity profiles and can be used to fit a salinity profile with a certain level of dispersion to a salinity profile with another level of dispersion. The scaled salinity at a point can be viewed as the CDF of the probability of SW molecules reaching such point. Therefore, it is natural to correct dispersion with a CDF transform. Choosing a Gaussian distribution is also a natural choice given the markovian nature of the advection-dispersion equation (ADE) adopted to simulate salinity transport. This is reflected in the Gaussian Green function of the ADE, which leads to error function-like distributions for advancing concentration fronts. This is illustrated in Figure 4.2, which displays the analytical solution of the ADE for a continuous injection. Figure 4.2a, b and c refer to three different times (10, 20, and 40 days) and three dispersivities (1E-3, 4E-3, and 1.6E-2 m). It is obvious that the dispersion coefficient can change the shape of the salinity profiles and that when the dispersion coefficient increases there is smoothing of the sigmoidal.

The CDF transform we propose is

$$CDF(x,\mu,\sigma) = \frac{1}{2}a\left[1 + ERF\left(\frac{x-\mu}{\sigma\sqrt{2}}\right)\right] \quad (4.2)$$

which depends on the mean μ and the standard deviation σ and can be scaled by the factor a. The mean translates the CDF in the x-direction so it is responsible for adjusting the center value, the standard deviation scales the x-direction and it is responsible for adjusting the width of the sigmoidal, which in the salinity profiles would mean a sharper or wider transition zone, and factor a shifts the sigmoidal in the y-direction. In order to change from one dispersion coefficient to another, we have to apply the CDF with a certain set of parameters. These parameters can be found automatically by solving an optimization problem that minimizes the misfit between the original and the desired curves. Figure 4.2a, b and c displays the fit when passing from a dispersion coefficient of 4E-3 m to 1E-3 m (green dots) and from 1.6E-2 m to 4E-3 m (red dots). In this figure we see that the fit is perfect for the analytical solution, so the CDF-type conversion can be used effectively to correct for dispersion. It must be noted that the optimized set of parameters depends on the dispersion level and doesn't need to be constant in time. Still, given that the width of the mixing zone in SWI should be relatively constant, we adopt a constant in time correction.

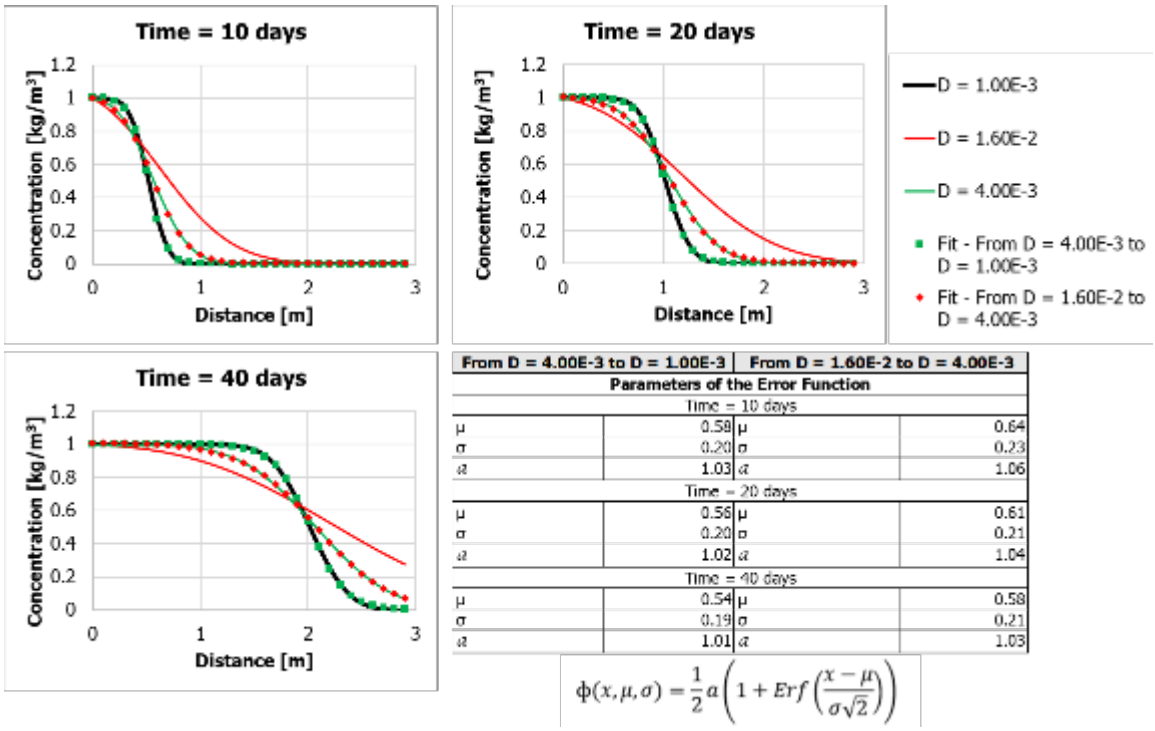

From D = 4.00E-3 to D = 1.00E-3		From D = 1.60E-2 to D = 4.00E-3
Parameters of the Error Function		
Time = 10 days		
μ	0.58	0.64
σ	0.20	0.23
a	1.03	1.06
Time = 20 days		
μ	0.58	0.61
σ	0.20	0.21
a	1.02	1.04
Time = 40 days		
μ	0.54	0.58
σ	0.19	0.21
a	1.01	1.03

$$\phi(x,\mu,\sigma) = \frac{1}{2}a\left(1 + Erf\left(\frac{x-\mu}{\sigma\sqrt{2}}\right)\right)$$

Figure 4.2. Illustration of the procedure to fit a salinity curve to another salinity curve with a given dispersion value. Three snapshots of the analytical solution of the advection-dispersion equation at 10, 20 and 40 days are displayed for three models ran with dispersion values: D = 1.0E-3 (black), 4E-3 (green) and 1.6E-2 (red). By optimizing the parameters of the CDF, each concentration curve can be changed from a modelled output to another output under different dispersion conditions (green and red dots). The table shows the optimal parameters and it can be observed that they change for each dispersion value and vary with time.

4.2.3 Modification of the HHCCR inverse problem.

We apply two modifications to the HHCCR inverse problem presented in Chapter 3, which from now on will be named "Linear" because of the salinity to ECw linear conversion. The first modification consists in changing the salinity to ECw conversion curve from the linear (blue curve in Figure 4.3) to the CDF-type conversion in the hydrogeophysical forward problem simulator (red and green curves in

Figure 4.3). The fixed parameters of the CDF in this problem are μ = 19 g/L, which represents the mid-point of 19 g/L of the salinity range from FW to SW in our model, and a=5.8 S/m, which represents the scaling of the CDF to reach the maximum ECw of the problem. The standard deviation, σ, has a value of 10 g/L for the CDF problem, merely a first guess for the behavior of the curve. The second modification to the Linear problem consists in changing the conversion curve and adding the standard deviation of the CDF as a parameter of the inverse problem to customize the conversion curve to the dispersion of, particularly, the Argentona hydrogeophysical model. Figure 4.3 illustrates the two new inverse problems named "CDF" and "CDF-STD".

The forward problem solvers and the spatial and temporal discretization remain the same as in Section 3.3.2. The observation groups and their relative weights also remain unchanged for the sake of comparison with the Linear problem solved in Chapter 3 (see Table 3.1).

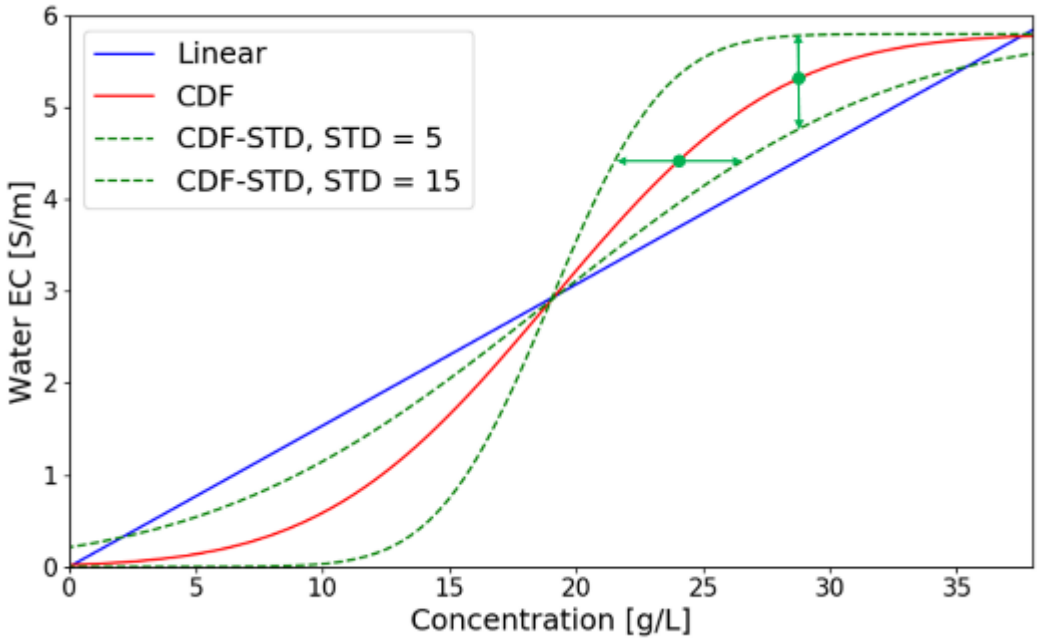

Figure 4.3. Conversion curves used to relate water salinities and water electrical conductivities. The linear conversion is the one originally used in the HHCCR inverse problem presented in Chapter 3. In the first modification of the inverse problem (CDF), we use the CDF-type conversion curve with fixed parameters: μ = 19 g/L, σ = 10 g/L, and a=5.8 S/m. In the second modification of the inverse problem (CDF-STD), we use the CDF-type conversion and include the CDF standard deviation in the parametrization. Green arrows illustrate the impacts of changing the standard deviation of the a priori CDF.

4.3 Results

The partial objective functions of problems HC and Linear, solved in Chapter 3, are presented in Table 4.1, along with the results from the CDF and CDF-STD problems. A weight equal to 1 was given to all data points to prepare this table, so as to compare the misfit between problems, which is why large differences are observed in the objective function values linked to each measurement type. Compared to the Linear problem, the CDF and the CDF-STD do not lower the misfit in the calibration period. In fact, they worsen them. Nevertheless, the CDF-STD has the lowest misfit values in the prediction period for the heads, heads time variations and the apparent resistivities from the CHERT experiment. The fact that the CDF solution leads to the worst predictions implies that the CDF transformation cannot be done blindly.

Table 4.1 also shows the estimated parameters. The inverse problem CDF and CDF-STD find hydraulic conductivity values for aquitard 3 in the order of 1E-5 m/d, and also a lower hydraulic conductivity for the weathered granite, less than 1 m/d. In the aquifers, the estimated hydraulic conductivities remain of the same magnitude. Overall, the CDF-STD problem estimates a less permeable model. Lateral inflow multipliers are very different from the ones obtained in Chapter 3. Figure 4.4 shows the estimated absolute values of the calibrated lateral inflow boundary condition. The Linear problem found that lateral inflow was higher in the deepest layer of the model. Results from CDF estimate that the largest amount of freshwater flows through Aquifer 3 (transition zone), and the CDF-STD problem estimates high freshwater inflow through Aquifer 2. These results contradict the a priori estimates but are consistent with the hydraulic test interpretation of del Val et al. (2021).

CDF-STD estimated a storm surge multiplier of 0.31 and a top freshwater recharge of 1.36, similar to the HC and the Linear problems. CDF estimates 1.77 for the storm surge multiplier and 0.95 for the top freshwater recharge, so a larger influence from the saltwater infiltration in the beach area is expected in the CDF model.

Both CDF and CDF-STD problems estimate a lower formation factor for the alluvial sediments, 5 and 11.83 respectively, less than the 15.34 estimated with the Linear problem. Finally, the standard deviation of the CDF was estimated to be 16. Figure 4.5 displays the salinity to ECw relations used in the the CDF and CDF-STD inverse problems: in red, the CDF used in CDF problem and as a starting point for CDF-STD problem, with a mean value of 19 g/L and a standard deviation of 10 S/m; in green, the result from the CDF-STD problem, which estimated a standard deviation of 16 S/m. The green line shows a smoother change from low to high water EC, creating a wider transition zone in the SWI context. We can also observe that pure freshwater (0 g/L of salt) has water EC of 0.24 S/m and pure seawater (38 g/L), has water EC of 5.5 S/m.

Figure 4.6 displays the modelled apparent resistivity of the CHERT experiment. Figure 4.6a corresponds to the calibration period, July 2015. We can observe that the results from the CDF and CDF-STD problem are more resistive, and also more dispersive. Figures 4.6b, c and d are from the validation period, October 2016, February 2017 and September 2017 respectively. The simulation of the CHERT from October 2016, acquired 10 days after a heavy-rain event, are better fitter by CDF model in panels PP20-PP15 and PP15-N125, but then it is too resistive moving further inland. The CHERT from February 2017, when storm surges occurred, is better fitted by model CDF-STD. CDF model is overall conductivity in this date, most likely due to an overestimation of the saltwater infiltration during the storm surge. In September 2017, model CDF is still too conductive in panels from PP20 to N1. The Linear model fits the CHERT dataset better than model CDF.

Figure 4.7 displays the water salinities observed and computed with the Linear, CDF and CDF-STD models. The grey and white area show the calibrated and predicted data points respectively. In the freshwater zone, the CDF and CDF-STD models estimate a lower salinity than the Linear model. The CDF-STD is the model reaching the lowest salinity, XX g/L. In the transition zone, estimated salinities with models CDF and CDF-STD are lower than salinities from the Linear model. The CDF-STD respect the salinization trend from the dataset, which is not the case for piezometer N320 in the CDF model. In the seawater zone, the CDF and CDF-STD models also display lower salinities than the Linear model. The results of the three models follow the same trend in piezometers N120, N125 and N225. Model CDF is the only one that displays the decrease in salinity in piezometer N325.

Figure 4.8 shows the results of the modelled head time series using inverse problems Linear (blue), CDF (red) and CDF-STD (green) and the observed data (black). The grey and white area show the calibrated and validated data points respectively. We can point out that models CDF and CDF-STD estimate slightly higher heads, a few centimeters above the Linear model. In the prediction period, model CDF overestimates the head increase of approximately 30 cm in the piezometers from the freshwater and the transition zones during storm days.

	Parameters	HC	Linear	CDF	CDF-STD	A priori
Hydraulic Conductivities	Freewater Table	3.0E-3	2.4E-1	1.6E-1	6.7E-1	1.0E-1
	Aquifer 1	3.68	5.67	5.41	8.00	10.00
	Aquitard 1	1.0E-2	2.0E-2	2.6E-2	1.8E-2	1.0E-2
	Aquifer 2	13.50	15.79	6.23	4.04	31.60
	Aquitard 2	2.5E-2	5.0E-2	1.4E-1	2.1E-2	1.0E-2
	Aquifer 3	81.61	65.00	13.66	11.44	31.60
	Aquitard 3	1.3E-4	1.7E-4	5.2E-5	6.5E-5	1.0E-2
	Weathered Granite	5.51	2.11	0.51	0.56	10.00
Lateral Inflow Multipliers	Aquifer 1	0.91	2.00	0.04	10.99	1.00
	Aquifer 2	1.13	5.56	3.70	18.50	2.00
	Aquifer 3	0.91	4.44	11.30	4.44	2.00
	Weathered Granite	1.06	6.98	0.62	1.87	10.00
Multipliers	Storm Surge Flux	0.19	0.34	1.77	0.31	1.00
	Top Recharge Flux	1.39	1.28	0.95	1.36	4.00
Formation Factor	Alluvial Sediments		15.34	5.00	11.83	6.00
	Weathered Granite		17.68	17.89	17.94	18.00
Standard Deviation of the CDF	All layers		-	10.00	15.99	10.00
	Partial Objective Functions ϕ					
Calibration Period	*h*	27.02	40.55	59.59	73.80	
	hh		3.36	5.83	8.90	
	c	3032.75	2535.87	5872.32	11075.48	
	cc		2888.37	3721.76	4454.32	
	rho		3.4E+6	1.0E+7	5.2E+6	
Validation Period (Prediction)	*h*	64.26	68.73	147.00	45.81	
	hh	10.72	9.50	83.84	8.56	
	c	18890.41	30596.80	55518.00	72483.37	
	cc	4831.18	4524.93	8433.00	8794.09	
	rho	2.6E+6	1.5E+6	7.0E+6	1.3E+6	

Table 4.1. Summary of the results of the inverse problems CDF and CDF-STD. The results from the HC and the Linear problems solved in Chapter 2 and the a priori values of the calibrated parameters are shown for comparison. The hydraulic conductivities found by the inverse problems CDF and CDF-STD problems are similar to the HC and the Linear problem results in the aquifer layers, but one order of magnitude lower in aquitard 3 and the weathered granite. The arrangement of the fresh groundwater flow from the CDF and the CDF-STD problems changes drastically from the a priori values and previous results, putting most of the flow through the alluvial aquifer layers and not the weathered granite. Problem CDF found a higher value for the storm surge multipliers. The estimated values for the formation factor of the alluvial layers were also reduced to 5 and 11.83, in comparison with the 15.34 found in the Linear inverse problem. These values are closer to the expected value. The CDF standard deviation changed from 10 to 16 during the calibration process. For the comparison of the objective functions, all data points were given the same weight of 1.0. It can be observed that neither the CDF nor the CDF-STD problems reduced the misfits in the calibration period, but problem CDF-STD has the lowest misfits in the validation period.

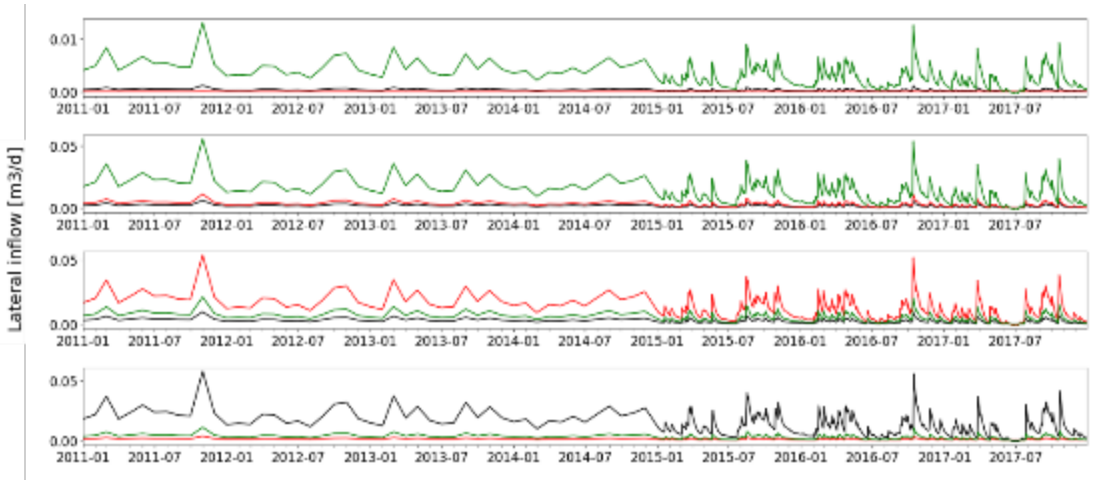

Figure 4.4. A priori (black), CDF (red) and CDF-STD (green) estimated values for the lateral inflow boundary conditions of the hydrogeophysical model. The CDF problem finds that the highest fresh groundwater flow passes through aquifer 3, while CDF-STD problem estimates that the highest lateral inflow goes through aquifers 1 and 2.

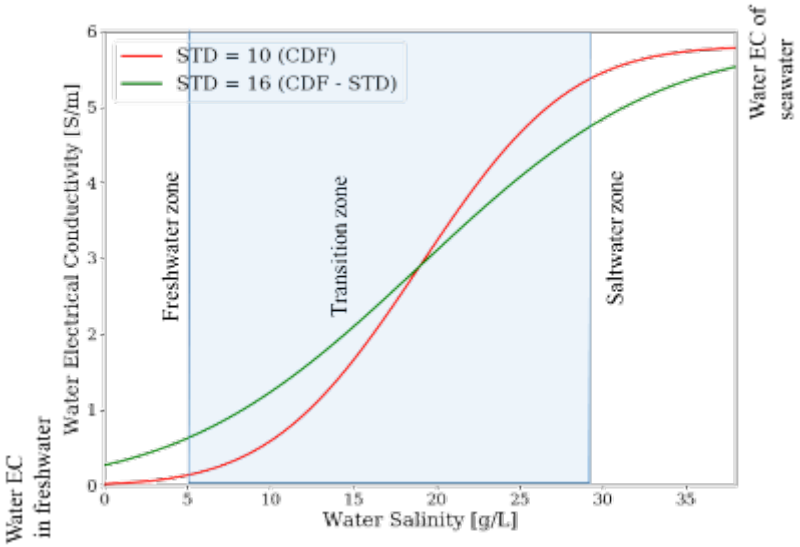

Figure 4.5. A priori (red) and estimated (green) salinity vs. ECw relations. Inverse problem CDF-STD found a value of 16 for the CDF standard deviation, creating a smoother conversion line and, consequently, wider transition zone. According to the estimated curve, pure freshwater would have a minimum water EC of 0.24 S/m, and seawater with 38 g/L of salt would have a ECw of 5.5 S/m. Both extreme values are consistent with Argentona site data.

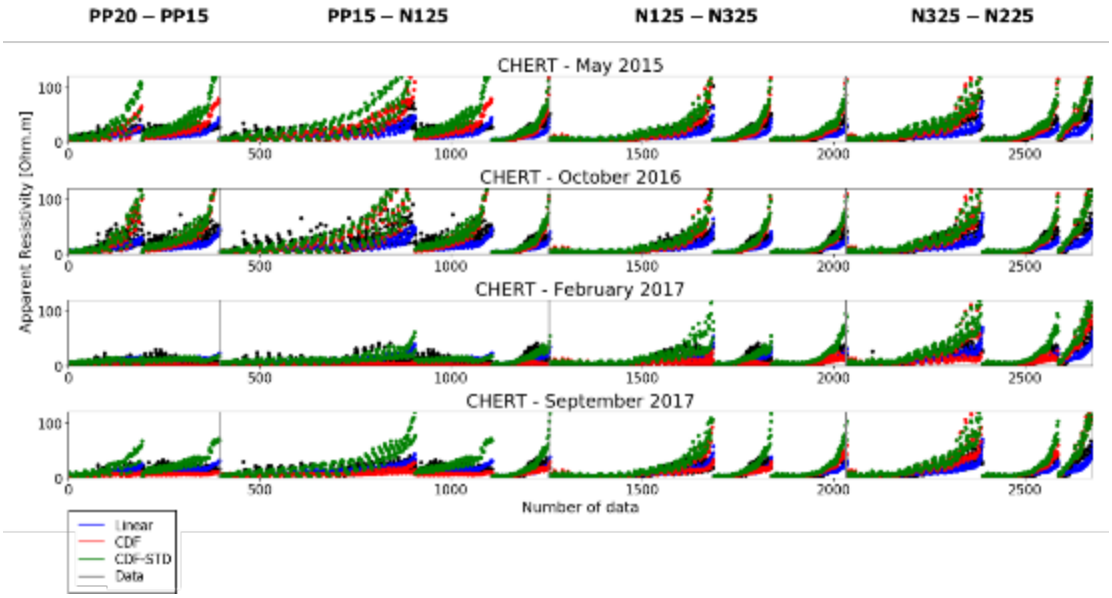

Figure 4.6. Result of the calibration of the apparent bulk electrical resistivity (rho) using the Linear, CDF and CDF-STD inverse problems. CHERT panels PP20-PP15 and PP15-N125 are on the beach area and are the most affected by the storm surges that occurred early 2017. The CDF inverse problem yields too low resistivities in both panels from February 2017 and September 2017, suggesting an overestimation of the saltwater infiltration. With the CDF-STD the simulated bulk apparent resistivities in the prediction period respect the change from more conductive to more resistive in each panel, although it still doesn't reproduce the dispersive behavior of the points in panels PP20-PP15 and PP15-N125 after the heavy rain episode in October 2016.

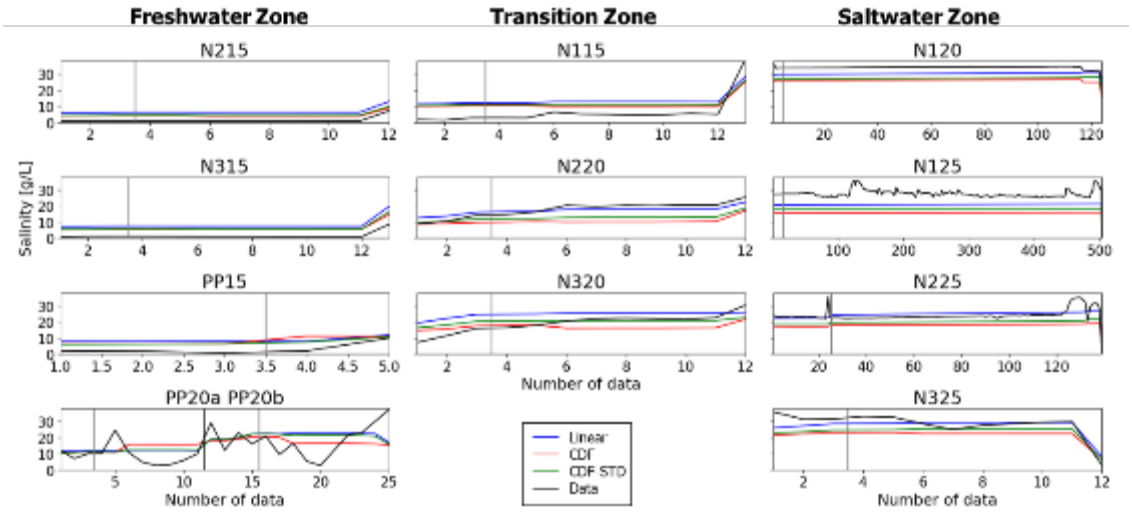

Figure 4.7. Result of the simulated salt concentrations using the Linear, CDF and CDF-STD inverse problems. The grey area denotes the data points that were calibrated and the white area shows the non-calibrated data points belonging to the validation period. The estimated salinity in the freshwater zone lowers with both CDF and CDF-STD estimations. In the transition zone, CDF-STD estimation follows the salinization trend, better than the CDF estimation. In the saltwater zone, the estimated salinity is lower than with the Linear problem, and the decreasing trend in N325

is not reproduced. Overall, the estimated absolute values are not far from field measurements, except in the PP20a borehole, where the predictions for model CDF are too high.

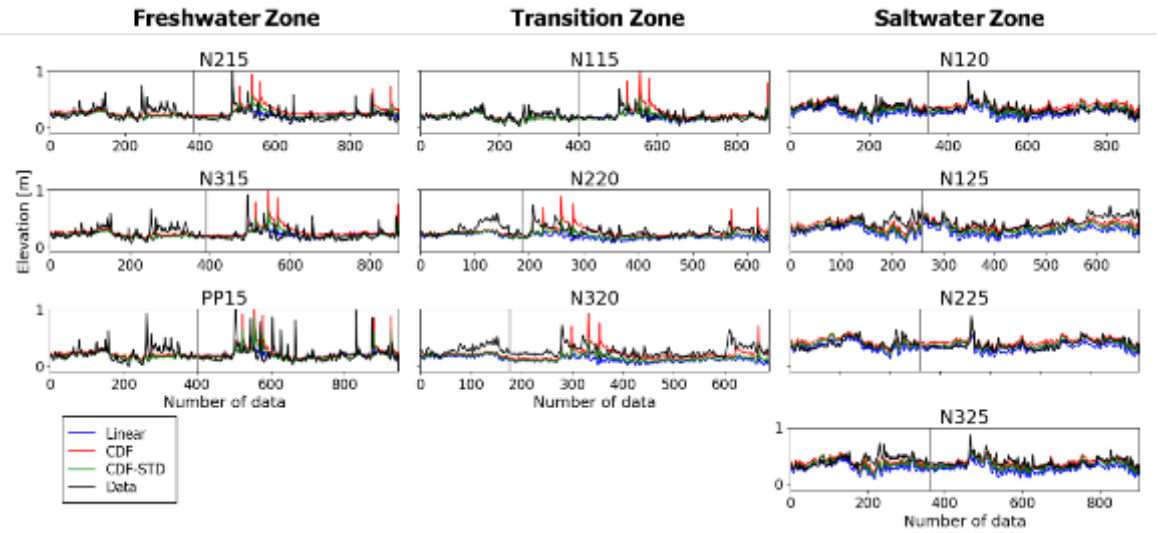

Figure 4.8. Result of the calibration of the heads observation group using the Linear, CDF and CDF-STD inverse problems on the three aquitard (3A) model. The grey area denotes the data points that were calibrated and the white area shows the non-calibrated data points belonging to the validation period. The calibrated head values of models CDF and CDF-STD are better for all piezometers. In the validation period, however, the CDF model overestimated the head increase during the days of storm surge.

Figure 4.9 shows the time-lapse images of the salinity distribution from the CDF-STD model, alongside with those from the Linear model. The CDF-STD model differentiates the freshwater zone, above -9 m a.s.l, and the transition zone, between -9 and -17 m a.s.l. Below the SWI, we find fresher water below the silt layer at -17 m a.s.l, inside the weathered granite layer. The main difference between the Linear and the CDF-STD model is that the freshwater zone reaches lowest salinities in the CDF-STD model. In general, the new salinity images display a less dispersive character.

4.4 Discussion

4.4.1 The optimized CDF-type conversion and the width of the transition zone.

By checking the Argentona site data from extracted water samples, we find that piezometers from the freshwater zone have a mean ECw of 0.12 S/m and that seawater samples have a mean ECw of 5.33 S/m. Having ECw of 0.24 S/m for the model pure freshwater and 5.5 S/m for the model saltwater is considered correct, because in real life, we would never find a water EC of 0 S/m in freshwater samples. In fact, a significant salinity may be reached by recharging water as a result of aerosol deposition.

The estimated CDF-type conversion corresponds to a wide transition zone. Previous studies (Beaujean et al., 2014; Coulon et al., 2021; Herckenrath et al., 2013a) had calibrated the dispersion coefficient, and still found that salinity was not properly estimated using low resolution geophysical data without salinity from water samples.. With the CHERT experiment, resolution issues were solved but the low concentrations were still not well represented due to a numerical dispersion problem. As stated by Hinnell et al. (2010), structural hydrological model issues will prevent the hydrogeophysical inversion from working, because in a coupled inversion it is the hydrological simulator that drives the interpretation of all datasets, including the geophysical one. Another recent study from Coulon et al. (2021), thanks to the size and resolution of their model, removed the transition zone by using a sharp

interface model and did not report dispersion issues in their results. However, in coastal aquifers, we cannot always remove the transition zone, where important chemical exchanges occur.

Although we have not formally studied the degree of dispersion at the Argentona site, we knew thanks to the time-lapse CHERT images that we were dealing with a highly dispersive site, with a transition zone of several meters that moved laterally and vertically. This dispersion was not, however, represented in the hydrological model with a proper a priori knowledge. The numerical dispersion issue observed in the hydrological model represented a problem in the calibration of the model, and made us realize that calibrating the numerical model dispersion was necessary to fit the data. Density-dependent flow and transport models try to model a complex physical problem, and very often have convergence issues, so the calibration of this parameter may not always be an easy choice for the stability of the solution. The methodology proposed addresses the dispersion of the model, without directly disturbing the hydrological model stability and directly affecting the calibration of the bulk apparent resistivities.

It is relevant to recall that the problem solved in this study assumes constant dispersivity in the whole model domain, and at all times. This is not the case with dispersion, as illustrated in Figure 4.2, and we could think of trying to fit different conversion curves for each model layer and for each time, but this would increase the number of parameters and, consequently when using optimization tools based on finite differences for the computation of the gradient, increase not only the computation time needed to solve the inverse problem, but also identifiability difficulties.

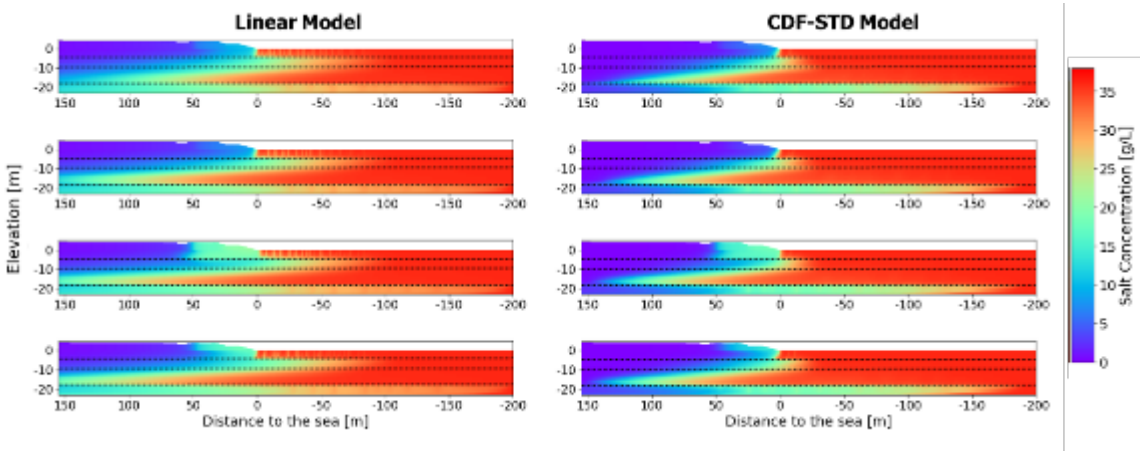

Figure 4.9. Time-lapse view of the simulated spatial distribution of salinity computed with the Linear and the CDF-STD models. Black lines show the position of the silt layers at -5, -9 and -17 m a.s.l, known to limit the SWI. The main difference between both models is the salinity of the freshwater zone of the model. The salinity distribution is less dispersive in the upper part of the model, above the silt layers at -5 and -9 m a.s.l. In the beach area, the effect of storm surges completely disappeared in June 2016, and the washout is more visible in September 2017, for the CTD-STD model.

4.4.2 The change in the estimated parameters post numerical dispersion correction.

A formation factor of 5 was found for the alluvial sediments in CDF model. This value corresponds to very porous rocks with 35 to 40% of porosity, and it was imposed as the lower limit of the inverse problem solution thanks to our knowledge of the site. This results in the CDF model indicates that the changes in the other parameters may be affected by this lower limit restriction. In the best case, the parameters move freely in the allowed space, without being constrained by the limits. It is not a surprise that model CDF did not perform well in the prediction capability test. Model CDF-STD found a

formation factor value of 11.83, without being constrained by the bounds imposed to the inverse problem. Although higher than 6, the a priori value, it still corresponds to our a priori knowledge of the site alluvial layers with porosities around 20-25%.

4.4.3 The best model: worst calibration fit but best prediction capabilities.

Given the results obtained in the validation period, we conclude that CDF-STD is the hydrogeophysical model that best represents the Argentona site. Paradoxically, it is not the one that yields the lowest misfits in the calibration period, as shown in Table 4.1. As was discussed in Chapter 3, our concept of the best model lies on its prediction capabilities, reason why part of the Argentona site monitoring data was saved to be part of a validation period. Although it represented more workload and it could have affected the stability of the inverse problem, the standard deviation of the CDF was added as parameter of the inverse problem, and it improved the results. In terms of convergence, we can also point out that models CDF and CDF-STD had a better convergence in the optimization process in terms of number of iterations and in terms of forward problem convergence than the Linear problem.

Model CDF-STD is able to reproduce fairly well the Argentona site response to external factors like sea level changes, freshwater recharge from the top and from the subsurface layers and saltwater recharge during storm surges (Figure 4.9, time-lapse view).

4.4.4 The Argentona site conceptual model improvements: the before and after calibration.

Now that the hydrogeophysical inversion of the Argentona site has been completed, we can update our knowledge about the site.

- Inverse problem results show that the aquitard layer at -5 m.a.s.l. is very important for protecting the freshwater zone in Aquifer 2 where piezometers N215, N315 and PP15 sample. The CDF problem simulation evidences that large saltwater fluxes on the beach area, in times of storm surges, would produce a large response in Aquifers 2 and even 3, below Aquitard 2, and would salinize the model according to CHERT results.
- The weathered granite layer has low hydraulic conductivity, of less than 1 m/d. Fresh groundwater flow still goes through it, which is why we find lower salinity values in N125 trapped below aquitard 3.
- The change in hydraulic behavior between piezometers with the screen at 20 m and at 25 m depth is explained by a strong hydraulic barrier, which was estimated to have a hydraulic conductivity as low as 1E-5 m/d. This very low hydraulic conductivity might be attributed to other type of heterogeneities which are not represented in a simple layer model. However, the presence of this barrier is necessary for model fitting and predictions.
- The estimated top freshwater recharge was not changed importantly (maximum of 30 percent increase) during the calibration, meaning that the soil balance is satisfactory. Freshwater recharge must also be taken into account in the models to control the dispersion effect.
- Our observations of the transition zone movement with the time-lapse CHERT experiment determined the presence of an aquifer with a transition zone of a few meters moving laterally and vertically. The calibrated CDF curve shows that the Argentona site data is fitted with a dispersive curve that respects this transition zone.

- The fresh groundwater flow is higher in the upper layers of the model, through the alluvial aquifer layers. It would be interesting to check with a 3D model at which extent the flow through the Argentona ephemeral stream is responsible for these high fluxes at these depths.
- As the cores extracted from the piezometers show formations that are loosely compacted, our initial hypothesis was of a low cementation factor (m=1.5) and porosities for the alluvial layers and the weathered granite around 20-30% and 15% respectively. Our findings for the formation factor (11.83 for the alluvial sediments and 18 for the weathered granite) back up this initial hypothesis, with alluvial layers with porosities of 20%.

4.5 Conclusions

- The prediction capability of the inverted model was improved by means of a new relationship between the water salinity and water electrical conductivity. The CDF-type conversion accounted for the numerical dispersion correction, and fitted the model numerical dispersion to one that can better explain the Argentona site dataset.
- The estimated parameters are realistic, in the sense that formation factors and aquifer permeabilities are in accordance with the expected values. Where we don't have much a priori knowledge we cannot reach this type of conclusion (fresh groundwater fluxes for example), but correcting formation factors estimation was feasible, and it improved the prediction capability of the hydrogeophysical model.
- Fresh groundwater flow multipliers were increased in the upper part of the density-dependent flow and transport model, with higher fluxes in the aquifer layers than in the weathered granite layer.
- The storm surges event had such a visible response in the CHERT experiment, that it was a key event to test the prediction capability of the inverted models.

Conscious of the limitations of the 2D models when studying 3D real experiments, we can still affirm that the current Argentona hydrogeophysical model can effectively predict system responses to stimuli like sea level variations, precipitation, storm surges, and fresh groundwater fluxes from inland. The presented methodology proved to be a good strategy to take more information out of the time-lapse CHERT experiment, circumventing the non-trivial issues of numerical dispersion related to the hydrological model.

5 General conclusions

The main objective of this thesis was to test the capacity of the joint use of high resolution geoelectrical data and hydrological data for the qualitative interpretation and quantitative characterization of a coastal aquifer and for the visualization of transient processes. In this regard, time-lapse cross-hole electrical resistivity tomography (CHERT) was used for the imaging and monitoring of seawater intrusion dynamics in a Mediterranean alluvial aquifer and we can draw the following conclusions from the use of this dataset.

The use of bulk electrical conductivity (EC) from time-lapse CHERT contributed in giving insights on the dynamics of seawater intrusion, as well as on the conceptual model of the Argentona site, in a cost-effective and efficient way. Despite the high salinity of water, which created a corrosive environment for the stainless-steel mesh electrodes used for the CHERT acquisition, the CHERT experiment provided with high resolution images, with very limited loss of resolution in depth, and allowed us to capture salinity changes in the upper and lower layers of the site, which led to the realization that, contrary to expectations, several seawater wedges are present at the site.

Surface ERT is a non-invasive method and easy to deploy on site, and it is the most common geophysical tool for imaging the seawater intrusion. Surface ERT has very high sensitivity to EC changes near the surface, but suffers from resolution loss in depth. We used jointly the surface ERT and CHERT datasets to increase the resolution of the initial model of the time-lapse CHERT monitoring. The goodness of the bulk EC dataset was confirmed by an excellent correlation between the CHERT inverted images and the induction logs.

Time-lapse CHERT imaged long-term and short-term conductivity changes. Long-term changes included (1) seasonal fluctuations of groundwater flux that make the freshwater-seawater transition zone to move seawards or landwards; and (2) the salinization of the aquifer below the silt layer at -9 m a.s.l, where the seawater intrusion is found, related to a drought in the study area during the years of monitoring. Short-term changes include (1) a decrease in bulk EC linked to a one-day heavy-rain event, typical in the study area during Autumn; and (2) an increase in bulk EC in the beach area related to storm surges caused by enhanced wave activity.

A hydrogeophysical model of the Argentona site was created in order to simulate the various transient hydrological processes that occurred in the study area during the two years of monitoring. The hydrogeophysical model couples a density-dependent flow and transport simulator with a geoelectrical problem simulator through a petrophysical law relating water salinity to bulk EC. This hydrogeophysical model was then linked to an optimization tool that uses a Gauss-Newton solver to estimate the model parameters by fitting simulated and observed data.

Two conceptual models from the Argentona site were tested with the calibration of hydraulic heads and salinity: a model with one aquitard, which was the original conceptual model of the site; and a

model with three aquitards, which was the update of the conceptual model after including the observations made with the time-lapse CHERT and tidal response testing. The one aquitard model did not pass the prediction test, while the three aquitard model fitted the data and was better at predicting system responses, proving that small-scale heterogeneities can have an impact in the hydraulic behavior of the aquifer.

Three inverse problems were solved using the three aquitards conceptual model: (1) HC, the traditional hydrological inversion based on the fit of hydraulic heads and salt concentrations; (2) HHCC, an inverse problem including head time variations and salinity variations along piezometers nests, searching to address typical issues of point measurements of heads and concentrations; and (3) HHCCR, an inverse problem using all the above datasets plus the bulk apparent resistivity of the time-lapse CHERT. By comparing the three inverse problems, we observed that the model obtained with HHCCR reached the best salinity fit and passed the prediction tests with all types of data. Problem HHCC highlighted that fitting heads values yields a model with a good fit in some portions of the time series and a poor fit in others, which is not ideal when trying to reproduce transient processes correlated in time.

The modelling process unveiled numerical dispersion issues related to the encounter between saltwater and fresh groundwater at the inland boundary during the pseudo-steady state phase. Numerical dispersion prevents the density-dependent flow and transport model from simulating correctly the pure freshwater zone and the pure saltwater zone, due to the mixture of both waters. Errors in simulated salinities affected the simulated bulk apparent resistivities. This dispersion is proper of the hydrological simulator and led to unexpected values for the formation factor of the alluvial aquifers.

We proposed a methodology to correct the numerical dispersion effect during the conversion from simulated salt concentrations to water EC. The method is based on changing from a linear conversion to a cumulative distribution function (CDF) type conversion. We showed with analytical solutions that we can correct salinity distributions from one dispersion value to another by fitting the CDF parameters (mean, standard deviation and scale factor). Results from the inverse problem showed that the prediction capability was improved by changing the conversion curve. The estimated parameters were realistic and formation factors were in agreement with the expected values.

The current calibrated Argentona hydrogeophysical model was found by fitting hydraulic heads, heads time variations, water salinity, spatial water salinity changes, and bulk electrical resistivities. The model can effectively predict the responses of the Argentona site to factors such as sea level variations, precipitations, storm surges, and fresh groundwater fluxes from inland. The presented methodology proved to be a good strategy to take a maximum of information out of the time-lapse CHERT experiment, and to circumvent the non-trivial numerical dispersion issue present in the density-dependent flow and transport simulators.

6 Bibliography

Abarca, E., Carrera, J., Sánchez-Vila, X. and Dentz, M.: Anisotropic dispersive Henry problem, Adv. Water Resour., 30(4), 913–926, doi:10.1016/j.advwatres.2006.08.005, 2007.

Ainsworth, T.: When Do Ocean Waves Become "Significant"? A Closer Look at Wave Forecasts. [online] Available from: https://www.vos.noaa.gov/MWL/apr_06/waves.shtml, 2006.

Archie, G. E.: The Electrical Resistivity Log as an Aid in Determining Some Reservoir Characteristics, Trans. AIME, doi:10.2118/942054-G, 1942.

Beaujean, J., Nguyen, F., Kemna, A., Antonsson, A. and Engesgaard, P.: Calibration of seawater intrusion models: Inverse parameter estimation using surface electrical resistivity tomography and borehole data, Water Resour. Res., 50(8), 6828–6849, doi:10.1002/2013WR014020, 2014.

Bellmunt, F. and Marcuello, A.: Method to obtain standard pseudosections from pseudo pole–dipole arrays, J. Appl. Geophys., 75(3), 419–430, doi:10.1016/J.JAPPGEO.2011.07.020, 2011.

Bellmunt, F., Marcuello, A., Ledo, J., Queralt, P., Falgàs, E., Benjumea, B., Velasco, V. and Vázquez-Suñé, E.: Time-lapse cross-hole electrical resistivity tomography monitoring effects of an urban tunnel, J. Appl. Geophys., 87, 60–70, doi:10.1016/j.jappgeo.2012.09.003, 2012.

Bellmunt, F., Marcuello, A., Ledo, J. and Queralt, P.: Capability of cross-hole electrical configurations for monitoring rapid plume migration experiments, J. Appl. Geophys., 124, 73–82, doi:10.1016/J.JAPPGEO.2015.11.010, 2016.

Ben-Zur, E., Gvirtzman, H. and Shalev, E.: Haline Convection within a Fresh-Saline Water Interface in a Stratified Coastal Aquifer Induced by Tide, Water, 13(13), 1780, doi:10.3390/w13131780, 2021.

Bergmann, P., Schmidt-Hattenberger, C., Kiessling, D., Rücker, C., Labitzke, T., Henninges, J., Baumann, G. and Schütt, H.: Surface-downhole electrical resistivity tomography applied to monitoring of CO2 storage at Ketzin, Germany, Geophysics, 77(6), doi:10.1190/geo2011-0515.1, 2012.

Binley, A., Slater, L. D., Fukes, M. and Cassiani, G.: Relationship between spectral induced polarization and hydraulic properties of saturated and unsaturated sandstone, Water Resour. Res., 41(12), 1–13, doi:10.1029/2005WR004202, 2005.

Binley, A., Hubbard, S. S., Huisman, J. A., Revil, A., Robinson, D. A., Singha, K. and Slater, L. D.: The emergence of hydrogeophysics for improved understanding of subsurface processes over multiple scales, Water Resour. Res., doi:10.1002/2015WR017016, 2015.

Blainey, J. B., Ferré, T. P. A. and Cordova, J. T.: Assessing the likely value of gravity and drawdown measurements to constrain estimates of hydraulic conductivity and specific yield during unconfined aquifer testing, Water Resour. Res., 43(12), doi:10.1029/2006WR005678, 2007.

Bussian, A. E.: Electrical conductance in a porous medium, Geophysics, 48(9), 1258–1268, doi:10.1190/1.1441549, 1983.

Cañedo-Argüelles, M., Kefford, B. and Schäfer, R.: Salt in freshwaters: Causes, effects and prospects - Introduction to the theme issue, Philos. Trans. R. Soc. B Biol. Sci., 374(1764), doi:10.1098/rstb.2018.0002, 2019.

Carrera, J. and Neuman, S. P.: Estimation of Aquifer Parameters Under Transient and Steady State Conditions: 1. Maximum Likelihood Method Incorporating Prior Information, Water Resour. Res., 22(2), 199–210, doi:10.1029/WR022i002p00199, 1986.

Carrera, J., Hidalgo, J. J., Slooten, L. J. and Vázquez-Suñé, E.: Computational and conceptual issues in the calibration of seawater intrusion models, Hydrogeol. J., 18(1), 131–145, doi:10.1007/s10040-009-0524-1, 2010.

Castro-Alcalá, E.: Laboratory experiments to evaluate the joint effect between heterogeneity and head fluctuation on mixing, effective porosity and tailing, UPC, Escola Tècnica Superior d'Enginyers de

Camins, Canals i Ports de Barcelona. [online] Available from: http://hdl.handle.net/2117/134623, 2019.

Chasseriau, P. and Chouteau, M.: 3D gravity inversion using a model of parameter covariance, J. Appl. Geophys., 52(1), 59–74, doi:10.1016/S0926-9851(02)00240-9, 2003.

Claerbout, J. F. and Muir, F.: Robust Modeling With Erratic Data, Geophysics, 38(5), 826–844, doi:10.1190/1.1440378, 1973.

Comte, J. C. and Banton, O.: Cross-validation of geo-electrical and hydrogeological models to evaluate seawater intrusion in coastal aquifers, Geophys. Res. Lett., 34(10), doi:10.1029/2007GL029981, 2007.

Constable, S. C., Parker, R. and Constable, C.: Occam's inversion: A practical algorithm for generating smooth models from electromagnetic sounding data, Geophysics, 52(3), 289–300, doi:10.1190/1.1442303, 1987.

Costall, A., Harris, B. and Pigois, J. P.: Electrical resistivity imaging and the saline water interface in high-quality coastal aquifers, Surv. Geophys., 39(4), 753–816, doi:10.1007/s10712-018-9468-0, 2018.

Costall, A. R., Harris, B. D., Teo, B., Schaa, R., Wagner, F. M. and Pigois, J. P.: Groundwater Throughflow and Seawater Intrusion in High Quality Coastal Aquifers, Sci. Rep., 10(1), doi:10.1038/s41598-020-66516-6, 2020.

Coulon, C., Pryet, A., Lemieux, J. M., Yrro, B. J. F., Bouchedda, A., Gloaguen, E., Comte, J. C., Dupuis, J. C. and Banton, O.: A framework for parameter estimation using sharp-interface seawater intrusion models, J. Hydrol., 600, doi:10.1016/j.jhydrol.2021.126509, 2021.

Daily, W., Ramirez, A., LaBrecque, D. and Nitao, J.: Electrical resistivity tomography of vadose water movement, Water Resour. Res., 28(5), 1429–1442, doi:10.1029/91WR03087, 1992.

Dewandel, B., Lachassagne, P., Wyns, R., Maréchal, J. C. and Krishnamurthy, N. S.: A generalized 3-D geological and hydrogeological conceptual model of granite aquifers controlled by single or multiphase weathering, J. Hydrol., 330(1–2), 260–284, doi:10.1016/j.jhydrol.2006.03.026, 2006.

Dietrich, S., Carrera, J., Weinzettel, P. and Sierra, L.: Estimation of Specific Yield and its Variability by Electrical Resistivity Tomography, Water Resour. Res., 54(11), 8653–8673, doi:10.1029/2018WR022938, 2018.

Doetsch, J., Linde, N., Vogt, T., Binley, A. and Green, A. G.: Imaging and quantifying salt-tracer transport in a riparian groundwater system by means of 3D ERT monitoring, GEOPHYSICS, 77(5), B207–B218, doi:10.1190/geo2012-0046.1, 2012.

Doherty, J.: Calibration and Uncertainty Analysis for Complex Environmental Models PEST: complete theory and what it means for modelling the real world. [online] Available from: www.pesthomepage.org, 2015.

Falgàs, E., Ledo, J., Marcuello, A. and Queralt, P.: Monitoring freshwater-seawater interface dynamics with audiomagnetotelluric data, Near Surf. Geophys., 7(5–6), 391–399, doi:10.3997/1873-0604.2009038, 2009.

Falgàs, E., Ledo, J., Benjumea, B., Queralt, P., Marcuello, A., Teixidó, T. and Martí, A.: Integrating hydrogeological and geophysical methods for the characterization of a deltaic aquifer system, Surv. Geophys., 32(6), 857–873, doi:10.1007/s10712-011-9126-2, 2011.

Ferré, T., Bentley, L., Binley, A., Linde, N., Kemna, A., Singha, K., Holliger, K., Huisman, J. A. and Minsley, B.: Critical Steps for the Continuing Advancement of Hydrogeophysics, Eos, Trans. Am. Geophys. Union, 90(23), 200, doi:https://doi.org/10.1029/2009EO230004, 2009.

Flores-Orozco, A., Kemna, A. and Zimmermann, E.: Data error quantification in spectral induced polarization imaging, GEOPHYSICS, 77(3), E227–E237, doi:10.1190/geo2010-0194.1, 2012.

Folch, A., del Val, L., Luquot, L., Martínez-Pérez, F., Bellmunt, F., Le Lay, H., Rodellas, V., Ferrer, N., Palacios, A., Fernández, S., Marazuela, M. A., Diego-Feliu, M., Pool, M., Goyetche, T., Ledo, J., Pezard, P., Bour, O., Queralt, P., Marcuello, A., Garcia-Orellana, J., Saaltink, M. W., Vazquez-Suñe, E. and Carrera, J.: Combining Fiber Optic (FO-DTS), CHERT and time-lapse formation electrical conductivity to characterize and monitor a coastal aquifer, 2019.

Folch, A., del Val, L., Luquot, L., Martínez-Pérez, L., Bellmunt, F., Le Lay, H., Rodellas, V., Ferrer, N., Palacios, A., Fernández, S., Marazuela, M. A., Diego-Feliu, M., Pool, M., Goyetche, T., Ledo, J., Pezard, P., Bour, O., Queralt, P., Marcuello, A., Garcia-Orellana, J., Saaltink, M. W., Vázquez-Suñé, E. and Carrera, J.: Combining fiber optic DTS, cross-hole ERT and time-lapse induction logging to characterize and monitor a coastal aquifer, J. Hydrol., 588, doi:10.1016/j.jhydrol.2020.125050, 2020.

de Franco, R., Biella, G., Tosi, L., Teatini, P., Lozej, A., Chiozzotto, B., Giada, M., Rizzetto, F., Claude, C., Mayer, A., Bassan, V., Gaspar and Etto-Stori, G.: Monitoring the saltwater intrusion by time lapse electrical resistivity tomography: The Chioggia test site (Venice Lagoon, Italy), J. Appl. Geophys., 69(3–

4), 117–130, doi:10.1016/j.jappgeo.2009.08.004, 2009.

Gehman, C. L., Harry, D. L., Sanford, W. E., Stednick, J. D. and Beckman, N. A.: Estimating specific yield and storage change in an unconfined aquifer using temporal gravity surveys, Water Resour. Res., 46(4), doi:10.1029/2007WR006096, 2009.

Goebel, M., Pidlisecky, A. and Knight, R.: Resistivity imaging reveals complex pattern of saltwater intrusion along Monterey coast, J. Hydrol., 551, 746–755, doi:10.1016/j.jhydrol.2017.02.037, 2017.

Goebel, M., Knight, R. and Halkjær, M.: Mapping saltwater intrusion with an airborne electromagnetic method in the offshore coastal environment, Monterey Bay, California, J. Hydrol. Reg. Stud., 23, doi:10.1016/j.ejrh.2019.100602, 2019.

Gómez, S., Ramos, G., Mesejo, A., Camacho, R., Vásquez, M. and del Castillo, N.: Well Test Analysis of Naturally Fractured Vuggy Reservoirs with an Analytical Triple Porosity-Double Permeability Model and a Global Optimization Method, Oil Gas Sci. Technol., 69(4), 653–671, doi:10.2516/ogst/2013182, 2014.

González-Quirós, A. and Comte, J. C.: Relative importance of conceptual and computational errors when delineating saltwater intrusion from resistivity inverse models in heterogeneous coastal aquifers, Adv. Water Resour., 144, doi:10.1016/j.advwatres.2020.103695, 2020.

Goyetche, T.: Seawater intrusion, transition zone dynamics and reactive mixing - Example of Argentona coastal alluvial aquifer, UPC, Barcelona., 2021.

Günther, T., Rücker, C. and Spitzer, K.: Three-dimensional modelling and inversion of dc resistivity data incorporating topography — II. Inversion, Geophys. J. Int., 166(2), 506–517, doi:10.1111/j.1365-246X.2006.03011.x, 2006.

Guo, W., langevin, C. D., Jr, D., Dausman, A. and Sukop, M.: SEAWAT Version 4: A Computer Program for Simulation of Multi-Species Solute and Heat Transport, , doi:10.13140/RG.2.2.22879.97444, 2008.

al Hagrey, S. A.: 2D Model Study of CO 2 Plumes in Saline Reservoirs by Borehole Resistivity Tomography, Int. J. Geophys., 2011, doi:10.1155/2011/805059, 2011.

Henry, H. R.: Effect of Dispersion on Salt Encroachment in Coastal Aquifers, U.S. Geol. Surv. Water-Supply, Paper 1613, 70–84, 1964.

Herckenrath, D., Odlum, N., Nenna, V., Knight, R., Auken, E. and Bauer-Gottwein, P.: Calibrating a Salt Water Intrusion Model with Time-Domain Electromagnetic Data, GroundWater, 51(3), 385–397, doi:10.1111/j.1745-6584.2012.00974.x, 2013a.

Herckenrath, D., Fiandaca, G., Auken, E. and Bauer-Gottwein, P.: Sequential and joint hydrogeophysical inversion using a field-scale groundwater model with ERT and TDEM data, Hydrol. Earth Syst. Sci., 17(10), 4043–4060, doi:10.5194/hess-17-4043-2013, 2013b.

Hermans, T., Vandenbohede, A., Lebbe, L., Martin, R., Kemna, A., Beaujean, J. and Nguyen, F.: Imaging artificial salt water infiltration using electrical resistivity tomography constrained by geostatistical data, J. Hydrol., 438–439, 168–180, doi:10.1016/j.jhydrol.2012.03.021, 2012.

Hermans, T., Kemna, A. and Nguyen, F.: Covariance-constrained difference inversion of time-lapse electrical resistivity tomography data, GEOPHYSICS, 81(5), E311–E322, doi:10.1190/geo2015-0491.1, 2016.

Hinnell, A. C., Ferr, T. P. A., Vrugt, J. A., Huisman, J. A., Moysey, S., Rings, J. and Kowalsky, M. B.: Improved extraction of hydrologic information from geophysical data through coupled hydrogeophysical inversion, Water Resour. Res., doi:10.1029/2008WR007060, 2010.

Huizer, S., Karaoulis, M. C., Oude Essink, G. H. P. and Bierkens, M. F. P.: Monitoring and simulation of salinity changes in response to tide and storm surges in a sandy coastal aquifer system, Water Resour. Res., 53(8), 6487–6509, doi:10.1002/2016WR020339, 2017.

Iribar, V., Carrera, J., Custodio, E. and Medina, A.: Inverse modelling of seawater intrusion in the Llobregat delta deep aquifer, J. Hydrol., doi:10.1016/S0022-1694(96)03290-8, 1997.

Irving, J. and Singha, K.: Stochastic inversion of tracer test and electrical geophysical data to estimate hydraulic conductivities, Water Resour. Res., 46(11), doi:10.1029/2009WR008340, 2010.

Jardani, A., Revil, A. and Dupont, J.-P.: Stochastic joint inversion of hydrogeophysical data for salt tracer test monitoring and hydraulic conductivity imaging, Adv. Water Resour., 2012.

Jordi, C., Doetsch, J., Günther, T., Schmelzbach, C. and Robertsson, J. O. A.: Geostatistical regularization operators for geophysical inverse problems on irregular meshes, Geophys. J. Int., 213(2), 1374–1386, doi:10.1093/gji/ggy055, 2018.

Karaoulis, M. C., Kim, J. H. and Tsourlos, P. I.: 4D active time constrained resistivity inversion, J. Appl. Geophys., 73(1), 25–34, doi:10.1016/j.jappgeo.2010.11.002, 2011.

Kiessling, D., Schmidt-Hattenberger, C., Schuett, H., Schilling, F., Krueger, K., Schoebel, B., Danckwardt, E. and Kummerow, J.: Geoelectrical methods for monitoring geological CO2 storage: First

results from cross-hole and surface–downhole measurements from the CO2SINK test site at Ketzin (Germany), Int. J. Greenh. Gas Control, 4(5), 816–826, doi:10.1016/J.IJGGC.2010.05.001, 2010.

Kitanidis, P. K.: Introduction to Geostatistics: Applications in Hydrogeology, Cambridge University Press, Cambridge., 1997.

Koestel, J., Kemna, A., Javaux, M., Binley, A. and Vereecken, H.: Quantitative imaging of solute transport in an unsaturated and undisturbed soil monolith with 3-D ERT and TDR, Water Resour. Res., 44(12), doi:10.1029/2007WR006755, 2008.

Kowalsky, M. B., Finsterle, S., Peterson, J., Hubbard, S., Rubin, Y., Majer, E., Ward, A. and Gee, G.: Estimation of field-scale soil hydraulic and dielectric parameters through joint inversion of GPR and hydrological data, Water Resour. Res., 41(11), 1–19, doi:10.1029/2005WR004237, 2005.

Kreyns, P., Geng, X. and Michael, H. A.: The influence of connected heterogeneity on groundwater flow and salinity distributions in coastal volcanic aquifers, J. Hydrol., 586, doi:10.1016/j.jhydrol.2020.124863, 2020.

Krysanova, V., Donnelly, C., Gelfan, A., Gerten, D., Arheimer, B., Hattermann, F. and Kundzewicz, Z. W.: How the performance of hydrological models relates to credibility of projections under climate change, Hydrol. Sci. J., 63(5), 696–720, doi:10.1080/02626667.2018.1446214, 2018.

LaBrecque, D. and Yang, X.: Difference Inversion of ERT Data: a Fast Inversion Method for 3-D In Situ Monitoring, J. Environ. Eng. Geophys. - J Env. ENG Geophys, 6, doi:10.4133/JEEG6.2.83, 2001.

LaBrecque, D. J., Ramirez, A. L., Daily, W. D., Binley, A. M. and Schima, S. A.: ERT monitoring of environmental remediation processes, Meas. Sci. Technol., 7(3), 375–383, doi:10.1088/0957-0233/7/3/019, 1996.

Lebbe, L.: Parameter identification in fresh-saltwater flow based on borehole resistivities and freshwater head data, Adv. Water Resour., 22(8), 791–806, doi:https://doi.org/10.1016/S0309-1708(98)00054-2, 1999.

Leontarakis, K. and Apostolopoulos, G. V.: Laboratory study of the cross-hole resistivity tomography: The Model Stacking (MOST) Technique, J. Appl. Geophys., 80, 67–82, doi:10.1016/j.jappgeo.2012.01.005, 2012.

Lesmes, D. P. and Friedman, S. P.: Relationships between the Electrical and Hydrogeological Properties of Rocks and Soils, in Hydrogeophysics, edited by Rubin Yoram and S. S. and Hubbard, pp. 87–128, Springer Netherlands, Dordrecht., 2005.

Linde, N. and Doetsch, J.: Joint Inversion in Hydrogeophysics and Near-Surface Geophysics, in Integrated Imaging of the Earth: Theory and Applications., 2016.

Linde, N., Binley, A., Tryggvason, A., Pedersen, L. B. and Revil, A.: Improved hydrogeophysical characterization using joint inversion of cross-hole electrical resistance and ground-penetrating radar traveltime data, Water Resour. Res., 42(12), W12404, doi:10.1029/2006WR005131, 2006.

Loke, M. H.: Constrained Time-Lapse Resistivity Imaging Inversion, in Symposium on the Application of Geophysics to Engineering and Environmental Problems 2001, pp. EEM7–EEM7., 2008.

Looms, M. C., Binley, A., Jensen, K. H., Nielsen, L. and Hansen, T. M.: Identifying Unsaturated Hydraulic Parameters Using an Integrated Data Fusion Approach on Cross-Borehole Geophysical Data, Vadose Zo. J., doi:10.2136/vzj2007.0087, 2008.

Martínez-Pérez, L., Marazuela, M. A., Goyetche, T., Luquot, L., Folch, A., del Val, L., Diego-Feliu, M., Palacios, A., Ferrer, N., Rodellas, V., Bellmunt, F., Ledo, J., Pool, M., Garcia-Orellana, J., Pezard, P. A., Saaltink, M. W., Vazquez-Suñe, E. and Carrera, J.: Facing geological heterogeneity impact at the Argentona experimental site, 2019.

Martínez Pérez, L.: Characterization of seawater intrusion and submarine groundwater discharge in al luvial coastal aquifers: field and laboratory approach., UPC, Barcelona. [online] Available from: http://hdl.handle.net/2117/341600 (Accessed 9 July 2021), 2020.

Maurer, H. and Friedel, S.: Outer-space sensitivities in geoelectrical tomography, GEOPHYSICS, 71(3), G93–G96, doi:10.1190/1.2194891, 2006.

Michael, H. A., Mulligan, A. E. and Harvey, C. F.: Seasonal oscillations in water exchange between aquifers and the coastal ocean, Nature, 436(7054), 1145–1148, doi:10.1038/nature03935, 2005.

Michael, H. A., Scott, K. C., Koneshloo, M., Yu, X., Khan, M. R. and Li, K.: Geologic influence on groundwater salinity drives large seawater circulation through the continental shelf, Geophys. Res. Lett., 43(20), 10,782-10,791, doi:10.1002/2016GL070863, 2016.

Michael, H. A., Post, V. E. A., Wilson, A. M. and Werner, A. D.: Science, society, and the coastal groundwater squeeze, Water Resour. Res., 53(4), 2610–2617, doi:10.1002/2017WR020851, 2017.

Miller, C. R., Routh, P. S., Brosten, T. R. and McNamara, J. P.: Application of time-lapse ERT imaging to watershed characterization, Geophysics, 73(3), doi:10.1190/1.2907156, 2008.

Minutti, C., Illman, W. A. and Gomez, S.: A New Inverse Modeling Approach for Hydraulic Conductivity Estimation Based on Gaussian Mixtures, Water Resour. Res., 56(9), doi:10.1029/2019WR026531, 2020.

Nguyen, F., Kemna, A., Antonsson, A., Engesgaard, P., Kuras, O., Ogilvy, R., Gisbert, J., Jorreto, S. and Pulido-Bosch, A.: Characterization of seawater intrusion using 2D electrical imaging, Near Surf. Geophys., 7(5–6), 377–390, doi:10.3997/1873-0604.2009025, 2009.

Oberdörster, C., Vanderborght, J., Kemna, A. and Vereecken, H.: Investigating Preferential Flow Processes in a Forest Soil Using Time Domain Reflectometry and Electrical Resistivity Tomography, Vadose Zo. J., 9, doi:10.2136/vzj2009.0073, 2010.

Paepen, M., Hanssens, D., De Smedt, P., Walraevens, K. and Hermans, T.: Combining resistivity and frequency domain electromagnetic methods to investigate submarine groundwater discharge in the littoral zone, Hydrol. Earth Syst. Sci., 24(7), 3539–3555, doi:10.5194/hess-24-3539-2020, 2020.

Palacios, A., José Ledo, J., Linde, N., Luquot, L., Bellmunt, F., Folch, A., Marcuello, A., Queralt, P., A. Pezard, P., Martínez, L., Del Val, L., Bosch, D. and Carrera, J.: Time-lapse cross-hole electrical resistivity tomography (CHERT) for monitoring seawater intrusion dynamics in a Mediterranean aquifer, Hydrol. Earth Syst. Sci., 24(4), doi:10.5194/hess-24-2121-2020, 2020.

Pauw, P. S., Groen, J., Groen, M. M. A., van der Made, K. J., Stuyfzand, P. J. and Post, V. E. A.: Groundwater salinity patterns along the coast of the Western Netherlands and the application of cone penetration tests, J. Hydrol., 551, 756–767, doi:10.1016/j.jhydrol.2017.04.021, 2017.

Pilar, P., Guedes Soares, C. and Carretero, J.: 44-year wave hindcast for the North East Atlantic European coast, Coast. Eng., 55, 861–871, doi:10.1016/j.coastaleng.2008.02.027, 2008.

Post, V., Kooi, H. and Simmons, C.: Using hydraulic head measurements in variable-density ground water flow analyses, Ground Water, 45(6), 664–671, doi:10.1111/j.1745-6584.2007.00339.x, 2007.

Post, V. E. A.: Fresh and saline groundwater interaction in coastal aquifers: Is our technology ready for the problems ahead?, Hydrogeol. J., 13(1), 120–123, doi:10.1007/s10040-004-0417-2, 2005a.

Post, V. E. A.: Fresh and saline groundwater interaction in coastal aquifers: Is our technology ready for the problems ahead?, Hydrogeol. J., 13(1), 120–123, doi:10.1007/s10040-004-0417-2, 2005b.

Post, V. E. A. and Werner, A. D.: Coastal aquifers: Scientific advances in the face of global environmental challenges, J. Hydrol., 551, 1–3, doi:10.1016/j.jhydrol.2017.04.046, 2017.

Purvance, D. T. and Andricevic, R.: On the electrical-hydraulic conductivity correlation in aquifers, Water Resour. Res., 36(10), 2905– 2913, doi:10.1029/2000WR900165, 2000.

Rücker, C., Günther, T. and Spitzer, K.: Three-dimensional modelling and inversion of dc resistivity data incorporating topography - I. Modelling, Geophys. J. Int., 166(2), 495–505, doi:10.1111/j.1365-246X.2006.03010.x, 2006.

Rücker, C., Günther, T. and Wagner, F. M.: pyGIMLi: An open-source library for modelling and inversion in geophysics, Comput. Geosci., 109, 106–123, doi:10.1016/j.cageo.2017.07.011, 2017.

Sanz, E. and Voss, C. I.: Inverse modeling for seawater intrusion in coastal aquifers: Insights about parameter sensitivities, variances, correlations and estimation procedures derived from the Henry problem, Adv. Water Resour., 29(3), 439–457, doi:10.1016/j.advwatres.2005.05.014, 2006.

Schmidt-Hattenberger, C., Bergmann, P., Bösing, D., Labitzke, T., Möller, M., Schröder, S., Wagner, F. and Schütt, H.: Electrical resistivity tomography (ERT) for monitoring of CO2 migration - From tool development to reservoir surveillance at the Ketzin pilot site, in Energy Procedia, pp. 4268–4275., 2013.

Scholer, M., Irving, J., Binley, A. and Holliger, K.: Estimating vadose zone hydraulic properties using ground penetrating radar: The impact of prior information, Water Resour. Res. - WATER RESOUR RES, 47, 2011.

Sen, P. N. and Goode, P. A.: Influence of temperature on electrical conductivity on shaly sands, GEOPHYSICS, 57(1), 89–96, doi:10.1190/1.1443191, 1992.

Shalev, E., Lazar, A., Wollman, S., Kington, S., Yechieli, Y. and Gvirtzman, H.: Biased monitoring of fresh water-salt water mixing zone in coastal aquifers, Groundwater, 47(1), 49–56, doi:10.1111/j.1745-6584.2008.00502.x, 2009.

Shoemaker, W. B.: Important Observations and Parameters for a Salt Water Intrusion Model, Groundwater, 42(6), 829–840, doi:https://doi.org/10.1111/j.1745-6584.2004.t01-2-.x, 2004.

Singha, K. and Gorelick, S. M.: Saline tracer visualized with three-dimensional electrical resistivity tomography: Field-scale spatial moment analysis, Water Resour. Res., 41(5), doi:10.1029/2004WR003460, 2005.

Singha, K., Day-Lewis, F. D., Johnson, T. and Slater, L. D.: Advances in interpretation of subsurface processes with time-lapse electrical imaging, Hydrol. Process., 29(6), 1549–1576,

doi:10.1002/hyp.10280, 2014a.

Singha, K., Day-Lewis F, D., Johnson, T. and Slater L, D.: Advances in interpretation of subsurface processes with time-lapse electrical imaging, Hydrol. Process., 29(6), 1549–1576, doi:10.1002/hyp.10280, 2014b.

Slater, L., Binley, A. ., Daily, W. and Johnson, R.: Cross-hole electrical imaging of a controlled saline tracer injection, J. Appl. Geophys., 44(2–3), 85–102, doi:10.1016/S0926-9851(00)00002-1, 2000.

Steklova, K. and Haber, E.: Joint hydrogeophysical inversion: state estimation for seawater intrusion models in 3D, Comput. Geosci., 21(1), 75–94, doi:10.1007/s10596-016-9595-y, 2017a.

Steklova, K. and Haber, E.: Joint hydrogeophysical inversion: state estimation for seawater intrusion models in 3D, Comput. Geosci., doi:10.1007/s10596-016-9595-y, 2017b.

Sutter, E. and Ingham, M.: Seasonal saline intrusion monitoring of a shallow coastal aquifer using time-lapse DC resistivity traversing, Near Surf. Geophys., 15(1), 59–73, doi:10.3997/1873-0604.2016039, 2017.

Tarallo, D., Fiore, V. Di, Cavuoto, G., Pelosi, N., Punzo, M., Giordano, L. and Marsella, E.: 4D Monitoring of sea water intrusion by Electrical Resistivity Tomography: case study in the coastal alluvial plain of the Volturno River, Italy. [online] Available from: https://www.researchgate.net/publication/269086309, 2014.

del Val, L., Carrera, J., Pool, M., Martínez, L., Casanovas, C., Bour, O. and Folch, A.: Heat Dissipation Test With Fiber-Optic Distributed Temperature Sensing to Estimate Groundwater Flux, Water Resour. Res., 57(3), e2020WR027228, doi:https://doi.org/10.1029/2020WR027228, 2021.

WAMDI Group: The WAM Model - A Third Generation Ocean Wave Prediction Model, J. Phys. Oceanogr., 18, 1775–1810, doi:10.1175/1520-0485(1988)018<1775:TWMTGO>2.0.CO;2, 1988.

Waxman, M. H. and Smits, L. M.: Electrical conductivities in oil-bearing shaly sands, Soc. Pet. Eng. J., 8(2), 107–122, doi:10.2118/1863-A, 1968.

Werner, A. D.: On the classification of seawater intrusion, J. Hydrol., 551, 619–631, doi:10.1016/j.jhydrol.2016.12.012, 2017.

Werner, A. D., Bakker, M., Post, V. E. A., Vandenbohede, A., Lu, C., Ataie-Ashtiani, B., Simmons, C. T. and Barry, D. A.: Seawater intrusion processes, investigation and management: Recent advances and future challenges, Adv. Water Resour., 51, 3–26, doi:10.1016/J.ADVWATRES.2012.03.004, 2013.

Woods, J. A., Teubner, M. D., Simmons, C. T. and Narayan, K. A.: Numerical error in groundwater flow and solute transport simulation, Water Resour. Res., 39(6), doi:10.1029/2001WR000586, 2003.

Yu, X., Yang, J., Graf, T., Koneshloo, M., O'Neal, M. A. and Michael, H. A.: Impact of topography on groundwater salinization due to ocean surge inundation, Water Resour. Res., doi:10.1002/2016WR018814, 2016.

Zarroca, M., Bach, J., Linares, R. and Pellicer, X.: Electrical methods (VES and ERT) for identifying, mapping and monitoring different saline domains in a coastal plain region (Alt Empordà, Northern Spain), J. Hydrol., 409(1–2), 407–422, doi:10.1016/j.jhydrol.2011.08.052, 2011.

Zhou, B. and Greenhalgh, S. A.: Cross-hole resistivity tomography using different electrode configurations, Geophys. Prospect., 48(5), 887–912, doi:10.1046/j.1365-2478.2000.00220.x, 2000.

7 Annex

Annex 1: Published Article

Time-lapse cross-hole electrical resistivity tomography (CHERT) for monitoring seawater intrusion dynamics in a Mediterranean aquifer

Published in: Hydrol. Earth Syst. Sci., 24, 2121–2139, 2020